# SIMULATING THE CAST FILM PROCESS USING AN UPDATED LAGRANGIAN FINITE ELEMENT ALGORITHM

**By**

**W. SPENCER SMITH, M. ENG, B. ENG. C.S.**

**A Thesis Submitted to the School of Graduate Studies**

**in Partial Fulfilment of the Requirements**

**for the Degree Doctor of Philosophy.**

**McMaster University**

**DOCTOR OF PHILOSOPHY (2001)** **McMaster University**
**(Civil Engineering)** **Hamilton, Ontario**

| | |
|---|---|
| **TITLE:** | **Simulating the Cast Film Process Using an Updated Lagrangian Finite Element Algorithm** |
| **AUTHOR:** | **Spencer Smith, M.Eng, B.Eng. C. S. (McMaster University)** |
| **SUPERVISOR:** | **Dr. D. F. E. Stolle** |
| **NUMBER OF PAGES:** | **xxii, 194** |

## Abstract

This thesis presents a new numerical algorithm for 2D nonisothermal time-stepping simulations of a nonlinear viscoelastic cast film process. The most significant contribution of the algorithm is that an updated Lagrangian (UL) description of motion is employed, as opposed to the more conventional Eulerian (E) description generally used in polymer processing simulations. Furthermore, use is made of a constitutive equation unlike those generally employed for polymers. The constitutive equation accommodates viscoelasticity, extensional thinning/thickening, and strain-hardening. A comparison of the UL and E algorithms and constitutive equations shows that the UL algorithm in some respects represents a more natural and intuitive approach, which has the advantage of being "closer" to the physics of the film casting problem.

This new numerical algorithm can find the steady-state film properties, and it can predict the onset of instability by observing draw resonance as a response problem. By determining the critical draw ratio as a response problem, the mathematical complications of the more common linear stability analysis approach are avoided. In terms of the stability of the film, it was observed that stability is decreased by extensional thinning, strain-hardening, and higher relaxation times and stability is increased by extensional thickening, higher heat transfer and higher ratios of air-gap length to die width.

## Acknowledgments

I would like to thank my supervisor, Dr. Dieter Stolle, for his ideas, patience, many efforts on my behalf, and for providing an excellent example of an accomplished researcher and teacher. I would also like to thank my supervisory committee, consisting of Dr. S. Pietruszczak and Dr. J. Vlachopoulos, for their interest in my research, and in the case of Dr. Vlachopoulos with allowing me to accompany his research group to several polymer related conferences. I would also like to acknowledge Dr. B. Koziey for the initial idea of researching the cast film process.

I have a number of people from the Civil Engineering Department at McMaster University whose help I would like to acknowledge. In terms of faculty I should single out Dr. F. Hall, Dr. B. Baetz, Dr. J. Wilson and Dr. F. Mirza. In terms of staff, I am very grateful for the help provided to me over the years by Deborah Smaluck, Gail Britton, Peter Koudys and Anna Robertson. With faculty and staff covered, that just leaves my fellow students, who I should thank for their advice and for giving me the occasional break from work. In particular, I would like to thank Jayson Potts, Gabriel Sedran, Matt Pringle, Todd Randall and Dean Inglis. I would also like to thank Dean's family (Erin and Brenna) for always being interested in how I was doing.

For providing me with financial assistance during my studies I would like to acknowledge the Civil Engineering Department at McMaster and the Natural Sciences and Engineering Research Council of Canada (NSERC).

My family has been very supportive during my many years of graduate studies. I would like to thank my Mother for her encouragement, and for all the little things she has done along the way to help. Finally, I would like to thank my brother Scott and his wife Diane. They both helped me gain perspective on the tasks at hand, either by talking things over with me, or even better, by providing a much needed distraction when things got too chaotic.

# Table of Contents

# List of Figures

# List of Tables

# List of Symbols

The symbols used in this thesis are defined on their first usage and they are summarized in the list that follows, first by chapter and then roughly in their order of appearance. An effort has been made to choose symbols based on the usual conventions adopted in the literature, which in some cases means that a symbol has been assigned multiple meanings. If the meaning of a symbol changes from one chapter to another, then this will be indicated by redefining the symbol under the later chapter's heading. Moreover, the intended meaning of multi-use symbols should be clear from the context in which the symbol is used.

## Chapter 1

| *Symbol* | *Meaning* |
|---|---|
| $x, y, z$ | coordinate axes in the machine, transverse and out-of-plane directions, respectively |
| $\dot{u},\ \dot{v},\ \dot{w}$ | velocities in the machine, transverse and out-of-plane directions, respectively |
| $\boldsymbol{x}$ | spatial position |
| $\boldsymbol{X}$ | initial position of a material particle |
| $t$ | time |
| $\tau$ | some past time |
| $\Delta t$ | time step |
| $P$ | an arbitrary material particle |
| $P'$ | $P$ occupies $P'$ at $t = \tau$ |
| $P''$ | $P$ occupies $P''$ at $t = \tau + \Delta t$ |

## Chapter 2

| *Symbol* | *Meaning* |
|---|---|
| $u, v, w$ | incremental displacements in the machine, transverse and out-of-plane directions, respectively |
| $L$ | air-gap length |
| $W_{die}$ | half of the die width |
| $h_{die}$ | half of the die thickness |
| $T_{die}$ | temperature at the die |

| | |
|---|---|
| $\dot{u}_{die}$ | velocity in the machine direction at the die |
| $\dot{u}_{roll}$ | velocity in the machine direction at the roll |
| $Dr$ | draw ratio ($Dr = \dot{u}_{roll} / \dot{u}_{die}$) |
| $\boldsymbol{L}$ | linear differential operator that relates the incremental strains to the incremental displacements |
| $\boldsymbol{u}$ | incremental displacement vector |
| $\Delta\boldsymbol{\varepsilon}$ | incremental strain tensor as a column vector |
| $\Delta\boldsymbol{\varepsilon}^c$ | incremental creep strain tensor as a column vector |
| $\Delta\varepsilon_{xx}$ | incremental strain in the machine direction |
| $\Delta\varepsilon_{yy}$ | incremental strain in the transverse direction |
| $\Delta\varepsilon_{zz}$ | incremental strain in the out-of-plane direction |
| $\Delta\gamma_{xy}$ | incremental shear strain in the *x*-*y* plane |
| $\boldsymbol{\sigma}$ | stress tensor as a column vector |
| $\Delta\boldsymbol{\sigma}$ | incremental stress tensor as a column vector |
| $\sigma_{xx}$ | Cauchy stress in the machine direction |
| $\sigma_{yy}$ | Cauchy stress in the transverse direction |
| $\sigma_{xy}$ | Cauchy shear stress in the *x*-*y* plane |
| $\boldsymbol{\sigma}_n$ | traction normal to the film boundaries |
| $\mathbf{q}_n$ | thermal flux normal to the film boundaries |
| $T$ | temperature, averaged through the film's thickness |
| $k$ | thermal conductivity |
| $\alpha$ | one-sided heat transfer coefficient for Newton's law of cooling |
| $C$ | specific heat capacity |
| $T_{air}$ | temperature of the air surrounding the film |
| $\boldsymbol{D}$ | elastic membrane constitutive matrix |
| $\dot{\varepsilon}_q^c$ | effective creep strain rate |
| $\psi$ | creep potential function |
| $q$ | effective stress |
| $J_2$ | second invariant of the deviatoric stress tensor |
| $A$ | constitutive parameter |
| $A_0$ | reference value for the $A$ parameter |
| $T_0$ | reference temperature for $A_0$ |
| $m$ | extensional thinning/thickening parameter |
| $n$ | strain hardening/softening parameter |
| $\eta^c$ | creep viscosity |
| $\eta^s$ | shear viscosity |
| $Q$ | activation energy |
| $R$ | gas constant |
| $\varepsilon^e$ | total elastic strain (1D uniaxial extension) |
| $\dot{\varepsilon}^c$ | creep strain rate (1D uniaxial extension) |
| $\lambda$ | relaxation time |

| | |
|---|---|
| $E$ | the elastic modulus |
| $E_1$, $E_2$, $E_3$ | three sample values for the elastic modulus $E$ |
| $\lambda_1$, $\lambda_2$, $\lambda_3$ | three sample values for the relaxation time $\lambda$ |

## Chapter 3

| *Symbol* | *Meaning* |
|---|---|
| $t_{final}$ | time at which the time-stepping simulations are stopped |
| $\boldsymbol{x}$, $\boldsymbol{y}$, $\boldsymbol{z}$ | nodal coordinate values for the finite element mesh, stored in arrays |
| $\boldsymbol{u}$, $\boldsymbol{v}$, $\boldsymbol{w}$ | nodal incremental displacement values, stored in arrays |
| $\Delta\boldsymbol{u}$, $\Delta\boldsymbol{v}$, $\Delta\boldsymbol{w}$ | nodal change in incremental displacement values, stored in arrays |
| $\boldsymbol{\sigma}$ | array of stress tensors at all the integration areas, or a single stress tensor as a column vector |
| $\Delta\boldsymbol{\sigma}$ | array of changes in the stress tensors at all the integration areas, or a single change in stress tensor as a column vector |
| $\Delta\boldsymbol{\sigma}^c$ | array of change in creep stress tensors at all the integration areas, or a single change in creep stress tensor as a column vector |
| $\boldsymbol{\varepsilon}_q^c$ | array of total effective creep strain for all of the integration areas |
| $\Delta\boldsymbol{\varepsilon}_q^c$ | array of change in effective creep strain for all of the integration areas |
| $\boldsymbol{T}$ | nodal values for the temperature degree of freedom; the same symbol is used at the element level and at the system level |
| $\Delta\boldsymbol{T}$ | change in the nodal values for the temperature degrees of freedom; the same symbol is used at the element level and at the system level |
| $u_{CL}$ | incremental displacement in the machine direction at the centre-line, or line of symmetry, for the film |
| $w_{CL}$ | incremental displacement in the out-of-plane direction at the centre-line, or line of symmetry, for the film |
| $\boldsymbol{B}$ | average shape function gradients matrix for the in-plane mechanical analysis |
| $\boldsymbol{D}^{ve}$ | viscoelastic tangential constitutive matrix |
| $\boldsymbol{a}$ | nodal degree of freedom values for the in-plane incremental displacements ($u$ and $v$); the same symbol is used at the element level and at the system level |
| $\Delta\boldsymbol{a}$ | change in $\boldsymbol{a}$ |
| $\boldsymbol{R}$ | load vector for the finite element analysis |
| $F$ | $\Delta t\dot{\varepsilon}_q^c = \Delta\varepsilon_q^c$ |
| $C_1$ | a parameter for the implicit creep algorithm |
| $H_e$ | a parameter for the implicit creep algorithm |
| $H_c$ | a parameter for the implicit creep algorithm |
| $\boldsymbol{K}_\sigma$ | the initial stress matrix |
| $\delta(\Delta\boldsymbol{\varepsilon})$ | virtual strain tensor consistent with the virtual displacements |

| | |
|---|---|
| $p$ | pressure |
| $\Delta p$ | change in pressure |
| $\alpha$ | a parameter where $\alpha \rightarrow \infty$ for an incompressible material |
| $\delta(\Delta W_v)$ | change in virtual volumetric work done |
| $\delta\varepsilon_{xx}$, $\delta\varepsilon_{yy}$, $\delta\varepsilon_{zz}$ | virtual strains |
| $\boldsymbol{B}_{zz}$ | average shape function gradients matrix for the out-of-plane mechanical analysis |
| $\|\cdot\|$ | Euclidean norm of a vector |
| *toler* | convergence criteria for ceasing the iterations |
| $q$ | effective stress |
| $q_0$ | initial effective stress |
| $\Delta\varepsilon_q$ | change in effective strain |
| $\Delta\varepsilon_q^c$ | change in effective creep strain |
| $q_e$ | effective elastic stress |
| $\varepsilon_q$ | effective strain |
| $J_2^\varepsilon$ | second invariant of the deviatoric strain |
| $G$ | shear modulus |
| $\boldsymbol{s}$ | deviatoric stress tensor stored as a column vector |
| $\boldsymbol{s}_e$ | elastic deviatoric stress tensor stored as a column vector |
| $p_e$ | pressure calculated assuming an elastic material |
| $\boldsymbol{I}$ | similar to the identity matrix, but written as a column vector |
| $\boldsymbol{H}$ | heat transfer matrix |
| $\boldsymbol{C}$ | heat capacity matrix |
| $\boldsymbol{F}$ | heat input load vector |
| $\boldsymbol{N}_T$ | matrix of shape functions for the interpolation of the temperature |
| $dA$ | the differential in-plane area |
| $\dot{\boldsymbol{T}}$ | the rate of change of the temperature degrees of freedom; depending on the context, this vector holds the system or element level degrees of freedom |
| $\boldsymbol{B}_T$ | matrix of shape function gradients associated with the temperature degrees of freedom |
| $\boldsymbol{T}_{k+1}$ | temperature degrees of freedom at the end of the $k^{\text{th}}$ time step |
| $\boldsymbol{T}_k$ | temperature degrees of freedom at the beginning of the $k^{\text{th}}$ time step |
| $V^d$ | the volume of the $d^{\text{th}}$ integration area |
| $\boldsymbol{B}^d$ | the average shape function gradients for the $d^{\text{th}}$ integration area |
| $\Delta\boldsymbol{\varepsilon}^d$ | the strain for the $d^{\text{th}}$ integration area |
| $\boldsymbol{LDL}^T$ | matrix decomposition into a lower triangular, a diagonal matrix and the transpose of the lower triangular matrix |

## Chapter 4

| *Symbol* | *Meaning* |
|---|---|
| $\tau_{ij}$ | the extra-stress tensor, using index notation |
| $K$ | a constant used in the E version of the power-law constitutive equation |
| $\dot{I}\dot{I}$ | an invariant proportional to the second invariant of the rate of deformation tensor |
| $\beta$ | the shear-thinning/thickening parameter for the E version of the power-law constitutive equation |
| $D_{ij}$ | rate of deformation tensor, using index notation |
| $s_{ij}$ | deviatoric stress tensor, using index notation |
| $\dot{\varepsilon}_{ij_c}$ | creep strain rate tensor, using index notation |
| $\dot{\varepsilon}_{ij}$ | strain rate tensor, using index notation |
| $\sigma$ | the total force in a Maxwell element |
| $\dot{\gamma}^s$ | the rate of straining in the spring in a Maxwell element |
| $\dot{\gamma}^d$ | the rate of straining in the dashpot in a Maxwell element |
| $\Delta\varepsilon_{ij}$ | the change in the strain tensor, using index notation |
| $\dot{\tau}_{ij}$ | the rate of change of the extra-stress tensor, using index notation |
| $E$ | the elastic modulus |
| $\varepsilon$ | the natural strain in a uniaxial extension |
| $L$ | the length of a uniaxial member |
| $L_0$ | the initial length of a uniaxial member |
| $\dot{u}$ | the velocity at the free end of a uniaxial member |
| $\dot{\sigma}_{xx}$ | the rate of change of the stress in a uniaxial member |
| $\check{\tau}_{ij}$ | the rate of change of the extra-stress tensor, using the upper convected derivative |
| $D/Dt$ | the material, or substantial, derivative |
| $L_{ij}$ | the velocity gradient tensor, using index notation |
| $\varepsilon^e_{ij}$ | the integral of the rate of deformation tensor holding the material particle constant; this measure is not a tensor |
| $B_{ij}$ | the finger deformation tensor, using index notation |

## Chapter 5

| *Symbol* | *Meaning* |
|---|---|
| *nel* | the number of finite elements |
| $\dot{W}^c$ | the rate of viscous energy dissipated |
| *ninteg* | the total number of integration points |

| | |
|---|---|
| $\eta_0^s$ | the shear viscosity at a reference temperature |
| $h_{roll}$ | the thickness of the film at the roll |

**Chapter 6**

| *Symbol* | *Meaning* |
|---|---|
| $Ar$ | the aspect ratio ($Ar = L/W_{die}$) |
| $nelL$ | the number of elements in the machine direction |
| $nelW$ | the number of elements in the transverse direction |
| $F$ | the force in the machine direction applied to the film at the roll |
| $W_{roll}$ | the width of the film at the roll |

**Chapter 7**

*No new symbols are introduced in this chapter*

**Chapter 8**

| *Symbol* | *Meaning* |
|---|---|
| $\boldsymbol{D}$ | rate of deformation tensor, written as a column vector |
| $\boldsymbol{n}$ | normal vector |
| $\Gamma_t$ | boundary where the traction is specified |
| $\Gamma_u$ | boundary where the displacement is specified |
| $\Gamma_q$ | boundary where the thermal flux is specified |
| $\Gamma_T$ | boundary where the temperature is specified |
| $\boldsymbol{t}$ | Traction applied to a surface |
| $\boldsymbol{\Psi}$ | the residual load vector |
| $\boldsymbol{K}^i$ | the stiffness matrix for the Eulerian algorithm and the $i^{th}$ iteration |
| $\boldsymbol{a}^i$ | the degree of freedom vector for the Eulerian algorithm and the $i^{th}$ iteration |
| $\boldsymbol{a}^{i+1}$ | the degree of freedom vector for the Eulerian algorithm and the $(i+1)^{th}$ iteration |
| $\Delta\boldsymbol{a}^i$ | the change in the degree of freedom vector |
| $\boldsymbol{a}_u$ | the degree of freedom values for the in-plane velocities |
| $\boldsymbol{a}_h$ | the degree of freedom values for the thickness |
| $\boldsymbol{a}_T$ | the degree of freedom values for the temperature |
| $\boldsymbol{a}_W$ | the degree of freedom values for the width |

| | |
|---|---|
| $\Delta \boldsymbol{a}_u$ | the change in the degree of freedom values for the in-plane velocities |
| $\Delta \boldsymbol{a}_h$ | the change in the degree of freedom values for the thickness |
| $\Delta \boldsymbol{a}_T$ | the change in the degree of freedom values for the temperature |
| $\Delta \boldsymbol{a}_W$ | the change in the degree of freedom values for the width |
| $\boldsymbol{F}^i$ | the load vector for the Eulerian algorithm and the $i^{\text{th}}$ iteration |
| $\boldsymbol{K}_T^i$ | the tangential stiffness matrix for the Eulerian algorithm and the $i^{\text{th}}$ iteration |

# Chapter 1 Introduction and Background

Two main approaches exist for describing the motion of a body: the material formulation, where the conservation equations are applied to a specific body, or control mass; and the spatial formulation, where the conservation equations are written in terms of a region in space, or control volume. Although the different formulations should yield identical results for any smooth motion of a body, for any given type of motion there is often an obvious choice as to which formulation is preferable. For instance, fluid mechanics problems lend themselves nicely to spatial, often termed Eulerian (E), formulations of motion. On the other hand, solid and structural mechanics problems are usually best treated using material, also known as Lagrangian (L) and updated Lagrangian (UL), descriptions of motion. Although the choice for description of motion is well established for fluid and solid mechanics problems, it is not so clear which choice is best when the material in question exhibits properties of both a fluid and a solid; that is, when the material is viscoelastic. To clarify the relative advantages and disadvantages of the spatial versus material approaches, this thesis considers the behaviour of an important class of viscoelastic material, polymers.

In the literature on polymer processing the usual choice to describe motion is a spatial formulation, especially when the processing operates continuously. Therefore, to compare the spatial and material descriptions, it is first necessary to develop a material description for

some continuous process. The process selected for comparison is the film casting process because it is an industrially significant process, and because the influence of the material properties and processing conditions on the finished product is not entirely understood. Therefore, besides comparing spatial and material formulations, this thesis also provides an opportunity to investigate the underlying physics of the cast film process.

The film casting process is described in Section 1.1 and some common problems encountered while casting are listed in Section 1.2. Although numerical simulation is a useful tool to gain a better understanding of these problems, simulation of the film casting process has several complications, which are the subject of Section 1.3. Different approaches have been employed to address the complications associated with simulating film casting. A review of the different approaches available in the literature is provided in Section 1.4. Thereafter, an overview of the current study is provided in Section 1.5. One of the principal distinctions between the new approach and previous approaches is the description of motion. The distinctions between the different descriptions of motion, E, L and UL, are clarified in Section 1.6. The final section of this chapter, Section 1.7, summarizes the purpose and scope of this research.

## 1.1 Description of the Cast Film Process

Figure 1.1 provides an overview of a typical continuous film casting operation. The process starts with solid polymer pellets in a hopper. These pellets are gravity fed into an extruder. The extruder consists of a screw that melts the polymer and provides the pressure

necessary to force the now molten polymer through a centre-fed “T” or coat-hanger die. Information on the design and operation of these dies is provided in TAPPI Press (1992). After exiting the die, the film is pulled through an air-gap, where it is cooled by convected cold air or an inert gas before it makes contact with a thermoregulated chill roll. To ensure good contact of the film with the chill roll and to aid in freezing, an air-knife is often used to blow a jet of air at the film. After freezing, the secondary film is hauled off for further treatment, such as heating and biaxial stretching. Once treated, the finished product goes to a winder, which produces the rolls of finished film.

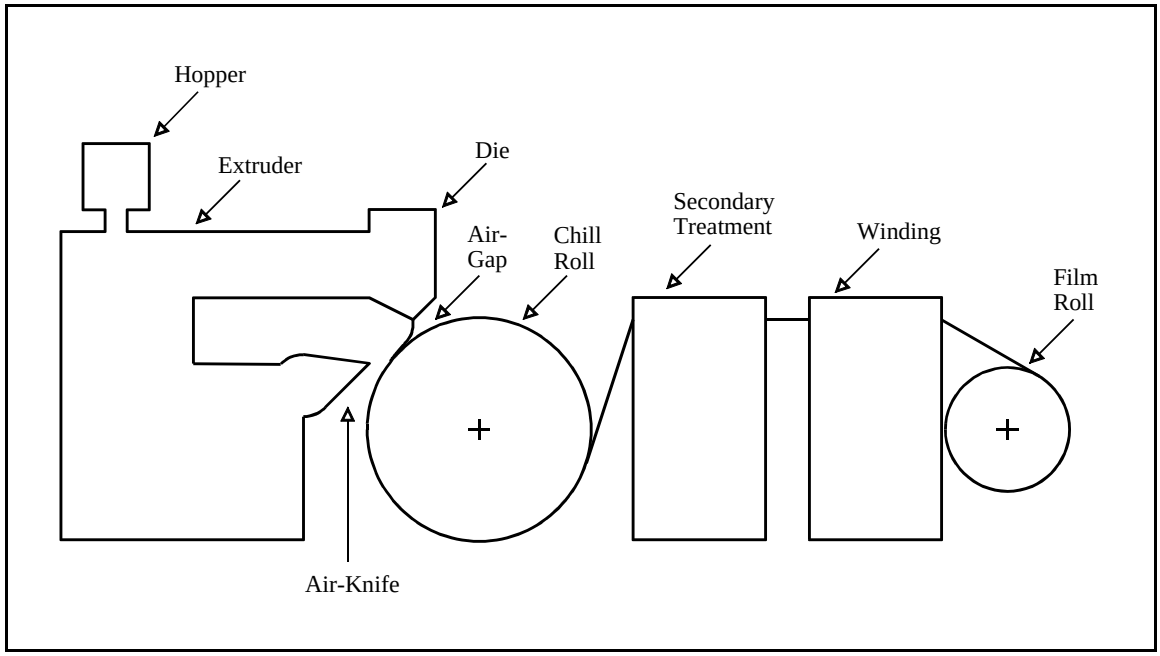


**Figure 1.1** Overview of the cast film process

One of the most important of the many stages used to produce cast film is the stretching of the film through the air-gap. Studies on film casting, including this one, typically focus on how the film behaves in the air-gap because the properties of the finished

product are mainly determined at this stage (Barq *et al*. 1992). Although the air-gap only represents a small fraction of the polymer processing time, the behaviour of the film in the air-gap is important because the success of downstream operations depends on the quality of the film supplied from upstream. A close-up schematic of the air-gap is shown in Figure 1.2. Further details on the film casting processes can be found in Pearson (1985) and Smith (1997).

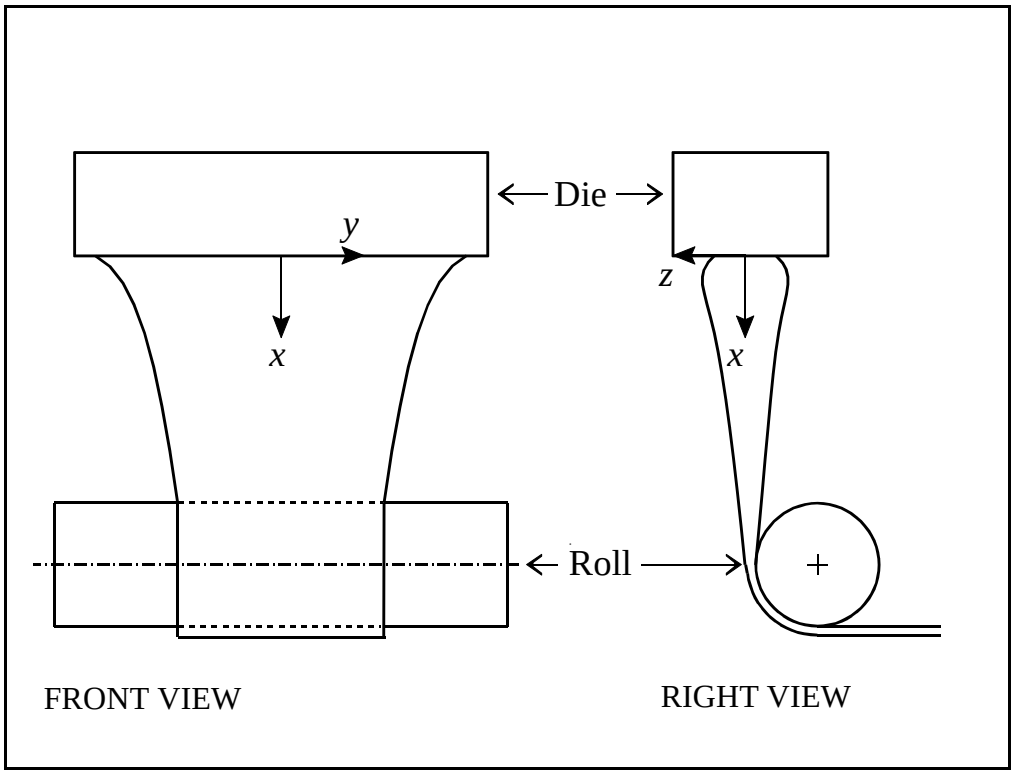


**Figure 1.2** Overview of the cast film process in the air gap

## 1.2 Problems Encountered with Film Casting

Important goals for film line designers are to maximize the production of a uniform thickness film and to minimize wasted film. Three main problems interfere with these goals:

i) the stretching of the film reduces its width (neck-in);

ii) thick beads form at the edges of the film (edge bead); and

iii) once the speed at the roll relative to that at the die exceeds some critical value, the width and thickness of the film begin to vary periodically (draw resonance).

At present, these three problems are still not well understood. Computer simulation of the process is one technique available for gaining a better understanding of the above problems, and possibly suggesting ways to mitigate them.

### 1.3 Difficulties Associated with Numerical Simulation of the Cast Film Process

At present, a trial-and-error approach is generally used to design film lines, as there are few numerical algorithms available to simulate the process. Any advances in the numerical modelling of film lines must take into account, and overcome, the following complications:

i) the free surface is initially unknown;

ii) the problem is highly nonlinear;

iii) there is a strong coupling between the velocity and the thickness;

iv) a large number of degrees of freedom are required; and,

v) the stress for most polymers has a complicated dependence on the deformation and thermal history of the material.

Several different approaches, which are summarized in the next section, have been used to address some of the above difficulties.

## 1.4 Literature Review on Cast Film

The cast film literature can be categorized according to the assumptions made to simplify the idealized governing equations. Section 1.4.1 lists and explains some typical simplifying assumptions made in the film casting literature. Besides categorizing the literature according to the assumptions made, different studies can also be subdivided by whether or not the model considers draw resonance. The literature that neglects draw resonance and focuses on steady-state operations is the subject of Section 1.4.2. Following this, the studies that predict draw resonance are summarized in Section 1.4.3. Besides differences in the assumptions and in the focus of a study, the literature can also be distinguished by the numerical algorithms used, which are listed in Section 1.4.4. All of the references cited in this section use a spatial description of motion.

### 1.4.1 The Assumptions Made in Film Casting Research

Ideally, the solution for a film casting problem would accommodate the following: three-dimensional variation of all the variables; nonisothermal conditions; all external influences, such as an air-knife or vacuum box; a complete rheological characterization of the polymer; and the entire deformation and temperature history of the polymer. Such a model is not yet, and may never be, available. The models that have been created are subsets of this ideal model. Typical assumptions that distinguish a given model from the ideal model include the following:

- simplify dimensionality: 1D versus 1.5D versus 2D

- assume isothermal
- assume a constitutive equation
- exclude inertial effects
- exclude the self-weight of the polymer
- neglect the sag of non-vertical films
- exclude die-swell
- use uniform boundary conditions at the die
- neglect surface tension
- neglect air-drag
- neglect the influence of the air-knife and/or vacuum box
- use a single layer of film, as opposed to modelling a process where different polymers are combined to form a multilayer film

Except for the terminology introduced for the dimensionality assumptions and the term die-swell, the items in the above list are self-explanatory. Table 1.1 clarifies the terminology for the dimensionality by summarizing the kinematic assumptions on the velocity components ($\dot{u}$, $\dot{v}$, $\dot{w}$) for each type of analysis. The corresponding coordinate directions ($x$, $y$, $z$) used in the table are the same as those shown in Figure 1.2. The dimensionality of the film problem determines whether neck-in and edge bead can be accommodated. This information is also shown in Table 1.1. As for the term die-swell, it can be explained by referring to Figure 1.2 and noting the increase in thickness as the film exits the die. This increase in thickness is die-swell, and it is explained by the sudden change from a confined shear flow inside the die to an essentially extensional flow field in the air-gap.

**Table 1.1 Summary of the Kinematic Assumptions**

| Dim | Direction | | | Neck-in | Edge Bead |
|---|---|---|---|---|---|
| | **Machine (*x*)** | **Transverse (*y*)** | **Out-of-Plane (*z*)** | | |
| **1D** | $\dot{u} = \dot{u}(x)$ | $\dot{v} = 0$ | $\dot{w} = \dot{w}(x, z)$ | No | No |
| **1.5D** | $\dot{u} = \dot{u}(x)$ | $\dot{v} = \dot{v}(x, y)$ | $\dot{w} = \dot{w}(x, z)$ | Yes | No |
| **2D** | $\dot{u} = \dot{u}(x, y)$ | $\dot{v} = \dot{v}(x, y)$ | $\dot{w} = \dot{w}(x, y, z)$ | Yes | Yes |

Published research on film casting consists of various combination of the above assumptions. In some studies good results are obtained for a limited class of film casting problems. However, the large range of processing conditions and materials encountered in industry means that no model has been proposed to date that adequately captures all behaviour. In the sections that follow, the film casting literature is summarized according to three key assumptions: the dimensionality assumption; whether the model is for isothermal conditions; and the constitutive law adopted. The studies cited in the sections that follow are for single layer films. Information on multilayer films can be found in Pis-Lopez and Co (1996a, 1996b).

### 1.4.2 Literature on Steady-State Film Casting

Table 1.2 summarizes the film casting literature that solves the steady-state film casting problem. The term steady-state is used to indicate that this literature does not consider transient behaviour or the related phenomenon of draw resonance. The table

compares the research according to the three key assumptions mentioned above. As Table 1.2 shows, most of the steady-state film casting studies are 1D or 1.5D; as a consequence of this, the influence of the edge-bead on the film has received only limited attention. The table also shows that the majority of film casting studies assume a Newtonian fluid.

**Table 1.2 Summary of the Assumptions Made in the Steady-State Studies**

| **Reference** | **Dim** | **Constitutive Equation** | **Thermal** |
|---|---|---|---|
| Avenas *et al*. (1986) | 1.5D | Newtonian | iso |
| Cotto, Duffo and Haudin (1989) | 1.5D | Newtonian | noniso |
| d'Halewyu *et al*.(1990) | 2D | Newtonian | iso |
| Agassant *et al*. (1991) | 1.5D | Newtonian | iso |
| Alaie and Papanastasiou (1991) | 1D | BKZ-type integral | noniso |
| Duffo, Monasse and Haudin (1991) | 1.5D | Newtonian | noniso |
| Barq *et al*. (1992) | 1.5D | Newtonian | noniso |
| Iyengar and Co (1993) | 1D | Modified Giesekus | iso |
| Debbaut *et al*. (1995) | 2D | Power-Law, Maxwell-B and Giesekus | iso |
| Sakaki *et al*. (1996) | 3D | Newtonian | iso |
| Beaulne and Mitsoulis (1999) | 1.5D | Upper-Convected Maxwell and K-BKZ Integral Model | noniso |
| Rajagopalan (1999) | 2D* | Giesekus (Giesekus 1982) | iso |
| Smith and Stolle (2000a) | 2D | Newtonian | noniso |
| Acierno *et al*. (2000) | 1.5D** | Newtonian | noniso |

* Rajagopalan (1999) is 2D in the sense that the thickness varies in the transverse direction, but edge-bead and neck-in are not included because the computational domain is restricted to the central portion of the film.

** Acierno *et al*. (2000) is 1D for the temperature predictions

### 1.4.3 Draw Resonance Literature

Table 1.3 is the same format as Table 1.2, except that the focus is on the stability research. This summary shows that only a small number of papers consider the stability of 2D films. Furthermore, nonisothermal problems have received only limited attention and the variety of constitutive equations considered is small.

**Table 1.3 Summary of the Key Assumptions in the Draw Resonance Research**

| **Reference** | **Dim** | **Constitutive Equation** | **Thermal** |
|---|---|---|---|
| Yeow (1974) | 1D | Newtonian | iso |
| Aird and Yeow (1983) | 1D | Power-Law | iso |
| Minoshima and White (1983) | 1D | Newtonian | noniso |
| Lee (1984) | 2D* | Power-Law | iso |
| Anturkar and Co (1988) | 1D | Modified Convected Maxwell | iso |
| Barq *et al*. (1990) | 1D | Newtonian | iso |
| Barq *et al*. (1994) | 1D | Convected Maxwell | iso |
| Silagy *et al*. (1996a) | 1.5D | Newtonian | iso |
| Silagy *et al*. (1996b) | 1.5D | Newtonian | iso |
| Iyengar and Co (1996) | 1D | Modified Giesekus | iso |
| Sialgy *et al*. (1998) | 2D | Newtonian and viscoelastic | iso |
| Silagy *et al*. (1999) | 2D | Newtonian | iso |

* Lee (1984) models the film differently than the other studies, by considering the film as a parallel composition of numerous fibre filaments spun simultaneously.

### 1.4.4 Solution Techniques

Table 1.4 summarizes the solution techniques corresponding to the simulation studies of Table 1.2. This summary shows that closed-form solutions are rare and only exist for the 1D and 1.5D cases, and only for the case of viscous fluids. Of the numerical techniques used, the finite element method (FEM) is the most popular. For the finite element simulations, the algorithm is either step-wise uncoupled or coupled. When the analysis is uncoupled, the velocity, width and thickness are each solved in turn, based on the current values of the other variables. Since such an approach may be slow or may have convergence problems, coupled algorithms, which solve all of the variables simultaneously, are preferred.

**Table 1.4 Summary of Techniques used for Solving the Governing Equations**

| **Reference** | **Solution Technique** |
|---|---|
| Avenas *et al*. (1986) | closed-form solution |
| Cotto, Duffo and Haudin (1989) | an explicit finite difference method |
| d'Halewyu, Agassant and Demay (1990) | step-wise uncoupled solution technique:<br>i) the velocity is found using FEM;<br>ii) the width is found using the Newton-Raphson method; and then<br>iii) the thickness is found using the finite volume method. |
| Agassant *et al*. (1991) | closed-form solution |
| Alaie and Papanastasiou (1991) | fully coupled Newton-Raphson FEM |
| Duffo, Monasse and Haudin (1991) | an explicit finite difference method |
| Barq *et al*. (1992) | Runge-Kutta's and Adams-Bashforth's methods (Conte and De Boor 1980: pp373-376) |
| Iyengar and Co (1993) | $4^{th}$ order Runge-Kutta with adaptive step size control |
| Debbaut *et al*. (1995) | fully coupled Newton-Raphson mixed FEM with upwinding for the mass transport equation |
| Sakaki *et al*. (1996) | streamline finite element method |
| Beaulne and Mitsoulis (1999) | fully coupled Newton-Raphson FEM |
| Rajagopalan (1999) | a coupled finite element method based on the elastic-viscous split stress formulation developed by Rajagopalan *et al*. (1990) |
| Smith and Stolle (2000a) | fully coupled Newton-Raphson FEM |
| Acierno *et al*. (2000) | a shooting method |

With respect to the determination of draw resonance, the most popular approach is linear stability analysis, which is used for almost all of the studies of Table 1.3. Another approach that is sometimes employed is to observe draw resonance as a response problem. In this case the time-dependent governing equations are solved and resonance is observed directly as oscillations in the film's geometry. This is the approach employed by Barq *et al*. (1990, 1994) and Silagy *et al*. (1998, 1999).

## 1.5 An Overview of the New Algorithm

Following the headings used in Tables 1.2 and 1.3, the current study can be classified as 2D and nonisothermal, with a viscoelastic constitutive equation. The constitutive equation accommodates Newtonian fluids, power-law viscosity, elastic effects and strain-hardening. Of the assumptions listed in Section 1.4.1, the influence of the following are assumed to be negligible in this thesis: inertia, self-weight, sag, die-swell, surface tension and air-drag. Furthermore, only uniform boundary conditions are used, the influence of the air-knife is neglected, and only a single layer of film is modelled.

The algorithm developed in this thesis can be used for both steady-state and draw resonance studies, as the algorithm uses time stepping to solve the transient governing equations. Stability is assumed to exist if the oscillations of the film geometry die out when a steady-state solution has been reached. On the other hand, if the oscillations do not die out, then draw resonance is assumed to have developed.

Probably the most important distinction between the algorithm introduced here and those used in previous studies, is that the current study uses a material description of motion. This decision has significant ramifications for the finite element algorithm. To better understand these ramifications, the next section describes the differences between spatial and material descriptions of motion.

## 1.6 Types of Description of Motion

Let us consider the motion of an arbitrary material particle $P$ corresponding to three different configurations over time, as shown in Figure 1.3 for a two-dimensional (2D) coordinate system. The motion of $P$ can be described by a relation between the spatial position ($\boldsymbol{x}$) and the initial coordinates ($\boldsymbol{X}$) and time ($t$); that is, $\boldsymbol{x} = \boldsymbol{x}(\boldsymbol{X}, t)$, with the independent variables being $\boldsymbol{X}$ and $t$. This equation expresses a material description of motion in a Lagrangian (L) formulation. In a Lagrangian analysis the initial configuration at $\boldsymbol{X}$ provides a reference configuration to which all future variables are referred back to. Although the choice of a reference configuration is an arbitrary one, often the initial configuration of the body is selected for a Lagrangian analysis. If instead, the reference configuration is continuously updated, then one has the updated Lagrangian (UL) formulation, in which $\boldsymbol{x} = \boldsymbol{x}(\boldsymbol{x}(\tau), t)$ with the independent variables being $\boldsymbol{x}(\tau)$ and $t$. In the UL approach all variables are expressed relative to the present configuration, at time $\tau$, in order to find the state of the system in a future configuration, at time $\tau+\Delta t$. For both the L and UL formulations one explicitly tracks the motion of the particles.

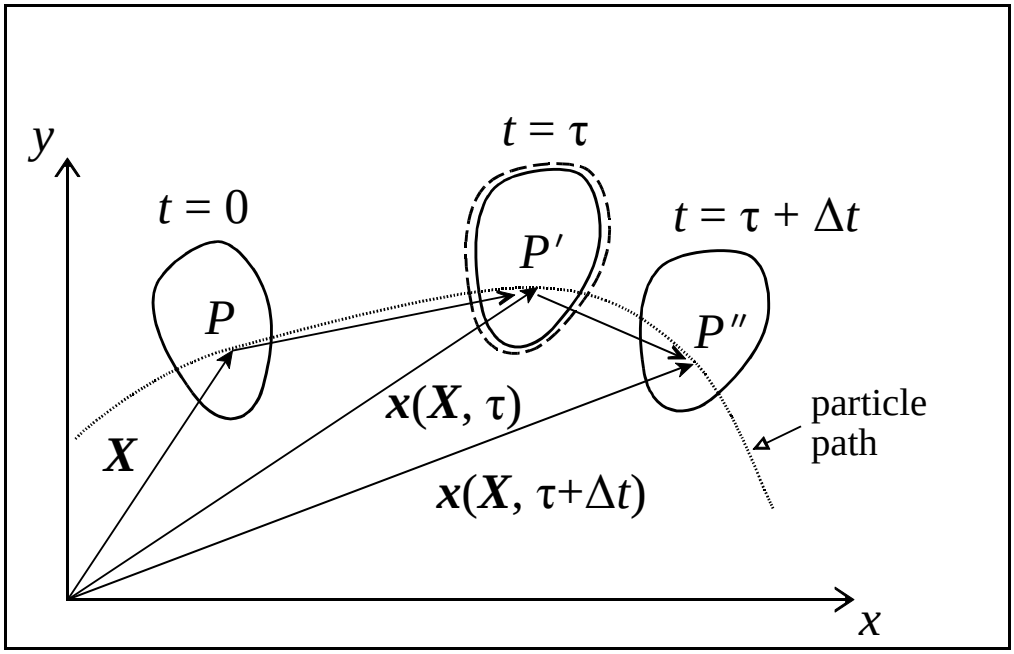


**Figure 1.3** Motion of a particle over time

For the spatial, or the so-called Eulerian (E), formulation, time and the current location in space $\boldsymbol{x}$ are the independent variables. Since the focus is on a region in space, denoted by the control volume shown by the dashed line in Figure 1.3, particle $P$ is not unique to the spatial point located at $P'$. Particle $P$, which is coincident with point $P'$ at $t = \tau$, is one of many particles that pass through $P'$. It is for this reason that the kinematics of the spatial formulation are best expressed in terms of velocities and velocity gradients rather than displacements and displacement gradients.

The choice of description of motion strongly influences the numerical algorithm and the implementation of the finite element method. Table 1.5 distinguishes four finite element formulations: Lagrangian, updated Lagrangian, Eulerian and arbitrary Lagrangian Eulerian

(ALE), and provides some example applications for each. When interpreting the finite element literature using the definitions of Table 1.5, caution should be employed since the terms UL and E are not always applied correctly (Gadala, Oravas and Dokainish 1983).

**Table 1.5 Different Finite Element Formulations**

| Type | Mesh | Example Applications |
|---|---|---|
| L | Stationary, corresponds to material | Solid and structural mechanics, including large deformation problems |
| UL | Moves with material, corresponds to material | Large deformation problems in solid and structural mechanics |
| E | Stationary, corresponds to space | Fluid mechanics, viscoelastic fluids (Marchal and Crochet 1987; Lou and Mitsoulis 1990), soil penetration (Van Den Berg, De Borst and Huétink 1996) |
| ALE | Motion independent of material, corresponds to space | Fluid structure interaction, free surface problems (Liu *et al*. 1988) |

## 1.7 Purpose and Scope

A new numerical algorithm, based on an updated Lagrangian formulation, is introduced in this thesis for the simulation of film casting. The two main purposes for developing the algorithm are: i) simulations can be performed to gain a better understanding of the film casting process and how the problems of neck-in, edge-bead and draw resonance are influenced by the material and the processing conditions; ii) the UL algorithm can be compared to E algorithms to identify the respective strengths and weaknesses of each approach.

Chapter 2 summarizes the governing partial differential equations and boundary conditions assumed for this study with Chapter 3 presenting the corresponding numerical algorithm used to solve the governing equations and associated boundary conditions. The proposed algorithm uses a constitutive equation that is more commonly encountered in L and UL formulations, even though the literature on polymers uses constitutive equations from an E framework. To relate the current study to the existing body of knowledge, it is necessary to relate the UL and E constitutive equations, which is the topic of Chapter 4. Chapter 5, 6 and 7, respectively, provide simulation results for 1D, 1.5D and 2D versions of the simulation algorithm. Each of these chapters includes a parametric study to examine the influence of various constitutive parameters and processing conditions on steady-state conditions and on the stability of the film. Chapter 8 compares the UL algorithm to an E algorithm and Chapter 9 lists the conclusions and recommendations from this study.

# Chapter 2 Governing Equations

This chapter presents the governing equations and boundary conditions for the 2D film casting problem following a UL framework. Equations are provided for equilibrium, continuity, conservation of thermal energy and the constitutive response.

## 2.1 Coordinate System and Notation

Figure 2.1 shows the Cartesian coordinate system used for the film casting problem. The origin is located at the centre of the die, and the coordinates run in the machine direction $x$, the transverse direction $y$, and the out-of-plane direction $z$. The dimensions of the film problem are defined by the air-gap length $L$, the die width $2W_{die}$ and the die thickness $2h_{die}$. A factor of 2 is used in labelling the dimensions of the die to facilitate the introduction of the symmetry constraints.

In this and most of the subsequent chapters, the notation used is similar to that of Zienkiewicz (1977), in which symmetric 2$^{nd}$ order tensors, such as stress and strain, are represented as vectors and the constitutive description is written in matrix form. All symbols used in this thesis are defined upon their first usage. In addition, a list of symbols is provided starting on page xvi and the component expansions of the variables are summarized in Appendix A.

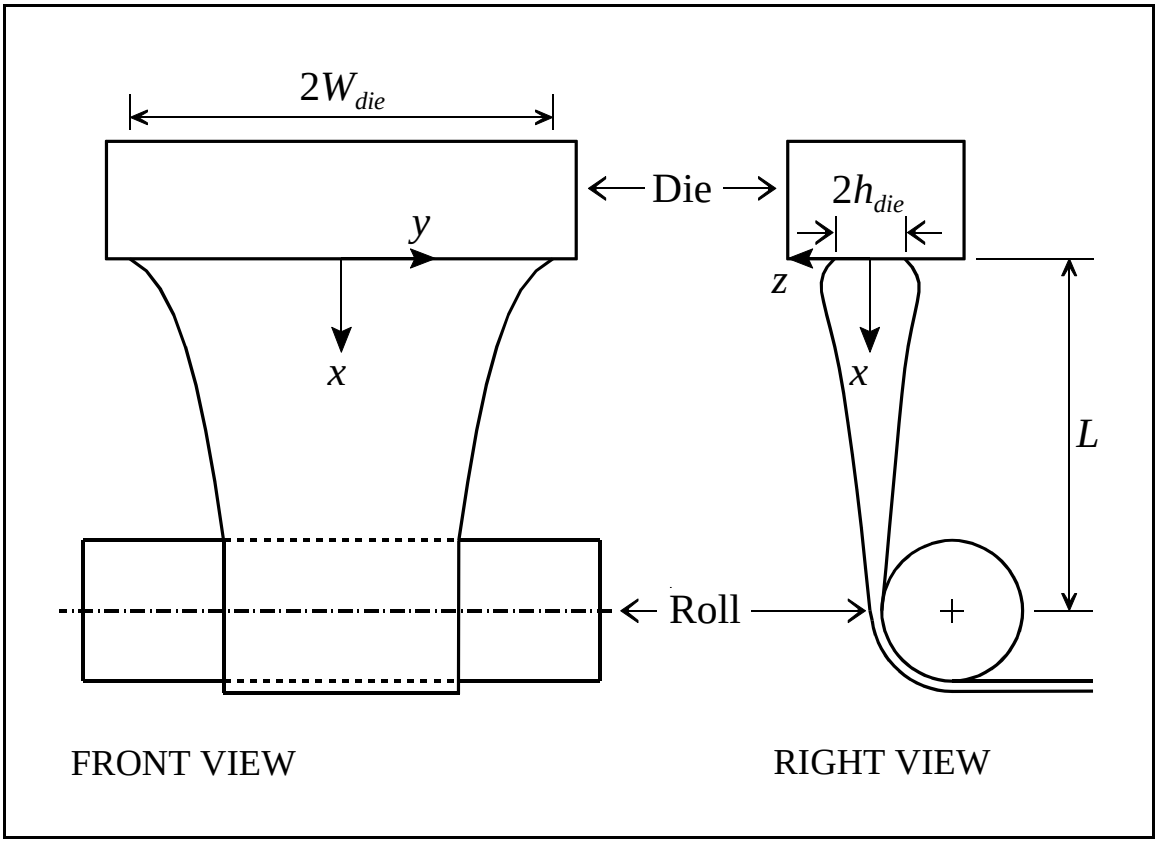


**Figure 2.1** Coordinate system and dimensions for the 2D film casting problem

## 2.2 Equilibrium Equation

At every instant in time the film must satisfy the equilibrium equation. If inertia, self-weight, air-drag and surface tension are neglected, then the equilibrium equation can be written as

$$\boldsymbol{L}^T\boldsymbol{\sigma} = \mathbf{0} \tag{2.1}$$

where $\boldsymbol{L}$ is the linear differential operator that relates incremental strains $\Delta\boldsymbol{\varepsilon}$ to incremental displacements $\boldsymbol{u}$, such that $\Delta\boldsymbol{\varepsilon} = \boldsymbol{L}\boldsymbol{u}$, and $\boldsymbol{\sigma}$ is the Cauchy stress tensor for the deformed

configuration. Appendix A shows the component expansions for $\boldsymbol{L}$, $\boldsymbol{\sigma}$, $\Delta\boldsymbol{\varepsilon}$ and $\boldsymbol{u}$. The film is assumed to behave as a membrane, which reduces the number of components in the equilibrium equation to only those necessary for a plane stress problem; i.e. $\boldsymbol{\sigma} = [\sigma_{xx}\ \sigma_{yy}\ \sigma_{xy}]^T$. This reduction is possible because for a membrane the normal to the film's surface is approximately in the *z*-direction, and the magnitude of the out-of-plane shear is negligible when compared to that of the other components. This assumptions applies when the film is thin and the thickness gradient is small. Strictly speaking the membrane approximation does not hold at the edges of the film (Pearson 1985: p478).

## 2.3 Continuity Equation

The equilibrium calculation using the membrane approximation only predicts the in-plane incremental displacements *u* and *v*. To determine the out-of-plane incremental displacement *w*, an explicit calculation using continuity, that is, volumetric strain considerations, must be introduced. If the melt is assumed incompressible for both the viscous and the elastic responses, the out-of-plane strain can be related to the two in-plane components via

$$\Delta\varepsilon_{zz} = -(\Delta\varepsilon_{xx} + \Delta\varepsilon_{yy}) \qquad \textbf{(2.2)}$$

which in turn can be used to calculate *w*.

## 2.4 Conservation of Thermal Energy

In the case of nonisothermal film casting, the transient 2D temperature field $T(x,y,t)$ of the membrane can be calculated using the following governing partial differential equation:

$$k\nabla^T(\nabla T) - \alpha(T - T_{air}) - \rho C\frac{\partial T}{\partial t} = 0 \qquad \textbf{(2.3)}$$

where $\nabla^T = [\partial/\partial x \; \partial/\partial y]$, $\alpha$ is the heat transfer coefficient from the film's surface, $T_{air}$ is the surrounding air's temperature, and $k$, $\rho$ and $C$ are material properties for the thermal conductivity, density and specific heat capacity, respectively. The source term in the above equation is actually a boundary condition on the film's upper surface, where Newton's law of cooling is assumed to apply. The conservation of thermal energy equation assumes that the temperature varies little through the thickness of the film. The equation also neglects viscous dissipation, as it is assumed negligible for the film casting process.

## 2.5 Constitutive Equation

Adopting a constitutive equation for an elastic material that is creeping and invoking the additivity postulate, the incremental form of Hooke's law may be written as

$$\Delta\boldsymbol{\sigma} = \boldsymbol{D}\,(\Delta\boldsymbol{\varepsilon} - \Delta\boldsymbol{\varepsilon}^c) \qquad \textbf{(2.4)}$$

where $\Delta\boldsymbol{\sigma}$ is the stress increment, $\boldsymbol{D}$ represents the elasticity matrix, and $\Delta\boldsymbol{\varepsilon}$ and $\Delta\boldsymbol{\varepsilon}^c$ are the total strain and creep strain increments, respectively. The components of $\boldsymbol{D}$ are given in Appendix A and the derivation of $\boldsymbol{D}$ is shown in Appendix B.

The creep strain increment may conveniently be expressed using the approach adopted by Perzyna (1966), which in a modified form can be written as

$$\Delta\boldsymbol{\varepsilon}^{c} = \Delta t\, \dot{\varepsilon}_q^c \frac{\partial \psi}{\partial \boldsymbol{\sigma}} \tag{2.5}$$

with $\Delta t$ being the time step, $\dot{\varepsilon}_q^c$ the effective creep strain rate and $\psi$ the creep potential function, which is defined as

$$\psi \equiv q, \quad with\ q = \sqrt{3J_2} \tag{2.6}$$

The parameter $q$ is the effective stress (Kraus 1980: p29), and $J_2$ represents the second invariant of the deviatoric stress tensor.

If the creep strain rate is assumed to follow a time hardening creep law, then

$$\varepsilon_q^c = A q^m t^n \tag{2.7}$$

where $A$, $m$ and $n$ are constants and $t$ is the total time. This law can be transformed into the strain hardening form, by holding $q$ constant and taking the time derivative of Equation 2.7. After some manipulations, the strain hardening relationship for the creep strain rate is obtained by eliminating time $t$ in the rate equation through the use of Equation 2.7; i.e.,

$$\dot{\varepsilon}_q^c = nA^{\frac{1}{n}} q^{\frac{m}{n}} (\varepsilon_q^c)^{\frac{n-1}{n}} \tag{2.8}$$

A close examination of the above equation indicates that it is an equation of state, in which $\dot{\varepsilon}_q^c = f(\varepsilon_q^c, q)$. A special case of Equation 2.8 occurs when $m = n = 1$ and $A = 1/(2\eta^c)$. In this case the above equation describes a Von Mises material, with a creep viscosity of $\eta^c$. The

viscosity is assumed to depend on temperature via an Arrhenius relation, which is introduced through the $A$ parameter via

$$A = A_0 e^{\left[-\frac{Q}{R}\left(\frac{1}{T} - \frac{1}{T_0}\right)\right]} \qquad \textbf{(2.9)}$$

where $Q$ is the activation energy, $R$ is the gas constant (8.314 J mol$^{-1}$ K$^{-1}$) and $A_0$ and $T_0$ are the reference values for the $A$ parameter and for the temperature, respectively.

Figure 2.2 illustrates the constitutive response by showing how the stress changes as the material undergoes an isothermal uniaxial extension. Plot (a) shows that the function relating stress $\sigma$ and elastic strain $\varepsilon^e$ is linear, with a slope equal to the elastic modulus $E$. The viscous response is shown in Plot (b), which illustrates the variation of stress with creep strain rate $\dot{\varepsilon}^c$. In the case of a Newtonian fluid the viscosity is constant, but for extensional thinning and thickening materials, increasing strain rates lead to decreasing and increasing viscosities, respectively. The constitutive description adopted in this thesis combines the responses shown in (a) and (b) to produce a viscoelastic material, which is illustrated in Plot (c). This plot shows three linear Maxwell elements undergoing the same constant rate of straining. The elements are distinguished from one another by their relaxation time $\lambda$, which is a measure of how long the material "remembers" past deformations. The lower the value of $\lambda$, the closer the material's response is to a viscous fluid and the higher the value, the closer the response is to an elastic solid. The three previously discussed plots (a, b and c) show a material that is not fundamentally changed by its deformation history, but if the value of the strain-hardening parameter $n$ is not equal to 1.0, then the material behaviour will be

affected by its past deformation. Plot (d) shows strain-hardening and softening materials, for which the constitutive behaviour depends on the total value of the accumulated creep strain. The softening behaviour ($n > 1$) in Plot (d) is unstable; therefore, the materials considered in this study will require that $n \leq 1$.

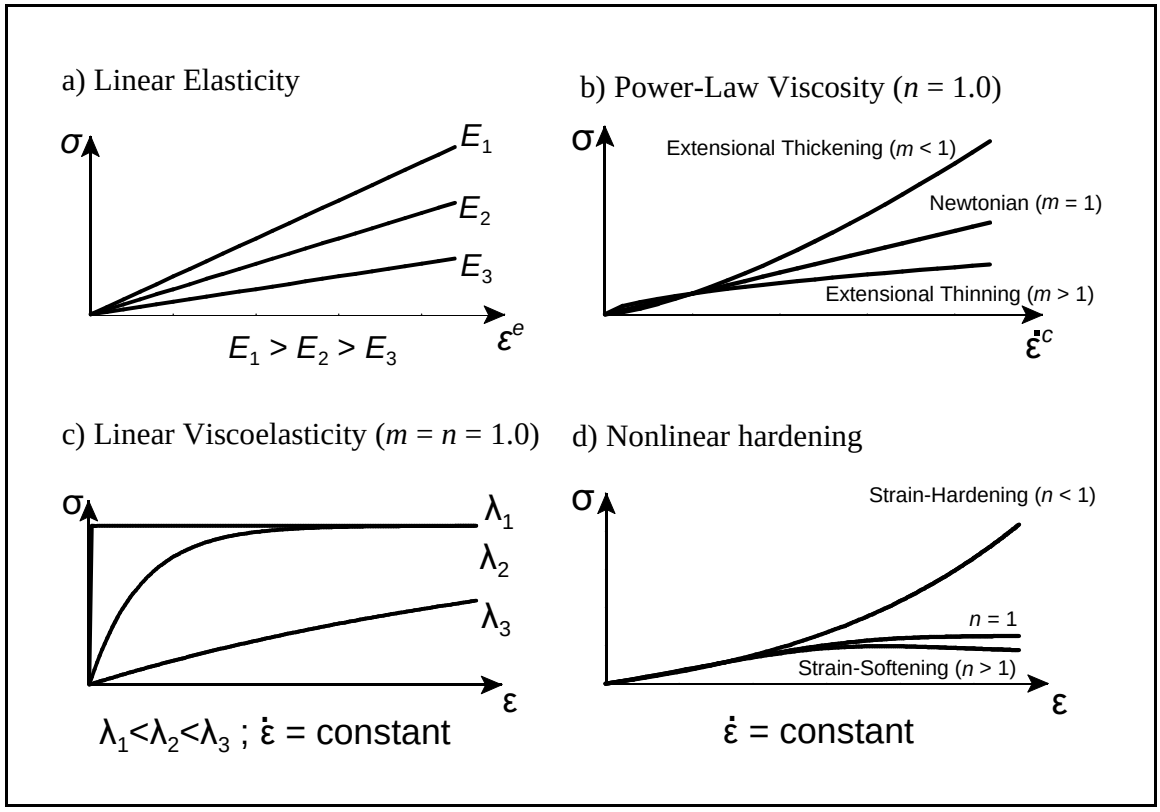


**Figure 2.2** Examples of constitutive behaviour under isothermal uniaxial extension

## 2.6 Boundary Conditions

The boundary conditions for the half width of the film casting problem are shown in Figure 2.3. As mentioned earlier, the film is assumed to be symmetric about its centre line. The mechanical boundary conditions specified inside the die and on the roll imply that the

film will move downstream (in the machine direction) as a rigid body at these locations. The ratio of the downstream speed at the roll to the speed at the die provides an important dimensionless number for characterising the film casting problem, the draw ratio *Dr*, where $Dr = \dot{u}_{roll} / \dot{u}_{die}$. On the roll the transverse $\dot{v}$ and out-of-plane $\dot{w}$ velocities are set to zero to simulate the sudden freezing of the melt when it contacts the chill roll. At the free surface and the line of symmetry, the natural boundary conditions of zero normal stress ($\boldsymbol{\sigma}_n$) and zero shear are assumed to apply. The thermal boundary conditions for the film consist of prescribing the temperature inside the die as $T_{die}$ and setting the normal thermal flux $\boldsymbol{q}_n$ to zero on all other surfaces. A zero thermal flux approximation is reasonable given the thinness of the film and its poor thermal conductivity.

One should note that the boundary conditions are expressed in terms of spatial locations, but the governing equations are expressed in terms of the material particles. The boundary conditions that are applied to a given material particle will change as it moves downstream. For a particle with a finite size the spatial location of the transition from one set of boundary conditions can only be approximated. This fact causes some difficulties for the numerical algorithm, which will be discussed in the next chapter.

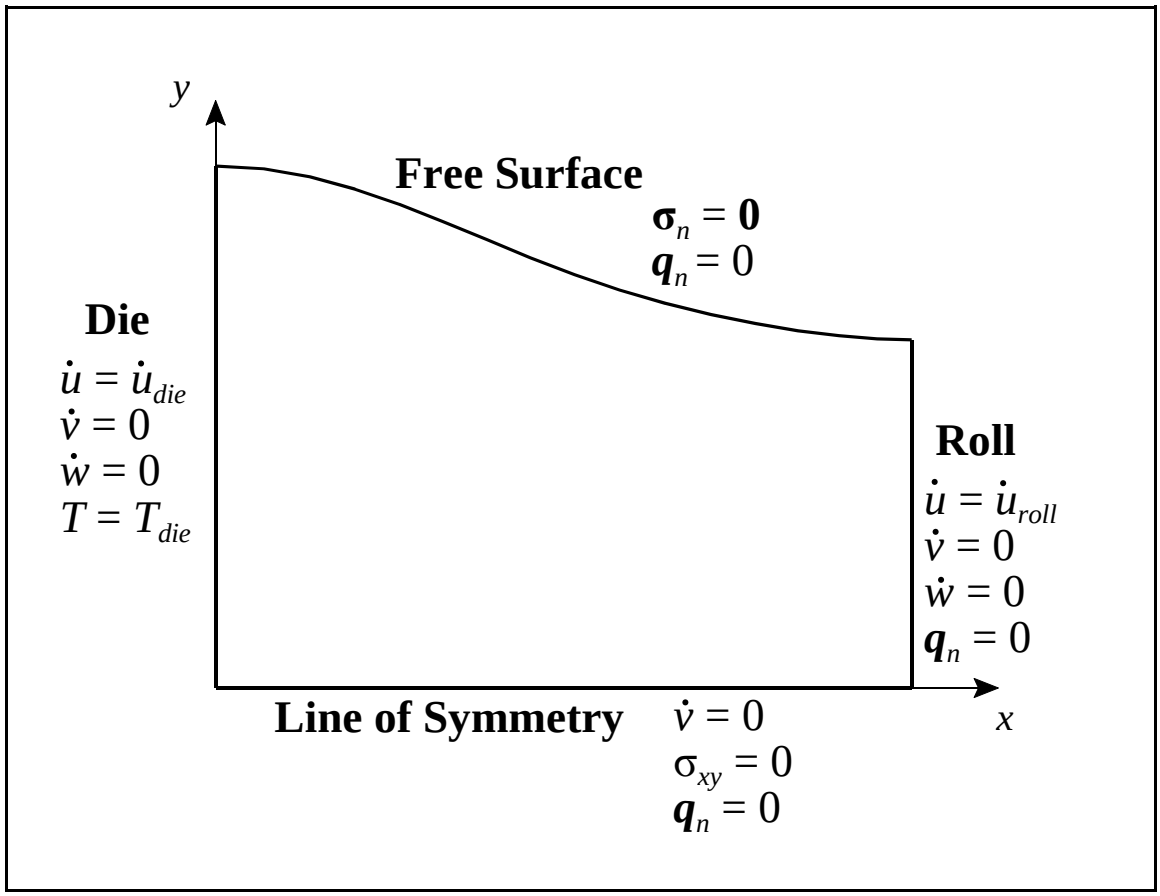


**Figure 2.3** Boundary conditions for the 2D film casting problem

### 2.7 Initial Conditions

The transient analyses of this study typically start with the film inside the die with the temperature set to $T_{die}$. The initial stresses and accumulated creep strain for the material inside the die are assumed to be zero. Strictly speaking, the initial stresses and creep strain are not likely to be zero, as flowing through the die will deform the material. However, the flow in the die is beyond the scope of the present work, so in the absence of upstream information, the stresses and accumulated strains will be assumed to be zero. This is the

same assumption used by Debbaut *et al*. (1995) for their viscoelastic fluid film casting study. A consequence of the zero stress condition, along with use of the membrane approximation, is that the die-swell phenomena cannot be accommodated by the present study.

# Chapter 3 Numerical Algorithm

This chapter describes the UL time-stepping finite element algorithm for numerically simulating film casting. Section 3.1 provides an overview of the algorithm and the definitions for the important variables. Thereafter, Sections 3.2 to 3.7 provide more specific details on the algorithm by describing the following steps: data input, initialization of variables and updating constraints, the nonlinear solution step, the radial return algorithm, the solution of the nodal temperatures, and updating the mesh. Section 3.8 develops the average strain element used by the algorithm with Section 3.9 discussing some issues regarding efficiency. In the final section, Section 3.10, the computer implementation of the numerical algorithm is addressed.

## 3.1 Overview of the Time-Stepping Algorithm

Figure 3.1 provides a flowchart for the time-stepping UL finite element algorithm. To simplify the presentation, the flowchart shows only those variables that are most important, which include the current time ($t$), the final time ($t_{final}$), the nodal coordinates ($\boldsymbol{x}$, $\boldsymbol{y}$, $\boldsymbol{z}$), the displacement degrees of freedom ($\boldsymbol{u}$, $\boldsymbol{v}$, $\boldsymbol{w}$), the stress tensors at the integration points ($\boldsymbol{\sigma}$), the total effective creep strain at the integration points ($\boldsymbol{\varepsilon}_q^c$) and the temperature degrees of freedom ($\boldsymbol{T}$). As usual, the symbol $\Delta$ is used to denote a change in a variable. In the

current context the bold face symbols refer to system level variables; that is, they are vectors that store values for all the nodes, or all the integration points, as appropriate. Some of these same symbols will be reused later in this chapter, but to refer to element level variables. The multiple meanings of the symbols is intended to simplify the notation, and it should not lead to any confusion, as the meaning of the variables will be clear from the context in which they are used.

Each time step of the UL algorithm starts from a known configuration and solves a materially and geometrically nonlinear finite element problem for the nodal displacements and temperatures. At the end of each time step the mesh, stresses, effective creep strains and temperatures are all updated. The updated values provide a new reference configuration and state, which allows one to repeat the prediction process for the following time step.

After many time steps, a given finite element will experience the following sequence of events: i) exits the die; ii) travels through the air-gap; iii) moves on to the chill roll; iv) is removed from the roll and is reinserted and reinitialized inside the die to begin the sequence again. In principle, the time-stepping process can be continued indefinitely; however, this is unnecessary for a stable film problem as the transient behaviour will eventually damp out and a spatially steady-state solution will be reached.

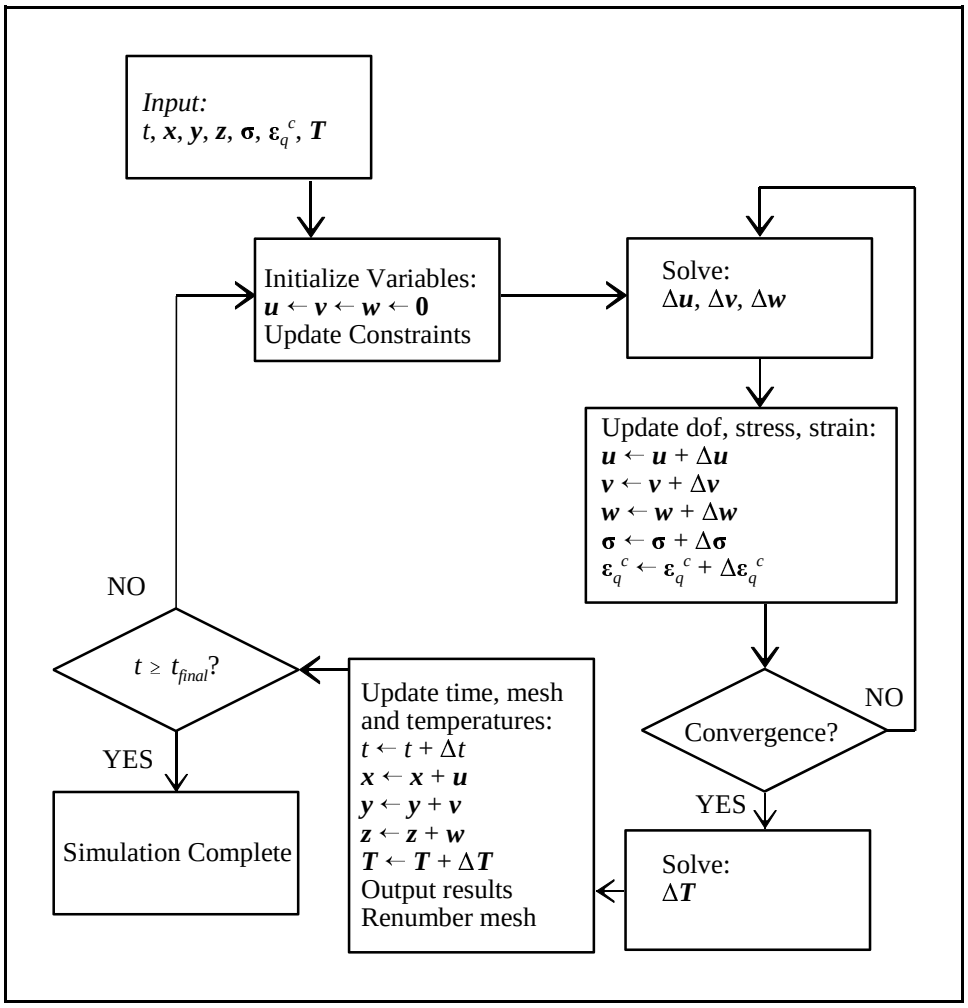


**Figure 3.1** Flowchart for the time-stepping UL finite element algorithm

## 3.2 Input Data

The first step in the program is to read in the information that describes the film casting problem, such as the material properties, the numerical parameters, the element connectivity and the boundary conditions. Initial values must also be provided for the time,

the nodal coordinates, the stress, the total effective creep strain and the temperatures. By default, the initial time, stress and effective creep strain are all zero, the temperatures are all equal to $T_{die}$ and all of the elements are stored inside the die. However, for some simulations it is more efficient to use more complex initial values for these variables. One option is to use initial values for a new simulation that are the final values of a previous simulation, in order to start an analysis from a reasonable initial geometry. Figure 3.2 shows a sample mesh for the situation when such an option is followed.

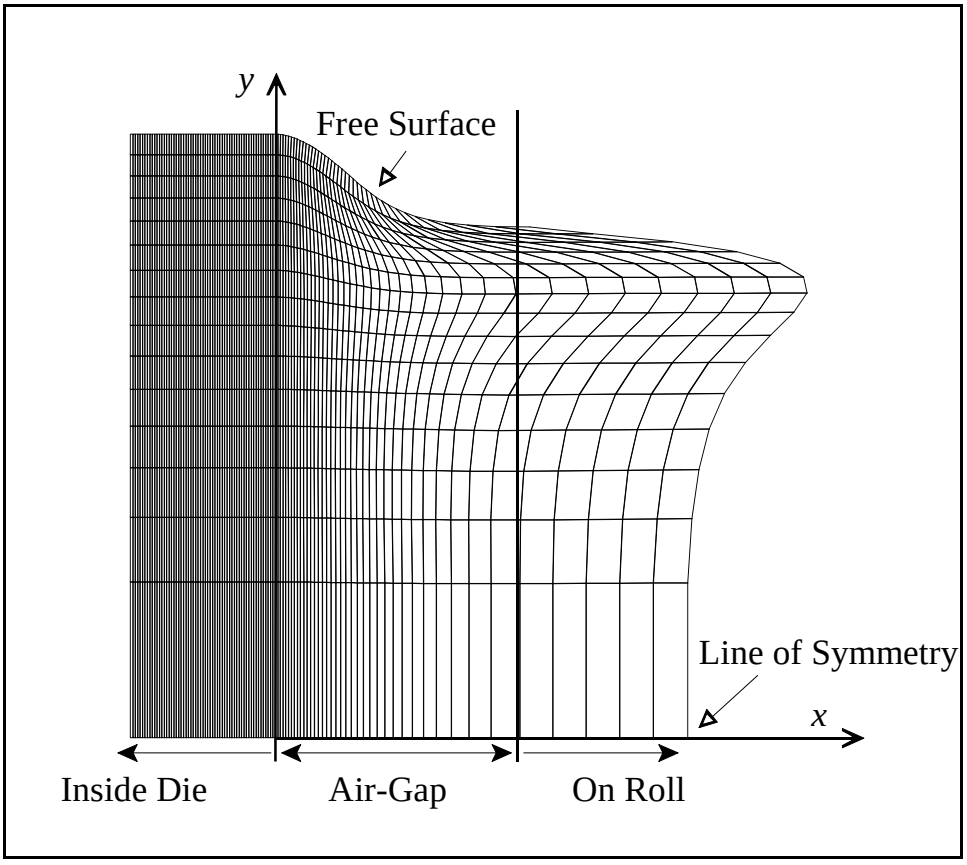


**Figure 3.2** A sample finite element mesh

### 3.3 Initialize Variables and Update Constraints

At the beginning of each time step various variables are initialized, such as the incremental displacement degrees of freedom (dof), which are set to zero. Another task that is performed at the beginning of each step is updating the constraints on the displacement dof. To determine the constraints, each node of the finite element mesh is classified according to its spatial location. Figure 3.2 shows the five spatial classifications: inside the die, on the chill roll, in the air-gap, on the line of symmetry, and at the free surface. In addition to constraints required by a node's spatial location, constraints are also required if the problem is assumed to be either 1D or 1.5D. The kinematic assumptions that define the terms 1D and 1.5D are given in Section 1.4.1. The constraints associated with the node's spatial location and the dimensionality of the problem are shown in Table 3.1.

**Table 3.1 Displacement Constraints for the Nodal Degrees of Freedom**

| Location of node | Dimension of Problem | Prescribed Displacements |
|---|---|---|
| Inside die | any | $u = u_{die}$, $v = 0$, $w = 0$ |
| On roll | any | $u = u_{roll}$, $v = 0$, $w = 0$ |
| On line of symmetry | any | $v = 0$ |
| In air-gap | 1D problem | $u = u_{CL}$, $v = 0$, $w = w_{CL}$ |
| | 1.5D problem | $u = u_{CL}$, $w = w_{CL}$ |

For a given film casting problem, the values of the velocities at the die and roll are provided, which allows the calculation of $u_{die} = \Delta t \cdot \dot{u}_{die}$ and $u_{roll} = \Delta t \cdot \dot{u}_{roll}$. In Table 3.1, the subscript *CL* refers to the centre line incremental displacements, which are handled

differently than the constraints at the die and roll. When the *CL* constraint applies, all of the appropriate degrees of freedom in a given column, say column *j*, are constrained to the same value as that corresponding to the dof at the line of symmetry. That is, using the node numbering shown in Figure 3.3, $u_{ij} = u_{CLj}$ and $w_{ij} = w_{CLj}$, where *i* is the row number (2 to 4) and *j* is the column number. This constraint is used for all the columns that are located in the air-gap. When the constraint $u_{ij} = u_{CLj}$ is active all the columns of nodes will remain parallel to the die. If the $w_{ij} = w_{CLj}$ constraint is also in effect, then the thickness across a given column of nodes is constant.

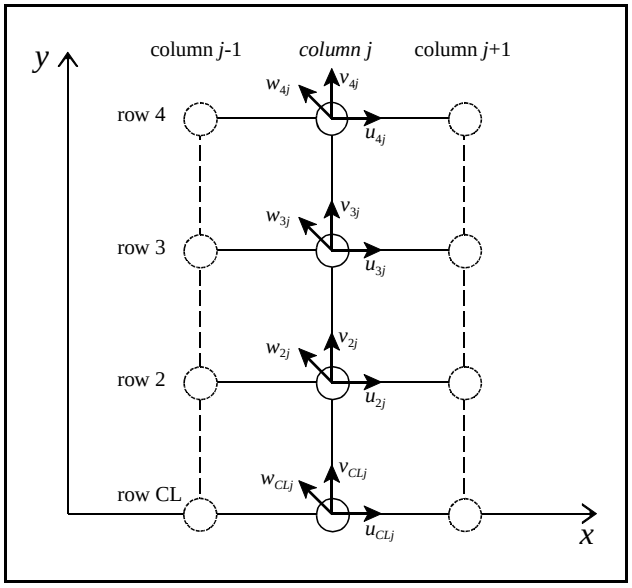


**Figure 3.3** A sample of several columns and rows of the finite element mesh

**3.4 Solve for the Nodal Displacements**

To find the displacement degrees of freedom, a fully implicit creep algorithm (Stolle 1991) is used. Owing to the linearization of the equations, an iterative scheme is required to converge to an equilibrium solution within each time step. On the first pass, the finite element equations for equilibrium can be expressed as follows, using the notation of Zienkiewicz (1977):

$$\int_V \boldsymbol{B}^T \boldsymbol{D}^{ve} \boldsymbol{B}\, dV\, \boldsymbol{a} = \boldsymbol{R} - \int_V \boldsymbol{B}^T \boldsymbol{\sigma} dV + \int_V \boldsymbol{B}^T \Delta\boldsymbol{\sigma}^c dV \tag{3.1}$$

with

$$\boldsymbol{D}^{ve} = \boldsymbol{D} - C_1 \boldsymbol{D} \frac{\partial q}{\partial \boldsymbol{\sigma}} \left( \frac{\partial F}{\partial \boldsymbol{\sigma}} \right)^T \boldsymbol{D} \tag{3.2}$$

$$\Delta\boldsymbol{\sigma}^c = C_1 F\, \boldsymbol{D} \frac{\partial q}{\partial \boldsymbol{\sigma}} \tag{3.3}$$

$$C_1 = [1 + (H_e + H_c)]^{-1},\ H_e = \left( \frac{\partial F}{\partial \boldsymbol{\sigma}} \right)^T \boldsymbol{D} \frac{\partial q}{\partial \boldsymbol{\sigma}},\ H_c = -\frac{\partial F}{\partial \varepsilon_q^c} \tag{3.4}$$

where $F = \Delta t \cdot \dot{\varepsilon}_q^c$, $\boldsymbol{a}$ is the dof vector for the in-plane displacement increments ($u$ and $v$), $\boldsymbol{R}$ is the load vector, $V$ is the volume of the domain, $\boldsymbol{B}$ is a matrix such that $\Delta\boldsymbol{\varepsilon} = \boldsymbol{B}\boldsymbol{a}$, $\Delta\boldsymbol{\sigma}^c$ is the creep stress increment, and $\boldsymbol{D}^{ve}$ is the viscoelastic constitutive matrix, which may correspond to nonlinear behaviour. It should be recognized that at this stage of the calculations $\boldsymbol{a}$ represents a first estimate for the change in displacements. For subsequent passes within an equilibrium iteration loop, the finite element equations, which provide a correction for $\boldsymbol{a}$, simplify to

$$\int_V \boldsymbol{B}^T \boldsymbol{D} \boldsymbol{B}\, dV\, \Delta \boldsymbol{a} \;=\; \boldsymbol{R} \;-\; \int_V \boldsymbol{B}^T \boldsymbol{\sigma}\, dV \qquad \textbf{(3.5)}$$

with $\boldsymbol{a} \leftarrow \boldsymbol{a} + \Delta\boldsymbol{a}$, where the right arrow notation represents the assignment of a value to the variable $\boldsymbol{a}$ (Rojiani 1996: p65). In Equations 3.1 and 3.5, the so-called initial stress matrix $\mathbf{K}_\sigma$, which is usually included for an updated reference configuration formulation (Stolle and Schad 1992), is not introduced, as it was found to have little influence on the final results for the class of problems addressed in this thesis. The book-keeping indices denoting the time step have been left out of the above equations to simplify the notation. A derivation of the implicit creep algorithm and an expansion of its terms are provided in Appendices A and C.

As the equilibrium equation is applied to the membrane, $\Delta\boldsymbol{a}$ does not contain the out-of-plane component of the incremental displacement $\Delta w$. To find $\Delta w$, the continuity equation (Equation 2.2) is multiplied by the trace of the virtual strain tensor $\delta(\Delta\boldsymbol{\varepsilon})$, which is consistent with the virtual displacements, and is then integrated over the film's domain

$$\int_V (\delta(\Delta\varepsilon_{xx}) + \delta(\Delta\varepsilon_{yy}) + \delta(\Delta\varepsilon_{zz}))(\Delta\varepsilon_{xx} + \Delta\varepsilon_{yy} + \Delta\varepsilon_{zz})\, dV = 0 \qquad \textbf{(3.6)}$$

Equation 3.6 has the advantage that it preserves the units of work done, as the change in the virtual volumetric work done can be expressed as $\delta(\Delta W_v) = \mathrm{tr}(\delta\Delta\boldsymbol{\varepsilon})\cdot\Delta p$ and $\Delta p = \alpha\cdot\mathrm{tr}(\Delta\boldsymbol{\varepsilon})$, where $\Delta p$ is the change in pressure and $\mathrm{tr}(\Delta\boldsymbol{\varepsilon}) \rightarrow 0$ as $\alpha \rightarrow \infty$, for an incompressible material. Equation 3.6 can be simplified by observing that $\delta\Delta\varepsilon_{xx} = \delta\Delta\varepsilon_{yy} = 0$, since both $\Delta u$ and $\Delta v$ are specified by $\Delta\boldsymbol{a}$, which is known:

$$\int_V \delta(\Delta\varepsilon_{zz})\Delta\varepsilon_{zz}\,dV = -\int_V \delta(\Delta\varepsilon_{zz})(\Delta\varepsilon_{xx} + \Delta\varepsilon_{yy})\,dV \qquad \textbf{(3.7)}$$

The above equation can be expressed in the usual finite element notation, with the use of $\boldsymbol{B}_{zz}$, which contains the components of the $\boldsymbol{B}$ matrix that are used to calculate $\Delta\varepsilon_{zz}$

$$\int_V \boldsymbol{B}_{zz}^T \boldsymbol{B}_{zz}\,dV\,\Delta\boldsymbol{w} = -\int_V \boldsymbol{B}_{zz}^T(\Delta\varepsilon_{xx} + \Delta\varepsilon_{yy})\,dV \qquad \textbf{(3.8)}$$

in which $\Delta\boldsymbol{w}$ is the nodal values for $\Delta w$ and $(\Delta\varepsilon_{xx} + \Delta\varepsilon_{yy})$ can be calculated for each integration volume after $\boldsymbol{a}$ or $\Delta\boldsymbol{a}$ is determined from the equilibrium considerations.

For each time-step, the changes in the dof vectors are calculated repeatedly, until the convergence criteria satisfies a given tolerance (*toler*), as follows:

$$Max\left(\frac{\|\Delta\boldsymbol{a}\|}{\|\boldsymbol{a}\|}, \frac{\|\Delta\boldsymbol{w}\|}{\|\boldsymbol{w}\|}\right) \le toler \qquad \textbf{(3.9)}$$

where $\|\cdot\|$ implies the Euclidean norm of the vector in question.

### 3.5 The Radial Return Algorithm

After solving for the displacement increments the local stresses and strains are updated using a radial return algorithm similar to that presented in Borja and Lee (1990) and Stolle *et al*. (1997). In the radial return algorithm, the stress invariants *p* and *q*, which correspond to the pressure and the effective stress, respectively, are first updated and then used to scale the stress tensor $\boldsymbol{\sigma}$ and to update the effective creep strain $\varepsilon_q^c$. Since the creep

response of the constitutive equation (Equation 2.8) does not depend on the pressure, $p$ and $q$ may be updated in an uncoupled manner.

Updated values of $q$ may be expressed as

$$q = q_o + 3G\Delta\varepsilon_q - 3G\Delta\varepsilon_q^c = q_e - 3G\Delta\varepsilon_q^c, \text{ where } \Delta\varepsilon_q \equiv \sqrt{\frac{4}{3} J_2^{\varepsilon}} \qquad \textbf{(3.10)}$$

with $q_0$ as the initial value for $q$, $q_e$ as the elastic prediction for $q$ in the absence of creep, $G$ as the shear modulus, $J_2^{\varepsilon}$ as the second invariant of the strain deviator, and $\Delta\varepsilon_q$ and $\Delta\varepsilon_q^c$ as the increments in the effective strain for the total and creep responses, respectively. The equations for the invariants are provided in Appendix A. A closed-form solution for $\Delta\varepsilon_q^c$ can be found, as shown in Appendix D, by integrating the creep response over the time step $\Delta t$, with the assumption that the stress is constant over the time step, yielding

$$\Delta\varepsilon_q^c = \varepsilon_q^c[(n\varepsilon_q^c)^{-n}(n\varepsilon_q^c + \dot{\varepsilon}_q^c\Delta t)^n - 1] \qquad \textbf{(3.11)}$$

where $n$ is the constitutive parameter that determines the strain-hardening nature of the material. If Equations 3.10 and 3.11 are combined, then the following equation results

$$q = q_e - 3G\varepsilon_q^c[(n\varepsilon_q^c)^{-n}(n\varepsilon_q^c + \dot{\varepsilon}_q^c\Delta t)^n - 1] \qquad \textbf{(3.12)}$$

An iterative Newton-Raphson scheme is adopted to solve for $q$, as presented in Appendix E.

Once $q$ is determined, the deviatoric stress tensor $\boldsymbol{s}$ may be updated using the following scaling:

$$\boldsymbol{s} = \frac{q}{q_e}\boldsymbol{s}^e \qquad \textbf{(3.13)}$$

with $\boldsymbol{s}^e$ being the deviatoric stress tensor for the elastic stress that corresponds to the invariants $p_e$ and $q_e$, where $p_e$ is the elastic prediction for $p$ in the absence of creep.

To obtain the complete stress tensor, the value for $p$ must also be calculated. For the membrane formulation $\sigma_{zz} = s_{zz} - p = 0$ and $\mathrm{tr}(\boldsymbol{s}) = 0$; therefore, a simple relation exists for determining $p$ for any stress state; i.e.,

$$p = -(s_{xx} + s_{yy}) \tag{3.14}$$

The updated stress is obtained by using Equation 3.13, along with Equation 3.14 to calculate

$$\boldsymbol{\sigma} = -p\boldsymbol{I} + \boldsymbol{s} \tag{3.15}$$

where $\boldsymbol{I}$ is defined (see Appendix A) so that $p$ is added only to the normal stresses.

Finally, the change in the effective creep strain may be found by rearranging Equation 3.10 as follows:

$$\Delta\varepsilon_q^c = \frac{q_e - q}{3G} \tag{3.16}$$

With the increment of effective creep strain determined, the total effective creep strain can be updated as follows: $\varepsilon_q^c \leftarrow \varepsilon_q^c + \Delta\varepsilon_q^c$.

### 3.6 Solve for the Nodal Temperatures

The finite element equations for temperature are found by multiplying Equation 2.3 by a virtual temperature $\delta T$ and integrating over the volume of the film. After application

of the divergence theorem, introducing the 2D discretization for temperature, and the zero flux boundary conditions, the following is obtained:

$$\boldsymbol{H}\boldsymbol{T} + \boldsymbol{C}\dot{\boldsymbol{T}} = \boldsymbol{F} \tag{3.17}$$

with

$$\boldsymbol{H} = \int_A \boldsymbol{B}_T^T k \boldsymbol{B}_T h \, dA + \int_A \boldsymbol{N}_T^T \alpha \boldsymbol{N}_T \, dA \tag{3.18}$$

$$\boldsymbol{C} = \int_A \boldsymbol{N}_T^T \rho C \boldsymbol{N}_T \, dA \tag{3.19}$$

$$\boldsymbol{F} = \int_A \boldsymbol{N}_T^T \alpha T_{air} \, dA \tag{3.20}$$

where $\boldsymbol{T}$ is the temperature dof vector, $\dot{\boldsymbol{T}}$ is its time derivative, $A$ is the area of the film, $\boldsymbol{N}_T$ is a matrix such that $T = \boldsymbol{N}_T\boldsymbol{T}$, $\boldsymbol{B}_T$ is a matrix such that $\nabla T = \boldsymbol{B}_T\boldsymbol{T}$, $h$ is the film's thickness and the other terms are defined as in Section 2.4. The finite element matrices for the temperature analysis are expanded in Appendix A.

To calculate the transient temperature field a finite difference approximation for the time derivative is introduced as follows:

$$\dot{\boldsymbol{T}} = \frac{\boldsymbol{T}_{k+1} - \boldsymbol{T}_k}{\Delta t} \tag{3.21}$$

where the subscripts $k$ and $k$+1 refer to the current time and the next time step, respectively. A fully implicit algorithm is obtained if the above divided difference is assumed to represent the rate of change at the end of the current time step. If Equation 3.21 is substituted into

Equation 3.17, at the end of the current time step, then, after some manipulations, the following is obtained:

$$\left[ \boldsymbol{H} + \frac{\boldsymbol{C}}{\Delta t} \right] \Delta \boldsymbol{T}_k = \boldsymbol{F}_k - \boldsymbol{H}\boldsymbol{T}_k \qquad \textbf{(3.22)}$$

where $\boldsymbol{T}_{k+1} = \boldsymbol{T}_k + \Delta \boldsymbol{T}_k$. Equation 3.22 is linear; therefore, unlike the displacement dofs, $\Delta \boldsymbol{T}_k$ can be solved directly without any need for iteration.

### 3.7 Update Mesh, Update Temperatures, Output Results and Renumber the Mesh

Once the nonlinear solution has converged and the temperature changes have been determined, the time, the mesh, the temperature as well as other variables are updated. The mesh is not updated during the solution step to improve the stability of the algorithm by working from a previously converged solution for all of the intermediate calculations. After the update, the results for the displacement field, geometry, stresses, strains, total creep strain and temperatures are output to files. Following this, the mesh is checked to see if elements that are on the roll can be removed and reinserted back inside the die. Elements are removed from the roll after a column of elements spans the chill roll's width because these elements no longer contribute to the solution in the air-gap, which is the region of interest. They are removed by shifting the node numbers and element numbers ahead by one; this effectively deletes the information in the last elements. To add new elements inside the die, the first column of nodes and elements are redefined to take on the new element properties.

## 3.8 Average Strain Film Elements

To construct the finite element stiffness matrices an average strain approach is employed, as presented by Stolle (1992) and Stolle *et al*. (2000). The average strain approach, which is an alternative to Gauss quadrature, has the advantage of defining gradients for a region, rather than for a point. This suits the assumption that the film properties are averaged through its thickness. Another advantage for the average strain approach, which is beneficial for the deforming mesh of a UL formulation, is that the integrations are exact, even for distorted elements.

The finite element used for film casting, which is shown in Figure 3.4, is a special case of the three-dimensional brick element. One element is used across the entire half-thickness of the film because, although each element has a 3D geometry, only the first four nodes are necessary to fully describe its shape and behaviour. This is possible when the $x$ and $y$ coordinates, and the associated $u$ and $v$ displacements, are assumed not to vary across the thickness. Furthermore, the $z$-coordinate, and the associated $w$ displacement, are both assumed to be zero at the mid-plane of the film.

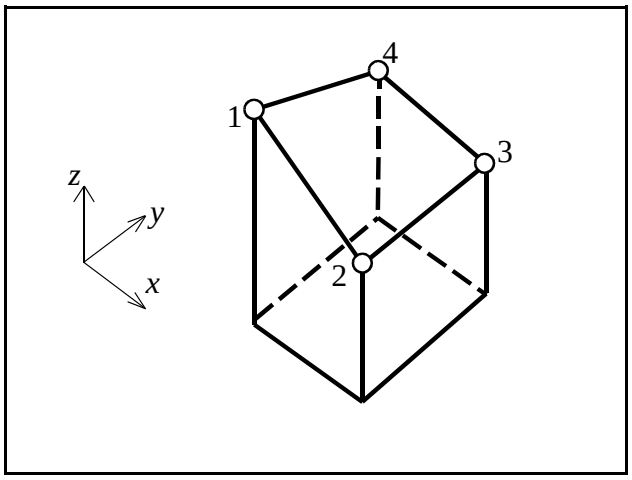


**Figure 3.4** A typical film element

Figure 3.4 shows a local film element (the global element uses the global numbering for the entire system). The local element must be divided into four sub-elements to prevent a singular stiffness matrix (Stolle 1992). Figure 3.5 shows the plan view of the film element and the four sub-elements in the *x*-*y* plane.

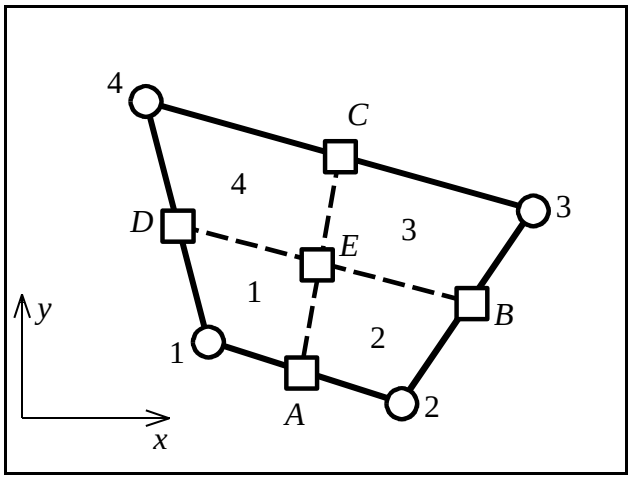


**Figure 3.5** Plan view of a film element and its sub-elements

The 3D strain tensor $\Delta\boldsymbol{\varepsilon}^d$ is calculated for the $d^{\text{th}}$ sub-element using the following equation:

$$\Delta\boldsymbol{\varepsilon}^d = \frac{1}{V^d}\int_{V^d}\int\int \boldsymbol{L}\begin{bmatrix} u \\ v \\ w \end{bmatrix} dx\,dy\,dz = \boldsymbol{B}^d\boldsymbol{a} \qquad \textbf{(3.23)}$$

where $V^d$ is the sub-element's volume. Starting from the above equation, the $\boldsymbol{B}^d$ matrix for the $d^{\text{th}}$ sub-element can be derived, as shown in Appendix F. The entries from $\boldsymbol{B}^d$ can then be used to construct the $\boldsymbol{B}$ matrices used to calculate the in-plane incremental displacements and the $\boldsymbol{B}_{zz}$ matrices used to calculate the out-of-plane incremental displacements.

As Figure 3.2 shows, the nodes of the film elements that are crossing the die or roll rarely coincide with the start location of these spatial boundary conditions. Figure 3.6 shows this more clearly via an exploded view of some typical elements as they cross the roll for the 1D, 1.5D and 2D cases. To address the problem of differences between the mesh and the spatial boundary conditions, two special elements are used: a die element and a roll element. For an element that is crossing the die or roll, the average shape function gradients are calculated using a redefined geometry. For these elements the *x*-coordinates are redefined to coincide with the *x*-coordinate of the die or roll. In the case of the die element, no further redefinition of the local coordinates is required, whereas for the roll element the *y* and *z* values must be interpolated to their values where the element crosses onto the roll. The redefined nodal locations for the 1D and 1.5D cases are shown in Figure 3.6 as trapezoids that coincide with the location of the roll. Figure 3.6 does not show redefined nodes for the

2D case, because the 2D elements cannot be treated in this simple manner. As the figure shows, two out of the three example elements for the 2D case have an odd number of nodes on the roll. This makes it impossible for a simple redefinition of the nodes to form a "new" quadrilateral element in the air-gap. Therefore, in the case of 2D analyses the die and roll elements are not employed. For the 2D case no special measures are taken to correct the elements at the die or roll.

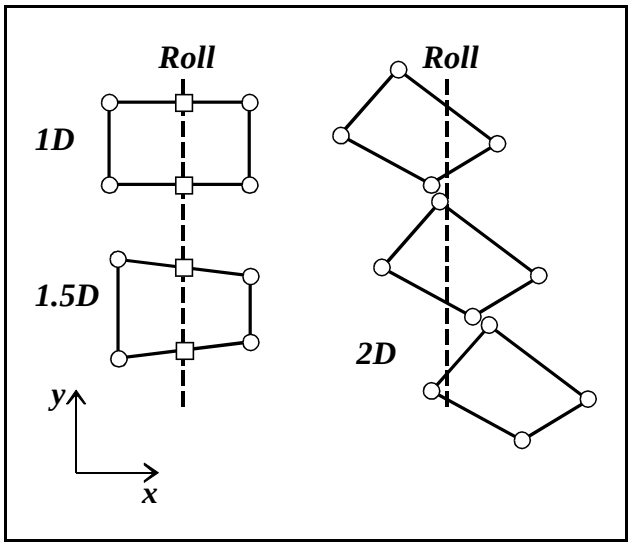


**Figure 3.6** Movement of typical film elements onto the roll

### 3.9 Improving the Efficiency of the Algorithm

The UL time-stepping algorithm is computationally expensive due to the large number of time steps required; therefore, some measures were taken to improve the overall efficiency.

i) The majority of the program's execution time is spent in the solver step, so an efficient $\boldsymbol{LDL}^T$ solver is used, similar to that presented in Bathe (1982). A conjugate gradient (CG) solver was also implemented, but it proved to be less efficient than the $\boldsymbol{LDL}^T$ solver. Although each solution for $\Delta\boldsymbol{a}$ is faster with the CG solver, more sub-iterations are necessary, owing to the approximate nature of each solution. Another measure for reducing the time associated with matrix decomposition is to reuse a previous matrix decomposition for subsequent calculations. Although the stiffness matrix changes from the first to the second sub-iterations (from Equation 3.1 to Equation 3.5), after the second pass the stiffness matrix no longer changes, so the same decomposition can be reused until the dof vector converges.

ii) Another approach to speed up the solver step is to solve for fewer degrees of freedom. Besides using an appropriately numbered and divided mesh, the degrees of freedom can be reduced by not solving for nodes inside the die, which as Figure 3.2 shows, represents a large number of nodes. The solution for these nodes is known *a priori* so there is no need to include them in the calculations. A straightforward method for eliminating these nodes from the calculations is to shift the constrained displacements inside the die, as shown in Table 3.1, from $u_{die}$ to zero. As the solver ignores the fixed dofs, the die dofs no longer need to be included in the calculations. To ensure that the proper gradients are calculated, the roll constraints must also be shifted, from $u_{roll}$ to $u_{roll} - u_{die}$. The *x*-direction nodal displacements are

shifted forward by $u_{die}$ before updating the mesh and writing the displacements to the output file.

iii) To reduce the number of degrees of freedom further, the middle of the width of a 2D film may sometimes be treated as a 1.5D problem. That is, a band of nodes, starting at the line of symmetry and forming a column parallel to the *y*-axis, are constrained to share one value for each of *u* and *w*. Besides reducing the total number of dofs, this 1.5D constraint also reduces the error that can accumulate in the mesh after many time steps. The source of this accumulated error is the boundary condition at the roll. If the situation occurs where a node at the line of symmetry is in the air-gap, while the node above it has moved a small distance onto the roll, then a small error exists, which may be exaggerated significantly over subsequent time steps.

iv) A final step to improving the speed of the program is the addition of another constraint to Table 3.1. If a node is in the air-gap and it is on the leading edge of the film, then it is constrained to have a value that gradually increases from $u_{die}$ to $u_{roll}$ as it moves from the die to the roll. This constraint is only active at the beginning of a simulation, when the mesh has not yet reached the chill roll. It is intended to reduce the number of time steps necessary for the film to reach the roll. Moreover, by gradually increasing the velocity of the leading edge, the film naturally acquires some of the characteristics of its eventual solution.

## 3.10 The Computer Implementation of the Algorithm

The numerical algorithm described in this chapter was programmed using Borland Delphi, which is a version of the Pascal language that incorporates object-oriented features and rapid application development using visual components. The program was written to accomplish the following tasks: generate the initial meshes and input files, implement the time-stepping algorithm and generate the output files. Post-processing was done using Matlab to view the time histories and Quattro-Pro and Tecplot to visualize the data at different instants in time. The majority of the simulations for this thesis were run on a Pentium II computer with 128 MBytes of RAM.

The time required to complete the simulations varied depending on two factors: the assumed dimensionality of the problem and the draw ratio. In general, when the problem is assumed 1D, the simulations take less time than for a 1.5D or 2D simulation, because the 1D problem does not require additional elements in the transverse direction. The draw ratio is an important factor in the overall simulation time because, as presented in future chapters, when all other parameters are held constant the higher the draw ratio the longer the duration of the transient behaviour. For a 1D problem at a low draw ratio, the simulation time is approximately one hour. At higher draw ratios the simulations may take eight hours or more. In the case of 1.5D and 2D simulations, the processing time can range from a few days to over a week for 2D problems operating at high draw ratios.

# Chapter 4 Comparison of UL and E Constitutive Equations

Information on the material properties of many polymers can be found in the chemical engineering literature, however these properties do not map directly onto the UL constitutive equation presented in Chapter 2. For the cases of a viscous fluid and a linear viscoelastic fluid, it is possible to mathematically relate the common E equations to the proposed UL equations. In the case of nonlinear viscoelasticity however, the mapping between the constitutive equations in the E and UL frameworks is unclear. As a consequence of this, caution must be employed when comparing the results of this study to observations in the film casting literature when nonlinear constitutive equations are involved.

Section 4.1 relates the UL constitutive parameters to the power-law fluid often used in the polymer processing literature. Section 4.2 presents the Maxwell element and how it is typically generalized in the UL and E frameworks. In the case of a linear Maxwell element, the parameters of the UL and E versions can be related, as shown in Section 4.3. The simple mapping however does not apply for the nonlinear constitutive equations, as demonstrated in Section 4.4, where the nonlinear responses are compared for the case of a constant rate of uniaxial extension. Throughout this chapter the index notation is used to represent vectors and tensors and the Einstein summation convention is assumed to apply. This notation differs from that in the other chapters, where bold face symbols and tensors

written as column vectors are employed. The change in notation is made to simplify the presentation and to highlight the fact that the discussion in this chapter is more general, in that it refers to stress and strain measures for any problem, not just the film casting problem.

### 4.1 Power-Law Viscous Fluids

In the E framework most often used in fluid mechanics, the power-law constitutive equation can be written as

$$\tau_{ij} = 2K\dot{II}^{\beta-1}D_{ij}, \quad \dot{II} = \sqrt{2D_{ij}D_{ij}} \qquad \textbf{(4.1)}$$

where $\tau_{ij}$ is termed the extra-stress tensor, $D_{ij}$ is the rate of deformation tensor, $K$ and $\beta$ are constants, and $\dot{II}$ is proportional to the second invariant of the rate of deformation tensor. Appendix H shows how Equation 4.1 can be related to the UL constitutive equation presented in Section 2.5 by taking the following into account:

i) the extra-stress tensor has the same definition as the deviatoric stress tensor ($\tau_{ij} = s_{ij}$);

ii) for viscous materials (low relaxation times) the elastic strain rate is small, so that $\dot{\varepsilon}_{ij}$ is approximately equal to $\dot{\varepsilon}^{c}_{ij}$;

iii) for small displacement gradient components, $\dot{\varepsilon}_{ij}$ is approximately equal to $D_{ij}$ (Malvern 1969: p162); and,

iv) the material is assumed to have no strain-hardening ($n = 1.0$).

The UL constitutive parameters in terms of the power-law parameters are as follows:

$$m = \frac{1}{\beta} \qquad \textbf{(4.2)}$$

and

$$A = 3^{\frac{-\beta-1}{2\beta}} K^{\frac{-1}{\beta}} \qquad \textbf{(4.3)}$$

A special case of the power-law fluid is the Newtonian fluid, which is obtained when $\beta = 1$. In this case Equations 4.2 and 4.3 simplify to $m = 1$ and $A = 1/(3K)$. To further highlight the Newtonian fluid, two symbols are introduced: $\eta^s$ and $\eta^c$, which are termed the shear and creep viscosities, respectively. These viscosities are related to $K$ and $A$, and to each other via

$$K = \eta^s \ , \quad A = \frac{1}{2\eta^c} \ , \quad \textit{and} \ \eta^c = \frac{3}{2}\eta^s \qquad \textbf{(4.4)}$$

## 4.2 UL and E Generalizations of a Maxwell Element

A linear Maxwell element consists of a spring and dashpot in series, as shown in Figure 4.1. The corresponding constitutive equation for the Maxwell element is (Joseph 1990: p2)

$$\sigma + \lambda\dot{\sigma} = 2\eta^s \dot{\gamma} \ , \ \lambda = \frac{\eta^s}{G} \qquad \textbf{(4.5)}$$

where $\sigma$ is the force in the element, which is the same force in the spring and in the dashpot, and $\dot{\gamma}$ is the sum of the rate of straining in the spring and dashpot ($\dot{\gamma} = \dot{\gamma}^s + \dot{\gamma}^d$).

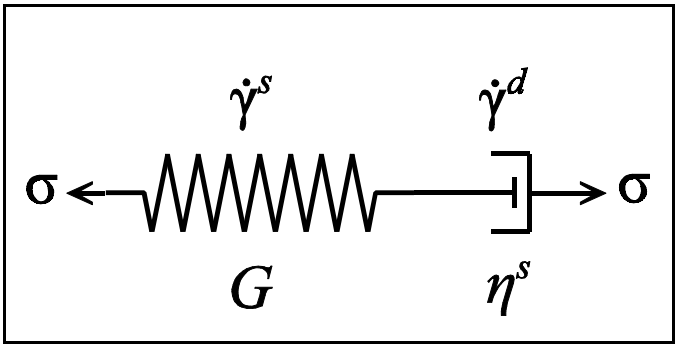


**Figure 4.1** A Maxwell element

Both the UL and E forms of the Maxwell fluid are based on generalizations of the linear Maxwell element shown above. The generalizations have to address two points: i) how to extend the one-dimensional element to multiple dimensions; and, ii) how to accommodate large deformations. Table 4.1 shows how these points are typically addressed in each framework.

**Table 4.1 UL and E Generalizations of the 1D Maxwell Element**

| **Framework** | **New σ** | **New $\dot{\gamma}$** | **Large Deformations** |
|---|---|---|---|
| UL | $s_{ij}$ | $\frac{\Delta\varepsilon_{ij}}{\Delta t} \approx \dot{\varepsilon}_{ij}$ | follow the material |
| E | $s_{ij}$ | $D_{ij}$ | convected derivative for the stress |

As Table 4.1 shows, both the UL and E frameworks generalize the force as a deviatoric stress tensor. The constitutive response is written in terms of the deviatoric stress because the material is assumed to be incompressible. Large deformations in the UL approach are accommodated by following the material. The E formulation, on the other

hand, does not directly follow the material; it focuses attention on a point in space. Therefore, the E formulation employs convected derivatives for the rate of change of stress. Convected derivatives are derived so that the constitutive equation is objective; that is, a stress rate is chosen that is frame-indifferent (Malvern 1969: p402). Convected derivatives account for the mass movement of the material, its rotation, and in some cases its deformation. An in-depth discussion of the convected derivatives can be found in Oldroyd (1950), Lodge (1974) and Bird (1987). A unique definition for convected derivatives does not exist, although one popular form is the upper convected derivative, which is presented in Section 4.4.

From the above discussion it appears that the UL formulation provides a more direct analog of the original Maxwell element. The E formulation is more complicated, and has two inconsistencies that are worth noting: the rate of strain tensor is not equivalent to the rate of deformation tensor, except in the case of small displacement gradients (Malvern 1969: p162), and, although the convected derivative for stress and the rate of deformation tensor are both objective, there is an inconsistency in that they may not always be chosen so as to be conjugate to one another in the energy sense. Given the differences between the UL and E formulations of the Maxwell element, it seems unlikely that the formulations describe the same constitutive response, except possibly in the linear case, which is discussed in the next section.

### 4.3 The Linear Maxwell Fluid

In this section the discussion is limited to small displacements (say less than 5%), so that the nonlinearities associated with convected derivatives need not be considered and a linear constitutive equations can be assumed. In the chemical engineering literature a linear small strain Maxwell fluid is often written as (Joseph 1990: p6)

$$\tau_{ij} + \lambda\dot{\tau}_{ij} = 2\eta^s D_{ij} \qquad \textbf{(4.6)}$$

As Appendix H shows, the UL constitutive equation may be written in an equivalent form, by using assumptions i), iii) and iv) from Section 4.1, and by setting $m = n = 1$

$$s_{ij} + \lambda\dot{s}_{ij} = 2\eta^s\dot{\varepsilon}_{ij} \qquad \textbf{(4.7)}$$

Appendix H also shows several equivalent definitions for the relaxation time

$$\lambda = \frac{\eta^s}{G} = \frac{2\eta^c}{3G} = \frac{1}{3GA} = \frac{1}{EA} \qquad \textbf{(4.8)}$$

### 4.4 UL and Nonlinear E Constitutive Response for a Constant Rate of Extension

In the previous section small strains were assumed, but in this section larger strains are allowed; therefore, the constitutive response becomes nonlinear. To simplify the comparison of the constitutive response in the E and UL formulations, this section focuses on the case of a constant rate of uniaxial extension, for which the equations are 1D and rotation is not a factor. Figure 4.2 shows the boundary conditions for the uniaxial extension problem. The initial length of

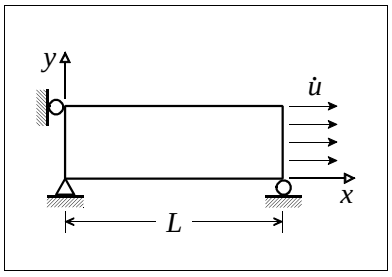


**Figure 4.2** Uniaxial extension

the specimen is $L_0$. For a constant rate of natural strain ($\dot{\varepsilon}$) the natural strain ($\varepsilon$) can be determined by integration, and the length ($L$) as a function of time can be determined as follows:

$$\varepsilon = \ln(\frac{L}{L_0}) = \dot{\varepsilon}t, \qquad \therefore L = L_0 e^{\dot{\varepsilon}t} \tag{4.9}$$

Equation 4.9 can be used to determine the variation of the velocity at the free end ($\dot{u}$) required to keep the extension rate constant

$$\dot{u} = \frac{dL}{dt} = \dot{\varepsilon}L_0 e^{\dot{\varepsilon}t} \tag{4.10}$$

In the UL framework the constitutive equation (Equation 4.7) for a constant uniaxial extension simplifies to

$$\dot{\sigma}_{xx} = E(\dot{\varepsilon} - \frac{\sigma_{xx}}{2\eta^c}) \tag{4.11}$$

This linear differential equation can be solved using the initial condition $\sigma_{xx} = 0$ to yield

$$\sigma_{xx} = 2\eta^c(1 - e^{-\frac{t}{\lambda}}) \tag{4.12}$$

As mentioned previously, a popular nonlinear version of the Maxwell fluid in an E formulation is the upper convected Maxwell (UCM) fluid, which can be written as

$$\lambda\check{\tau}_{ij} + \tau_{ij} = 2\eta^s D_{ij} \tag{4.13}$$

with the upper convected derivative defined as

$$\check{\tau}_{ij} = \frac{D\tau_{ij}}{Dt} - L_{ik}\tau_{kj} - \tau_{ik}L_{jk} \qquad \textbf{(4.14)}$$

where $L_{ij}$ is the velocity gradient tensor and $D/Dt$ is the material derivative. In the case of a constant rate of uniaxial extension, the stress in a UCM fluid as a function of the natural strain rate $\dot{\varepsilon}$ is found in Appendix I to be

$$\sigma_{xx} = \frac{2\eta^s\dot{\varepsilon}}{1 - 2\lambda\dot{\varepsilon}}\left(1 - e^{(2\dot{\varepsilon}-\frac{1}{\lambda})t}\right) + \frac{\eta^s\dot{\varepsilon}}{1 + \lambda\dot{\varepsilon}}\left(1 - e^{(-\dot{\varepsilon}-\frac{1}{\lambda})t}\right) \qquad \textbf{(4.15)}$$

### 4.4.1 A Comparison of the UL and UCM Solutions

To see how the two solutions compare the same problem was solved in both frameworks for strain rates of 0.2, 1.0 and 2.5 $s^{-1}$. The material properties for the UL and UCM constitutive equations are shown in the UCM and UL columns of Table 4.2.

**Table 4.2 Comparison Between the UL and E Constitutive Parameters**

| **Material Parameter** | **UCM** | **UL** | **Best Fit UL** |
|---|---|---|---|
| $\lambda$ | 0.255 s | 0.255 s | 0.02066 s |
| $\eta^s$ | 1000 Pa·s | 1000 Pa·s | - |
| $A$ | - | $1/(3\eta^s) = 3.333 \times 10^{-4}$ | 0.003227 |
| $m$ | - | 1 | 0.6659 |
| $n$ | - | 1 | 0.8608 |

Figure 4.3 shows that the UL and UCM solutions are considerably different, most notably at higher strains and for the higher strain rate.

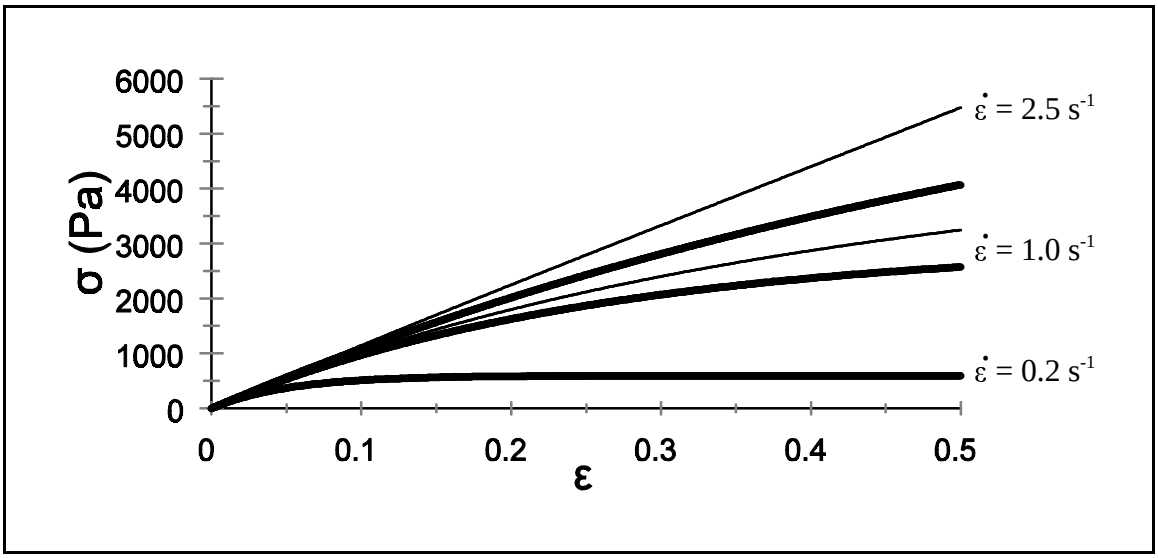


**Figure 4.3** Stress versus natural strain for a constant rate of uniaxial extension with the UL (▬) and the UCM (–) versions of Maxwell's equation

To further highlight the differences in the constitutive response between the UL and UCM versions of the Maxwell equation, the UL equation was fit to the UCM results using a Hooke and Jeeves algorithm, which is explained in Appendix J. Figure 4.4 shows that the agreement has been much improved. To accomplish this improvement however the material properties for the UL version had to be greatly modified, as shown in Table 4.2. The relaxation time has been reduced, the linear viscosity has been replaced with extensional thickening and the material has become strain-hardening. It is worth noting that the best fit parameters are not unique, since other combinations of the parameters will also significantly reduce the differences between the UL and UCM solutions.

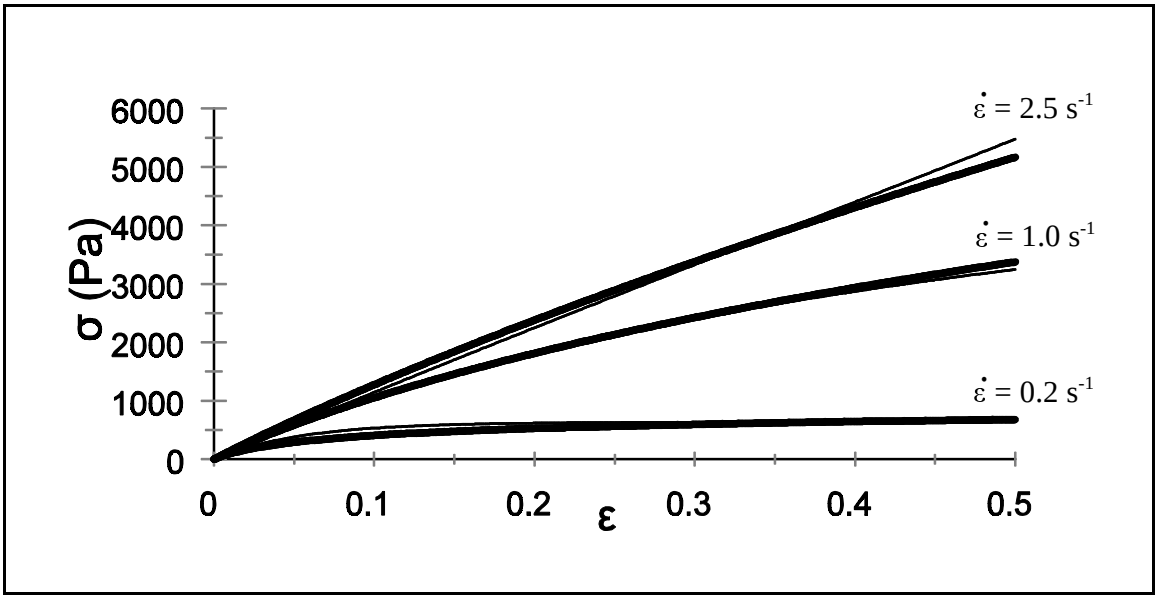


**Figure 4.4** Stress versus natural strain for a constant uniaxial extension with the UL (▬) parameters fit to the UCM (-) equation

Although the fit has been greatly improved for the uniaxial extension, such good agreement does not necessarily exist for other loading configurations when using the optimum parameters. For instance, if the UCM and best fit UL parameters are used to predict the stresses for an equibiaxial extension, different results are obtained, as shown in Figure 4.5. The equation for stress versus strain for the UCM fluid under equibiaxial extension is derived in Appendix I. This simple example demonstrates the fact that model calibration using one material test does not guarantee good agreement for other loading cases.

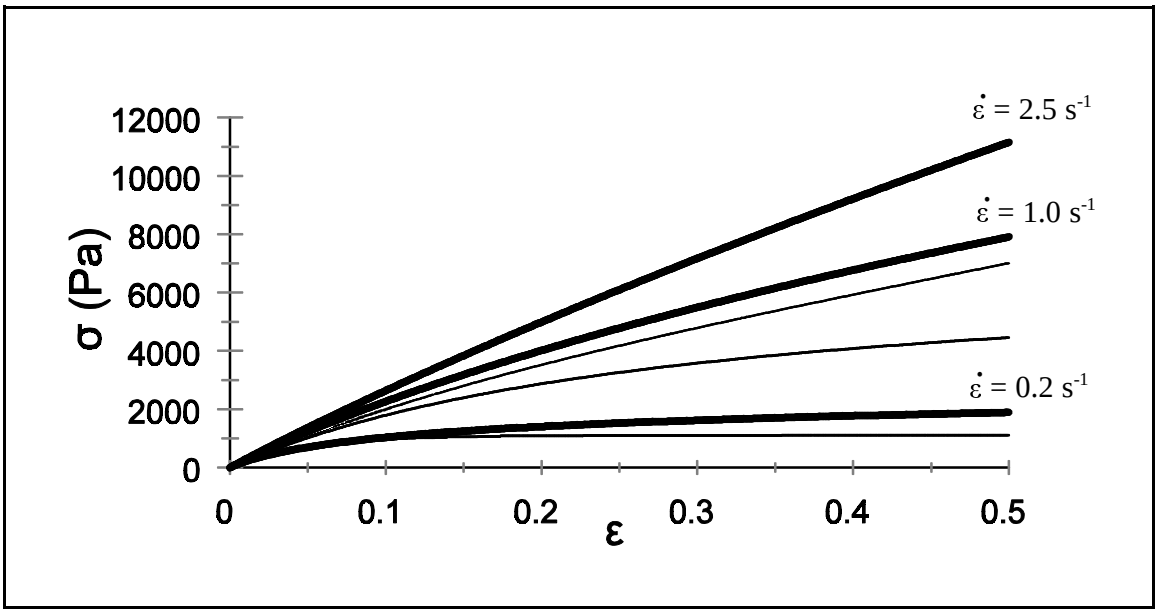


**Figure 4.5** Stress versus natural strain for a constant biaxial extension using the UL (▬) parameters fit to the uniaxial UCM (–) equation

### 4.4.2 A Comparison of The Special Cases: The Viscous and Elastic Responses

To better highlight the differences between the UL and E versions of the Maxwell equation, the behaviour corresponding to the viscous and elastic limits of the viscoelastic equations presented in Section 4.4 are considered. The viscous solution is found by taking the limits of Equations 4.12 and 4.15 as $G$ approaches infinity so that the relaxation time approaches zero. The stress in the $x$-direction is found to be identical for both formulations, with

$$\sigma_{xx} = 2\eta^c\dot{\varepsilon} = 3\eta^s\dot{\varepsilon} \qquad \textbf{(4.16)}$$

To find the elastic solution, the limits of Equations 4.12 and 4.15 are taken as $\eta^s$ approaches infinity so that $\lambda$ approaches infinity. In this case the stresses for the two cases are different. For the UL framework

$$\sigma_{xx} = E\varepsilon \tag{4.17}$$

where $\varepsilon$ is the natural strain. The elastic limit for Equation 4.15 requires the application of L'Hospital's rule to the fractions at the beginning of each term to yield the nonlinear equation

$$\sigma_{xx} = \frac{E}{3}(e^{2\varepsilon} - e^{-\varepsilon}) \tag{4.18}$$

This observation suggests that the nonlinearity of the elastic response of the UCM fluid can account for the increasing difference between the two formulations with increasing strain rate, as illustrated in Figure 4.3. Since the UL formulation is linear in the elastic response, a nonlinear creep response is required to take into account the nonlinear behaviour of the UCM formulation, as shown by the fitted parameters in Table 4.2.

Although the viscous response is the same in the two frameworks, the elastic response is different. Specifically, the strain measure used is different between the two formulations. The 1D elastic response discussed above generalizes to approximate the following in the UL framework:

$$\sigma_{ij} = -p\delta_{ij} + 2G\varepsilon_{ij}^{e} \tag{4.19}$$

In Equation 4.19, the strain measure is the natural strain $\varepsilon_{ij}^{e}$, which corresponds to integrating the rate of deformation tensor over time while holding the material constant. It is worth emphasizing that it is the material particle that is held constant, not the location in space. As

pointed out by Malvern (1969: p151) the integration of the natural strain increments has no physical meaning unless the material particle is being followed. Malvern also observes that although the natural strain increments are tensors, the integral of the natural strains while holding the material particle constant is not a tensor.

For the E framework the multi-dimensional elastic response for a UCM fluid with an infinite relaxation time is given by

$$\sigma_{ij} = -p\delta_{ij} + G(B_{ij} - \delta_{ij}) \qquad \textbf{(4.20)}$$

where $B_{ij}$ is the Finger, or left Cauchy Green, deformation tensor. This equation is derived in Appendix K.

From the above discussion it is clear that the UL and UCM equations are not equivalent. Moreover, it is apparent that the definition of the relaxation time in the UL formulation is different than that in the nonlinear E approach. Therefore, the viscoelastic simulations presented in the next chapters cannot be directly related to the cast film literature. Although the UL constitutive behaviour assumed in this thesis differs from the usual behaviour assumed using an E approach, this does not in itself indicate a shortcoming of the current approach. In fact, the UL framework has an intuitive appeal because constitutive laws are generally interpreted using a material point perspective, even for Eulerian equations. Therefore, one cannot clearly state that the E interpretation is more correct than the UL, and vice-versa.

# Chapter 5 One-Dimensional Film Casting

In 1D film casting simulations the complications of neck-in and edge-bead are not included, which simplifies the numerical algorithm and reduces the number of degrees of freedom required. Furthermore, the problems inherent with spatial boundary conditions and a material mesh are mitigated by the ability to redefine the element coordinates to coincide with the die and roll locations, as discussed in Section 3.8. Consideration of the 1D problem is not only motivated by the simplifications and improvements to the algorithm, the 1D problem has several other advantages, which include the following: i) the 1D assumption is a good approximation of many film lines, where the die width is much greater than the air-gap length; ii) the 1D simulations provide a simpler framework for examining the influence of the constitutive and thermal responses; and iii) the 1D problem can be solved in closed-form for some simple fluids, thus it provides a means to validate the numerical algorithm.

The main division of this chapter is between the stable and unstable simulations, which are discussed in Sections 5.1 and 5.2, respectively. In both sections the simulation results are first validated against the available closed-form solutions. Following this, parametric studies are performed to investigate the influence of the constitutive parameters ($m$, $n$, $\lambda$) and nonisothermal conditions. Smith and Stolle (2000b) presents material similar

to that in this chapter, but with a constitutive equation that allows for some compressibility in the elastic strains.

## 5.1 Stable Simulations

The simulation results presented in this section correspond to stable simulations; that is, the simulations were carried out until all of the transient behaviour damped out. Details on the transient behaviour and determination of stable versus unstable conditions are the subject of Section 5.2.

Section 5.1.1 validates the 1D algorithm for the film casting of a power-law fluid. Sections 5.1.2, 5.1.3 and 5.1.4 consist of parametric studies to look at the influence of strain-hardening, the relaxation time and nonisothermal conditions, respectively.

### 5.1.1 Comparison to the Closed-Form Solutions for Steady-State Film Casting

To validate the 1D algorithm, the numerical solution was compared to the closed-form solution, which is derived in Appendix G, for a power-law fluid. The simulation parameters are provided in Table 5.1, where *nel* stands for the total number of elements, which includes those inside the die and on the chill roll.

**Table 5.1 Film Casting Parameters for the 1D Simulations**

| Geometry | Boundary Conditions | Material Parameters | Numerical Parameters |
|---|---|---|---|
| $L$ = 0.1 m | $\dot{u}_{die}$ = 0.01 m/s | $m$ = 1.0 | *nel* = 200 |
| $h_{die}$ = 0.001 m | $\dot{u}_{roll} = \dot{u}_{die} Dr$ | $n$ = 1.0 | $\Delta t = 10^{-3}$ s |
| | $Dr$ = 10 | $\lambda$ = 0.002 s | *toler* = $10^{-2}$ |
| | | $\eta^s$ = 2000 Pa·s | |
| | | $A = 1/(3\eta^s) = 1.6667\times10^{-4}$ (Pa·s)$^{-1}$ | |
| | | $E = 1/(\lambda A) = 3.0\times10^{6}$ Pa | |

Figure 5.1 shows the numerical solutions for the dimensionless thickness and velocity distributions in the air gap for a viscous fluid ($m$ = 1), an extensional thickening fluid ($m$ = 0.75) and an extensional thinning fluid ($m$ = 1.25). The solutions for velocity, thickness and stress agree very well with the closed-form solutions, which are not shown on the figure because they are essentially coincident with the plotted curves. A convenient measure of error, which encapsulates the error in all of these variables, is the relative error in the rate of energy dissipation $\dot{W}^c$, which is defined as

$$\dot{W}^c = \int_V \dot{\boldsymbol{\varepsilon}}^{cT} \boldsymbol{\sigma}\, dV = \int_V \dot{\varepsilon}_q^c q\, dV \approx \left[ \sum_{i=1}^{ninteg} (\Delta\varepsilon_q^c q)_i\, V_i \right] / \Delta t \qquad \textbf{(5.1)}$$

where the subscript $i$ refers to the values for the $i^{th}$ integration volume and *ninteg* is the total number of integration volumes for the film. In the case of 1D and 1.5D film casting, the calculation of $\dot{W}^c$ uses the die and roll elements discussed in Section 3.8. For the simulations where $m$ is varied, the relative errors are 4.7 %, 0.56 % and 0.52 % for $m$ = 0.75,

1.0 and 1.25, respectively. The error can be decreased further by increasing the number of elements in the air-gap. This topic is discussed in detail in Section 8.2.

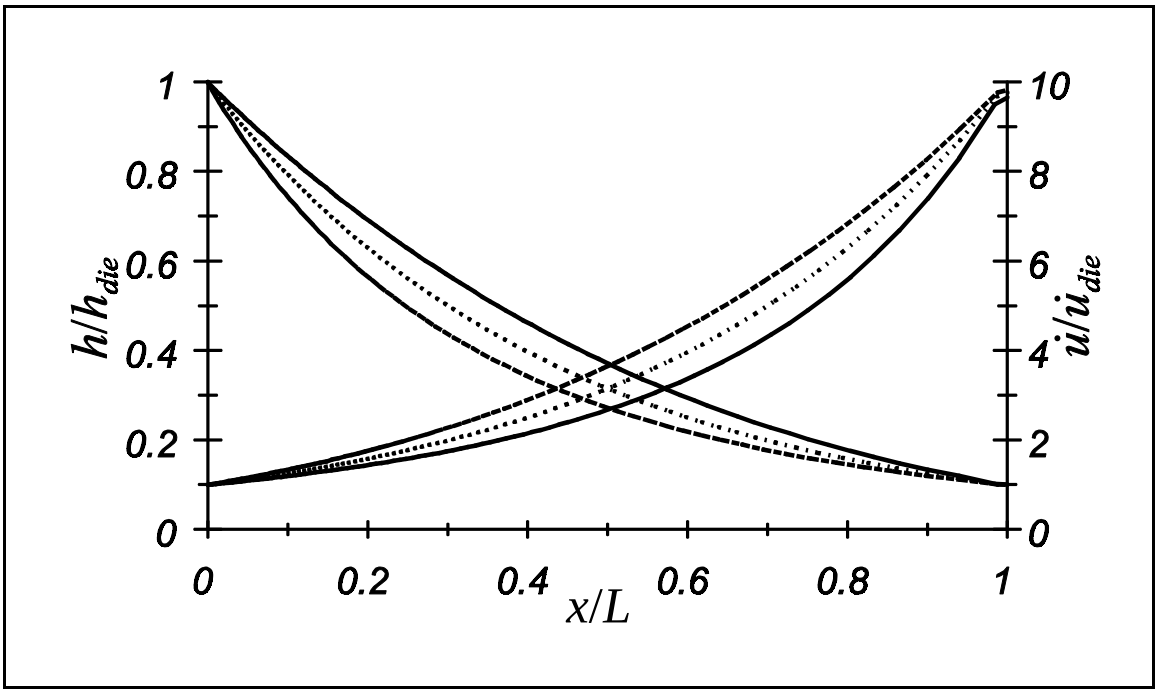


**Figure 5.1** Dimensionless thickness and velocity distributions in the air-gap with $m$ = 1.25 (—), 1.0 (···) and 0.75 (---)

### 5.1.2 Influence of Strain-Hardening on Stable Film Casting

The influence of the $m$ parameter of Equation 2.8 was presented in the previous section. This section considers the influence of the strain-hardening parameter $n$. To observe the influence of $n$, simulations were conducted using the simulation parameters of Table 5.1, with altered values of $m$ and $n$. Figure 5.2 show the simulation results for velocity and thickness in the air-gap. Strain-hardening is seen to increase the thickness gradient at the die, which seems reasonable as the material will become more difficult to deform as it

moves downstream and accumulates creep strain. The thickness gradient at the die is even further increased for a strain-hardening fluid with extensional thickening ($m = 0.75$). Again this behaviour is to be expected, given that extensional thickening is seen to follow the same trend, even in the absence of strain hardening (Figure 5.1).

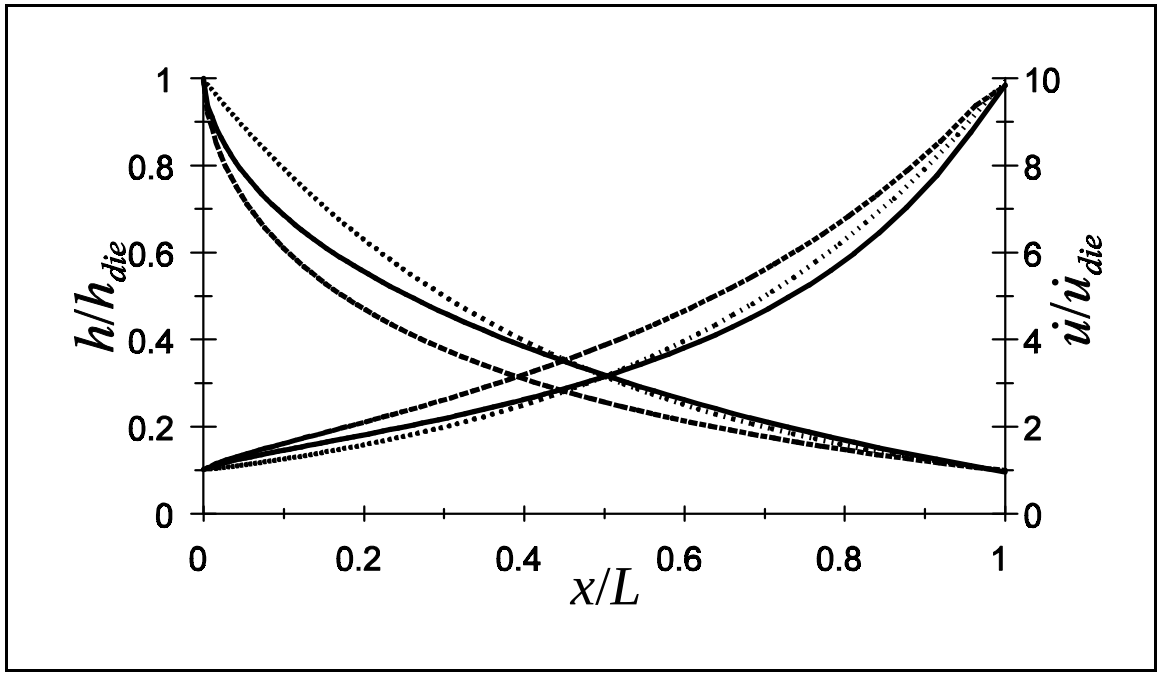


**Figure 5.2** Dimensionless thickness and velocity distributions in the air-gap with $m$ = 1.0, $n$ = 0.5 (––); $m$ = 0.75, $n$ = 0.5 (- - -) and $m$ = 1.0, $n$ = 1.0 (···)

### 5.1.3 Influence of the Relaxation Time on Stable Film Casting

To investigate the influence of the relaxation time, the simulation parameters of Table 5.1 were used again, but in this case the relaxation time was varied from 0.002 s to 0.5 s. Figure 5.3 shows how this change influences the velocity and thickness profiles. An increase in the relaxation time causes the thickness profile to approach a straight line, and the velocity

profile to change accordingly, to ensure that the continuity requirement is satisfied. This behaviour is qualitatively different from that observed in some published studies of film casting, where the velocity is seen to approach a linear profile (Alaie and Papanastasiou 1991). However, as explained in Chapter 4, the meaning of the relaxation time for the constitutive equation used in this thesis does not have the same meaning as that generally adopted in the film casting literature.

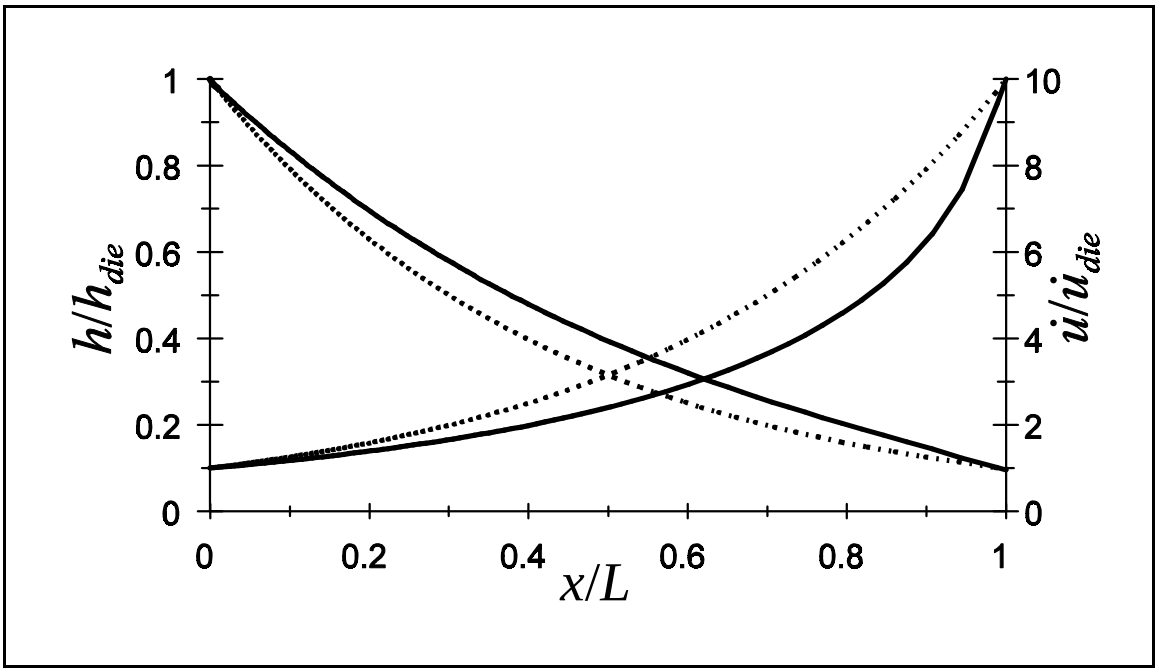


**Figure 5.3** Dimensionless thickness and velocity distributions in the air-gap with $\lambda$ = 0.5 s (––), and $\lambda$ = 0.002 s (···)

### 5.1.4 Influence of Nonisothermal Conditions on Stable Film Casting

The previous simulations were for isothermal film casting. To investigate the influence of heat transfer, on an approximately viscous fluid, the simulation parameters of

Table 5.1 were used together with the additional parameters provided in Table 5.2, and heat transfer coefficients $\alpha$ of 0, 20, and 40 W/(m$^2$ K). The parameters selected for Table 5.2 are typical parameters for polypropylene (PP).

**Table 5.2 Typical Nonisothermal Film Casting Parameters for PP**

| Boundary Conditions | Material Parameters |
|---|---|
| $T_{die}$ = 215 °C | $\rho$ = 910 kg/m$^3$ (Rauwendall 1986: p218) |
| $T_{air}$ = 30 °C | $k$ = 0.15 W/(m K) (Rauwendall 1986: p218) |
| $\alpha$ = 20 W/(m$^2$ K) | $C$ = 2100 J/(kg K) (Rauwendall 1986: p218) |
| | $Q/R$ = 5100 K (Tanner 1985: p353) |
| | $T_0$ = 190 °C (Tanner 1985: p353) |
| | $\eta_0^s = 1/(3A_0)$ = 3200 Pa·s (Tanner 1985: p353) |

Figure 5.4 shows how increasing heat transfer coefficients influences the velocity and thickness profiles. As the heat transfer coefficient increases, the thickness gradient at the die also increases. This behaviour is reasonable if one considers that as the film moves further downstream its temperature decreases and thus its viscosity increases. The lower upstream viscosity, when compared with that downstream, should force the film to deform more near the die, where there is less resistance to a higher rate of deformation. The same trends in the velocity and thickness profiles for viscous fluids with increasing heat transfer are observed in the E analysis of Smith (1997).

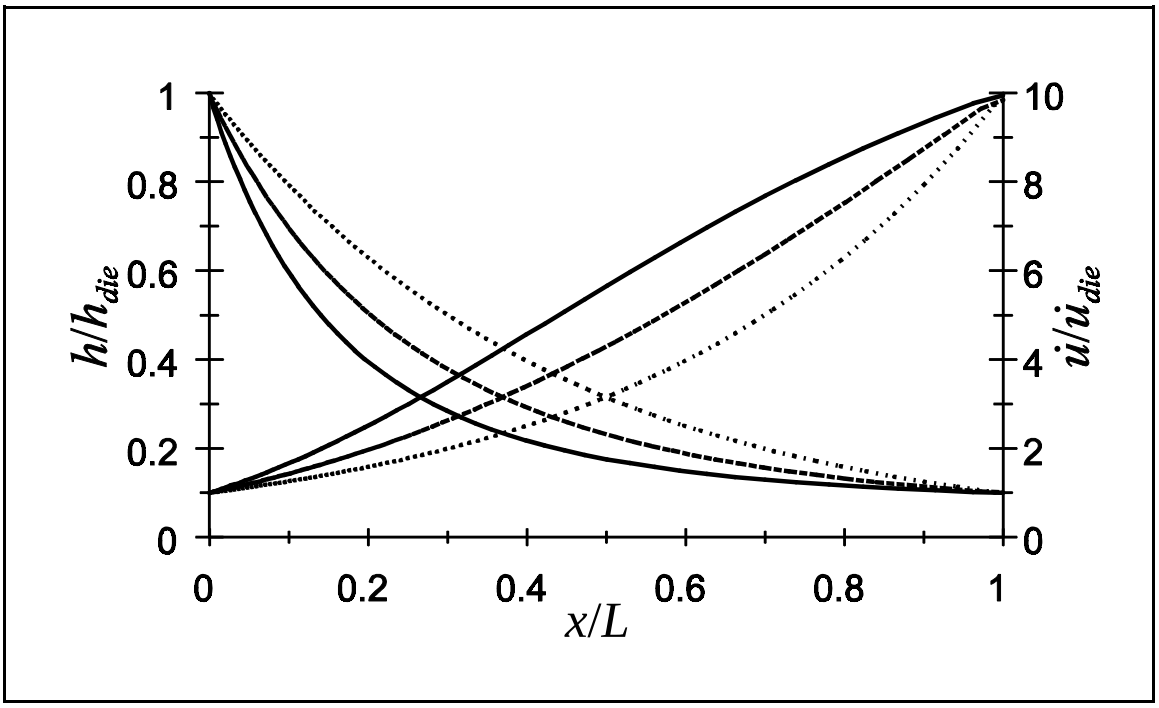


**Figure 5.4** Dimensionless thickness and velocity distributions in the air-gap with $\alpha$ = 0 (···), 10 (- - -) and 20 (–-) W/(m$^2$ K)

### 5.2 Instability in 1D Film Casting

In the previous sections, the transient behaviour of the film was not shown. As indicated previously, for each of the above simulations, the time-stepping was continued until the rate of change of all the variables, holding the spatial location constant, was negligible. However, for some materials and processing conditions, the spatial rate of change of the geometry does not approach zero, instead it continues to oscillate; this corresponds to instability or draw resonance. This fact places a limit on the parametric study results previously shown, since for a given draw ratio the film is only stable within a certain range

of the constitutive parameters. It is the purpose of this section to identify the stable ranges and to investigate further the phenomenon of draw resonance in 1D film casting.

Section 5.2.1 presents the approach for identifying instability as a response problem. This approach is used in Section 5.2.2 to 5.2.4 to examine the influence of the constitutive parameters ($m$, $n$ and $\lambda$) and nonisothermal conditions on the critical draw ratio.

### 5.2.1 Identification of Draw Resonance as a Response Problem

The critical draw ratio was identified by monitoring the thickness at the roll over time for successive integer values of the draw ratio. Only integer values are considered due to the uncertainty inherent in this approach. By definition, an upper bound for stability corresponds to the situation where large oscillations in a film's thickness do not damp out over time. This definition of stability does not require a constant thickness history, only one that stays reasonably bounded. An alternative approach is to define the processing conditions as stable if the time rate of change of $\dot{W}^c$ approaches zero as time progresses. The advantage of this definition is that the rate of energy dissipated is a scalar measure that depends on the changing configuration of the entire body, not just the thickness at the chill roll.

Figure 5.5 shows the thickness at the roll and the $\dot{W}^c$ histories, using the simulation parameters of Table 5.1, but with $Dr$ increased from 10 to 20. The thickness is normalized with the thickness expected by the continuity requirement ($h_{roll} = h_{die}/Dr$). An examination of this figure shows that after an initial increase in thickness the oscillations decrease. According to the proposed definition, this implies that the process is stable with $Dr = 20$.

It is noteworthy that this plot shows two frequencies. The higher frequency is likely associated with the imperfect satisfaction of the boundary conditions over each time step. Although this higher frequency makes for a noisy plot, it approximates the actual physics of the process where the boundary conditions likely migrate slightly over time. This conclusion is supported by the experimental data for film casting presented in Barq *et al*. (1990), who show noise, even for stable operations.

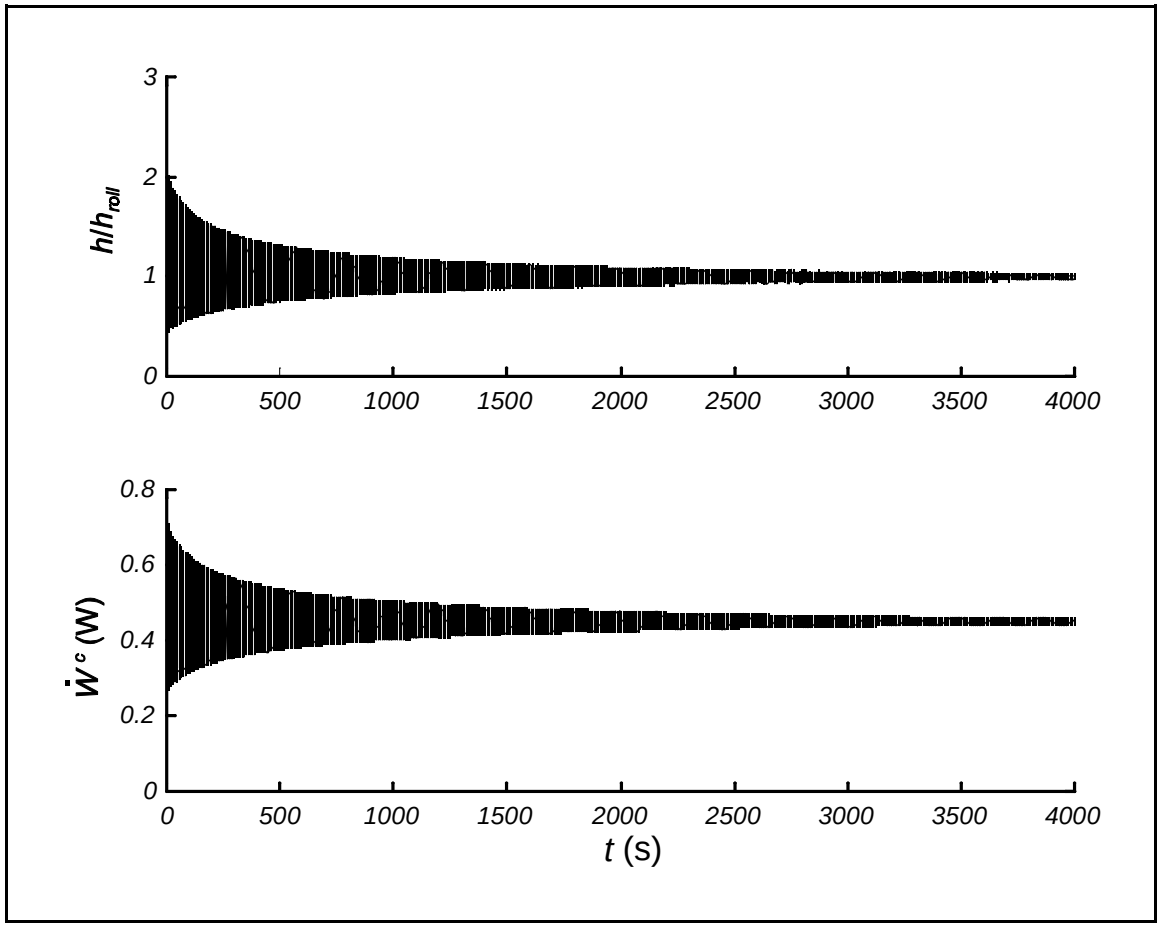


**Figure 5.5** Normalized thickness at the chill roll and rate of energy dissipation histories for $Dr = 20$

The time histories corresponding to a draw ratio of 21 are shown in Figure 5.6. Unlike at $Dr$ = 20, the amplitude of the oscillations in the final thickness and $\dot{W}^c$ do not decrease over time. Therefore, the film is considered to be unstable for $Dr$ = 21. This allows one to conclude that the critical draw ratio lies between 20 and 21, which agrees well with the theoretical prediction for a viscous fluid of $Dr_{cr} \approx 20.2$ (Yeow 1974).

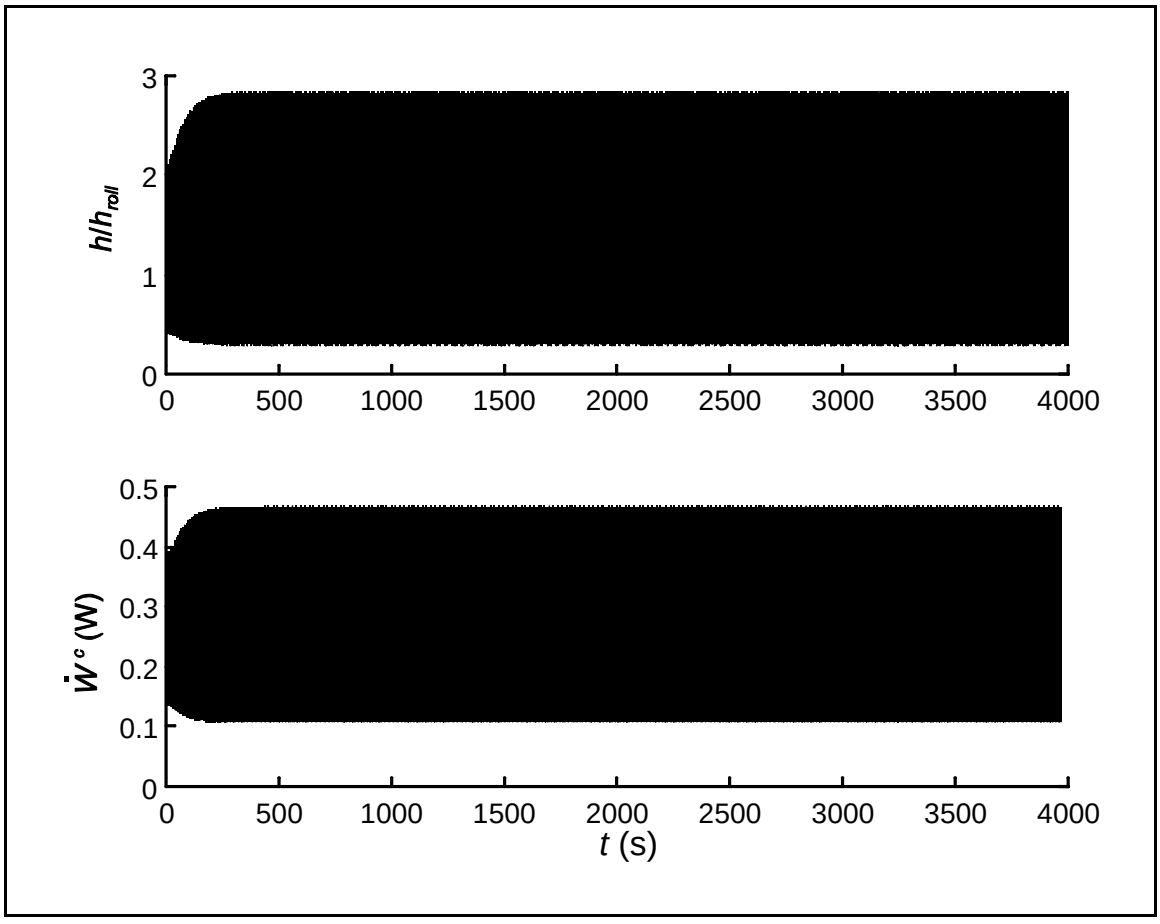


**Figure 5.6** Normalized thickness at the chill roll and rate of energy dissipation histories for $Dr$ = 21

### 5.2.2 Influence of *m* and *n* on Stability

The approach described in the previous section for an approximately viscous fluid is repeated here, using different constitutive parameters. All of the simulations of this section use the processing conditions and numerical parameters of Table 5.1, but the constitutive parameters are changed as indicated.

Figure 5.7 shows the dependence of the critical draw ratio on the extensional thinning/thickening parameter for fluids with and without strain-hardening. This figure also plots the closed-form solution for the critical draw ratio of a fluid without strain-hardening, as derived by Aird and Yeow (1983). The curve in Figure 5.7 for $n = 1.0$ agrees very well with theoretical expectations, although as the extensional thickening nature increases ($m < 1.0$), Figure 5.7 underpredicts the theoretically determined critical draw ratio. This is most likely a consequence of the numerical algorithm, which does not perform as well at the higher draw ratios required for these cases, because the downstream elements are considerably elongated. To partially compensate for the effect of the elongation of the downstream elements at higher draw ratios, the simulations used to produce the $m \leq 1$ points of Figure 5.7 employed 1600 elements, instead of the usual 200.

When strain-hardening is added, the shape of the curve is similar, but it is shifted to lower draw ratios. The mechanism that leads to this decrease in stability is unclear at this time.

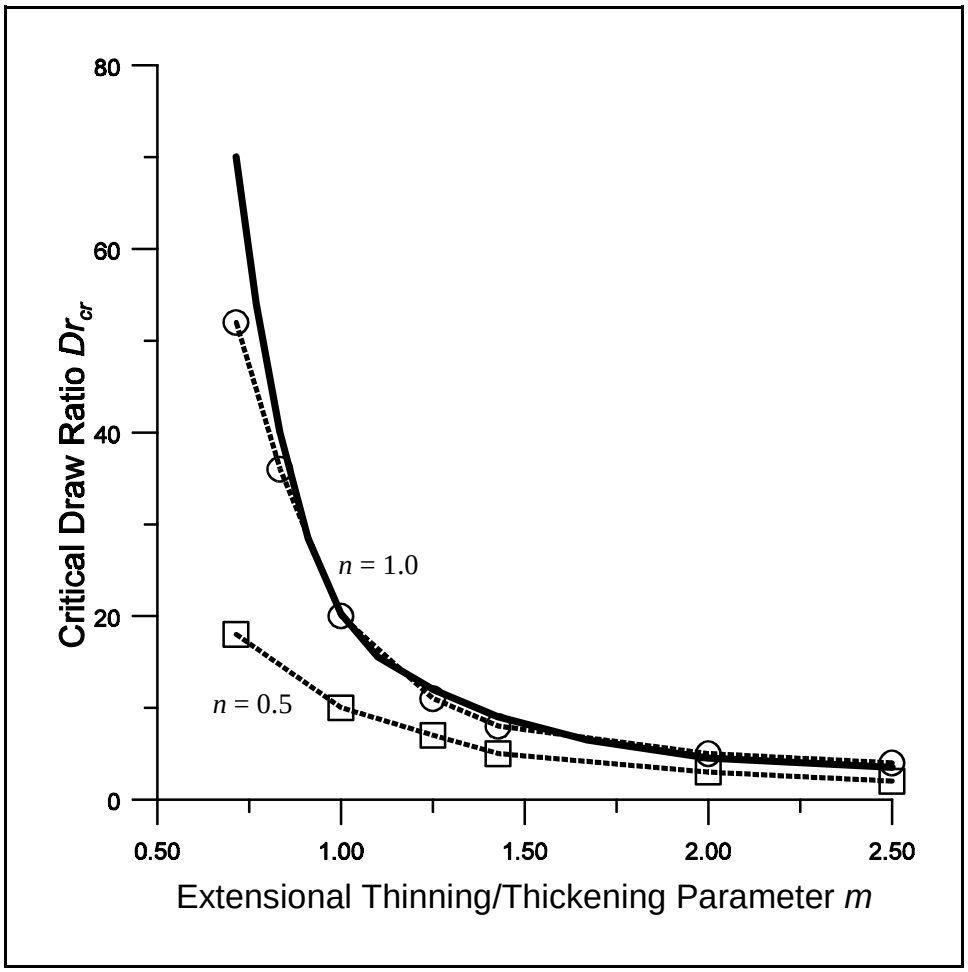


**Figure 5.7** Dependence of $Dr_{cr}$ on the extensional thinning/thickening parameter, with and without strain-hardening for the closed-form (—) and numerical solutions (○ and □)

### 5.2.3 Influence of Relaxation Time on Stability

The critical draw ratio for higher relaxation times is identified using the procedure described in Section 5.2.1. It should be noted that a different time step size than that shown in Table 5.1 was found to change the critical draw ratios for the simulations of this section,

although the change was small and the qualitative trends were unchanged. Figure 5.8 plots the highest stable draw ratio for the different relaxation times. This figure shows that a higher relaxation time decreases the stability of the system. The decrease in $Dr_{cr}$ could be related to the increase in the elastic strain energy, which is available to do work when it is released. The trend shown in Figure 5.8 differs from that predicted by linear stability analysis of viscoelastic fluids, which suggests that increasing relaxation time has a stabilizing effect (Anturkar and Co 1988; Silagy *et al*. 1996). However, as previously mentioned, the constitutive equation used in this study fundamentally differs from those used in previous stability studies.

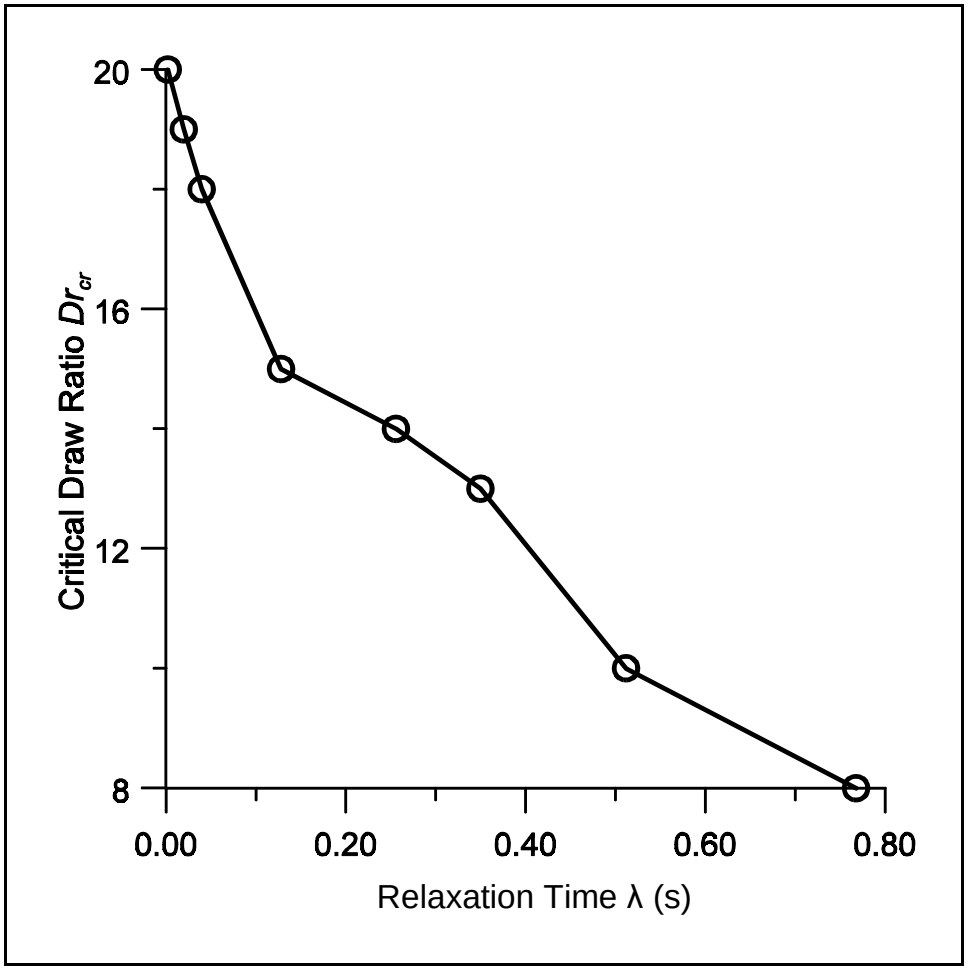


**Figure 5.8** Dependence of the critical draw ratio $Dr_{cr}$ on the relaxation time λ (s)

### 5.2.4 Influence of Nonisothermal Conditions on Stability

To investigate the influence on a viscous fluid of increasing heat transfer from the film's surface, the parameters of Tables 5.1 and 5.2 were used for a range of draw ratios, until instability was observed. The results of the analysis are summarized in Figure 5.9. As the figure shows, increasing heat transfer has a significant benefit for the stability of the film. The same stabilizing influence is observed in fibre spinning (Shah and Pearson 1972), which

has essentially the same governing equations as 1D film casting. An increase in the critical draw ratio with increasing heat transfer from the film's surface provides an explanation with regard to why industrial film lines operate at much higher draw ratios than should be possible according to the isothermal theory.

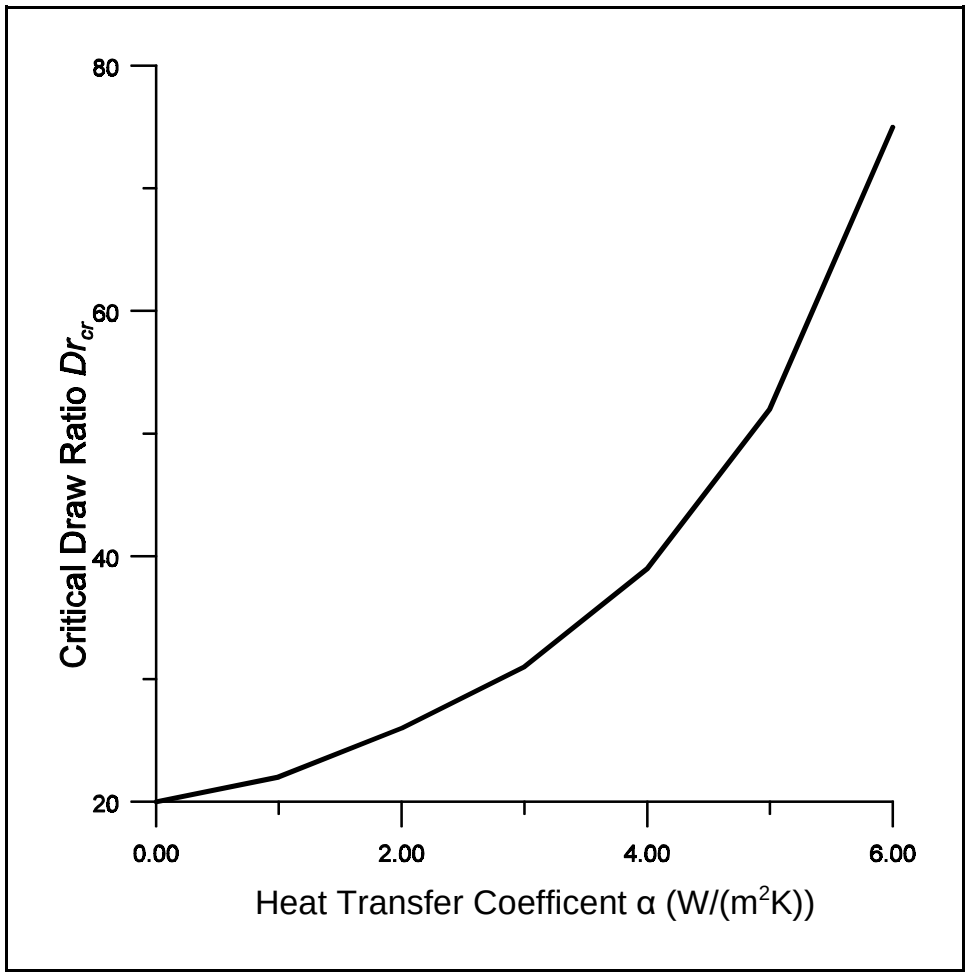


**Figure 5.9** Dependence of the critical draw ratio $Dr_{cr}$ on the heat transfer coefficient α

# Chapter 6 One and a Half Dimensional Simulations

The previous chapter considered film that was either infinite in width or constrained in the transverse direction. Although this assumption provides useful information, it is not realistic because real films tend to neck-in. This chapter presents what is termed a 1.5D model, which allows for neck-in, while still maintaining the simplifying assumption of uniform thickness across the width. One reason for considering the 1.5D model, besides the fact that it provides a convenient framework for investigating neck-in, is that a somewhat modified form of the model is popular in the literature on film casting (see Tables 1.2 and 1.3.) Furthermore, the 1.5D assumption has the advantage of allowing for die and roll elements that can be redefined to coincide with the spatial boundaries, as discussed in Section 3.8. Although there are advantages to the 1.5D formulation, there are also some drawbacks, which are also discussed in this chapter. Given the shortcomings of the 1.5D assumption, only a limited number of simulation results are presented here. Those results that are presented focus on an approximately viscous fluid and the influence of the aspect ratio *Ar*, which is defined as the ratio of the air-gap length to the die width; that is, $Ar = L/W_{die}$.

Section 6.1 considers two sets of steady-state simulations: one that compares the current work to an available closed-form solution; and the other that investigates the

influence of the aspect ratio on the film's steady-state geometry. The influence of the aspect ratio is also considered in Section 6.2, but this time with respect to its influence on the critical draw ratio. The final section, Section 6.3, discusses the problems and drawbacks associated with the 1.5D kinematic assumption.

## 6.1 Steady-State Simulations

The approach for detecting the steady-state conditions is the same as that used for the 1D simulations, except that now the width at the chill roll, as well as the thickness and the rate of energy dissipation, are monitored until the oscillations cease. All of the simulations in this section were continued until their steady-state was reached. The transient results are discussed in Section 6.2.

### 6.1.1 Comparison with a Closed-Form Solution

Sergent (1977) developed a mathematical solution for the film casting problem using the same kinematic assumptions as the 1.5D numerical algorithm developed for this study, although the two approaches are not identical in terms of the boundary conditions. Whereas Sergent (1977) sets the die width as a prescribed boundary condition, the current approach does not prescribe the width. However, the same objective is accomplished in the numerical algorithm by setting the transverse velocity at the die to zero. The solution developed by Sergent (1977) is summarized in Appendix L.

Avenas *et al*. (1986) present the answers for several film casting problems using the closed-form solution of Sergent (1977). The description of one of these problems is summarized in Table 6.1, along with the numerical parameters used to perform the simulation of this study. The parameters *nelL* and *nelW* stand for the number of divisions in the finite element mesh in the machine and transverse directions, respectively.

**Table 6.1 Film Casting Parameters for Comparison to the Closed-Form Solution**

| Geometry | Boundary Conditions | Material Parameters | Numerical Parameters |
|---|---|---|---|
| $L = W_{die} \cdot Ar$ | $\dot{u}_{die} = 0.01$ m/s | $m = 1.0$ | $nelL = 150$ |
| $h_{die} = 0.00055$ m | $\dot{u}_{roll} = \dot{u}_{die} Dr$ | $n = 1.0$ | $nelW = 30$ |
| $W_{die} = 0.1$ m | $Dr = 9$ | $\lambda = 0.002$ s | $\Delta t = 10^{-3}$ s |
| $Ar = 4.3$ | | $A = 1.1111 \times 10^{-5}$ (Pa·s)$^{-1}$ | $toler = 10^{-2}$ |
| | | $E = 1/(\lambda A) = 4.5 \times 10^{7}$ Pa | |

Figure 6.1 compares the film's free surface for the closed-form versus the numerical solution, using the simulation parameters of Table 6.1. Good agreement is shown between the two solutions, especially considering the scale of the *y*-axis used in the figure. However, there is a significant difference in terms of the behaviour at the die and roll, where the numerical solution shows curvature, and the closed-form solution maintains a linear trend. This variation is due to the difference in boundary conditions between the two approaches and the requirement of zero mass flux across the film's free surface. In order for the zero mass flux condition to hold, the velocity vector at the edge of the film and the free surface

must be tangent to one another. At the die and roll $\dot{v} = 0$; thus, the free surface can only be tangent to the velocity if it lies in the same direction as $\dot{u}$. The boundary conditions used by the numerical algorithm are apparently in better agreement with actual film casting process, as a curved shape is in better qualitative agreement with experimental evidence (d'Halewyu *et al.* 1990; Barq *et al.* 1992.)

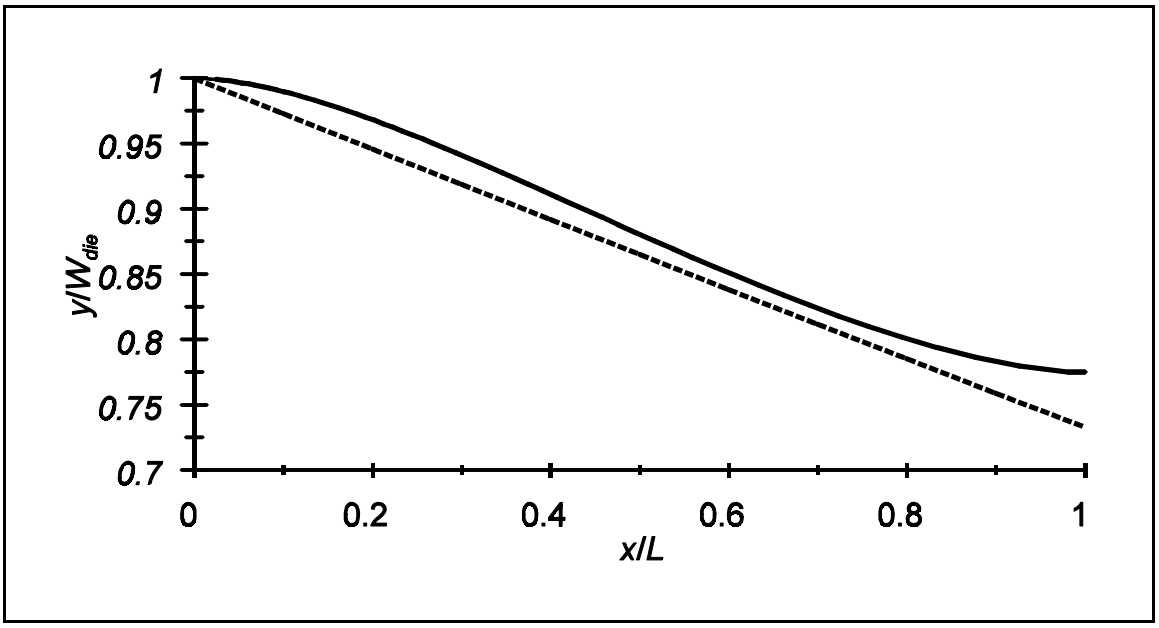


**Figure 6.1** Free surface for the closed-form solution (---) and for the numerical solution (–)

The simulated film thickness was also compared to the closed-form solution. A maximum relative difference of -5% was found between the closed-form and numerical solutions. The relative difference is negative because of the continuity requirement and because, as Figure 6.1 shows, the numerical solution has a greater width than the closed-form

solution. In order to have the same mass flux in both cases, the thickness must decrease to compensate.

The previous results are for a draw ratio of 9; Avenas *et al.* (1986) also show results for different draw ratios. Figure 6.2 shows how the force *F*, width and thickness of the numerical and closed-form solutions vary with the draw ratio. For the numerical solution, the force was calculated by numerically integrating the following equation:

$$F = 2\int_{0}^{W_{roll}} h\sigma_{xx}dy \qquad \textbf{(6.1)}$$

where $W_{roll}$ is the film's half width at the roll. Figure 6.2 shows that the two solutions are in good agreement with respect to their force predictions. The numerically predicted thickness and width also follow the same trend as the closed-form solution, with the error decreasing as the draw ratio increases. As mentioned previously, the numerically simulated width is greater than the closed-form solution; therefore, in order to satisfy continuity the simulated thickness must be less than the closed-form thickness, as demonstrated in Figure 6.2.

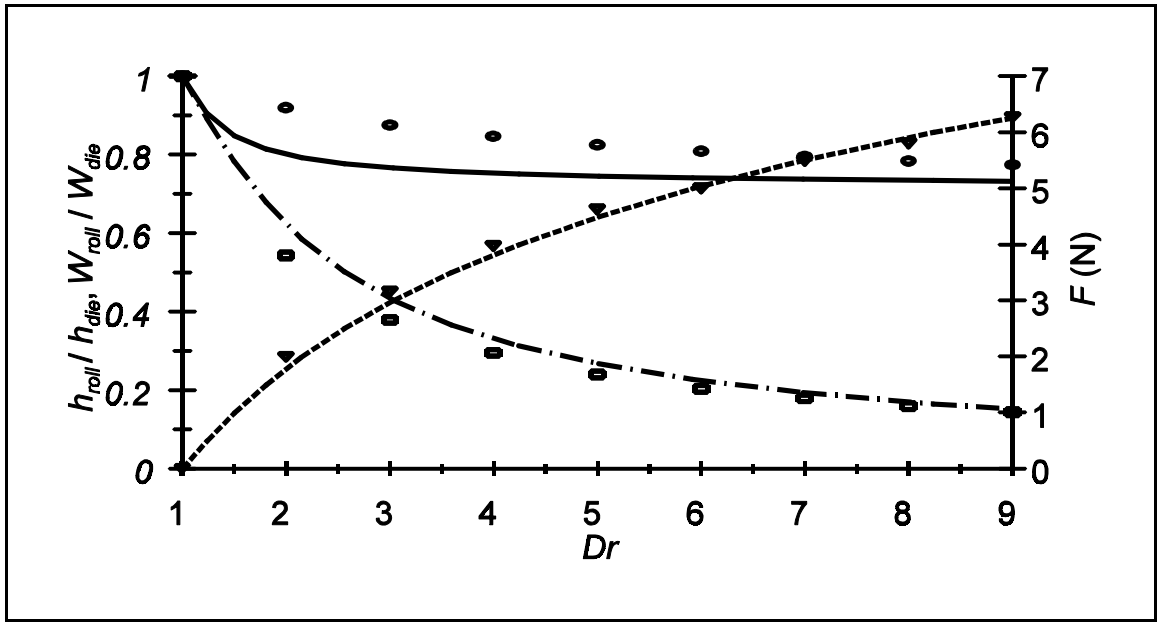


**Figure 6.2** Force (▽), width (○) and thickness (□) versus draw ratio for the numerical solutions and the corresponding closed-form solutions (---, —, and ·–·–, respectively)

### 6.1.2 Influence of the Aspect Ratio

The parameters provided in Table 6.2 were used to conduct the simulations presented in this section, but with different values of the aspect ratio $Ar = L/W_{die}$. An approximately viscous fluid is used to avoid the complications of extensional thinning/thickening, strain-hardening or effects of material elasticity.

**Table 6.2 Film Casting Parameters for the 1.5D Simulations**

| Geometry | Boundary Conditions | Material Parameters | Numerical Parameters |
|---|---|---|---|
| $L = W_{die} \cdot Ar$ | $\dot{u}_{die} = 0.01$ m/s | $m = 1.0$ | $nelL = 150$ |
| $h_{die} = 0.001$ m | $\dot{u}_{roll} = \dot{u}_{die} Dr$ | $n = 1.0$ | $nelW = 30$ |
| $W_{die} = 0.5$ m | $Dr = 10$ | $\lambda = 0.002$ s | $\Delta t = 10^{-3}$ s |
| $Ar = 0.2$ | | $A = 1.6667 \times 10^{-4}$ (Pa·s)$^{-1}$ | $toler = 10^{-2}$ |
| | | $E = 1/(\lambda A) = 3.0 \times 10^{6}$ Pa | |

Figure 6.3 shows the thickness contours for various values of the aspect ratio *Ar*, with $Ar = 0.0$ corresponding to $W_{die} \rightarrow \infty$ and thus to 1D conditions. All of the contours are parallel because the 1.5D assumption does not allow the thickness to vary in the transverse direction. This means that each cross-section of the film must be rectangular. Figure 6.3 shows that as the aspect ratio increases the neck-in also increases. This result is to be expected, as a longer air-gap provides a greater opportunity for the film to neck-in. A consequence of the increased neck-in is that the thickness of the film at the roll increases as the aspect ratio increases, owing to continuity. For the same mass flux to cross onto the roll with a decreased width, there must be a corresponding increase in the thickness.

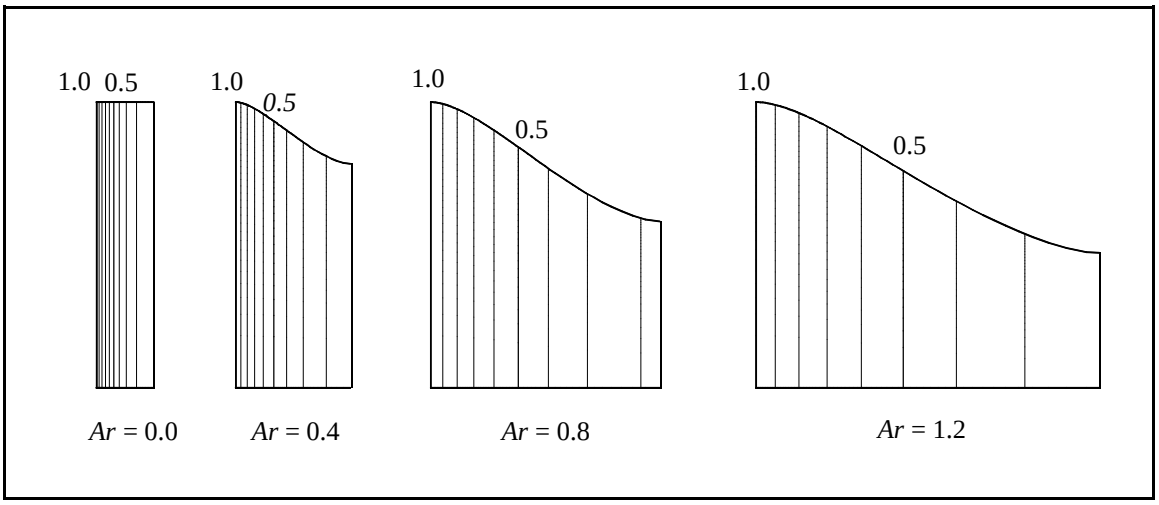


**Figure 6.3** Normalized thickness contours ($h/h_{die}$) for varying aspect ratios (*Ar*)

### 6.2 Influence of the Aspect Ratio on the Critical Draw Ratio

The approach to identifying instability for the 1.5D problems is the same as that used for the 1D simulations discussed in the previous chapter. The findings are summarized in Figure 6.4, which shows how the critical draw ratio varies with the aspect ratio. One of the points (*Ar* = 0.4) in the figure deviates from the trend exhibited by the other points. The deviation is likely a consequence of the lack of precision associated with limiting the analysis to only integer values. To illustrate this point, the figure includes a dashed line for the trend that would occur if the critical draw ratio for the point in question were increased by one integer value. The first point in Figure 6.4 corresponds to the critical draw ratio for 1D film casting. As the aspect ratio increases, a stabilizing influence is observed, although the benefits seem to level off at $Ar \approx 1.0$. A stabilizing influence from an increasing aspect ratio is also shown in the studies of Silagy *et al*. (1996a, 1996b) and Chambon *et al*. (1996).

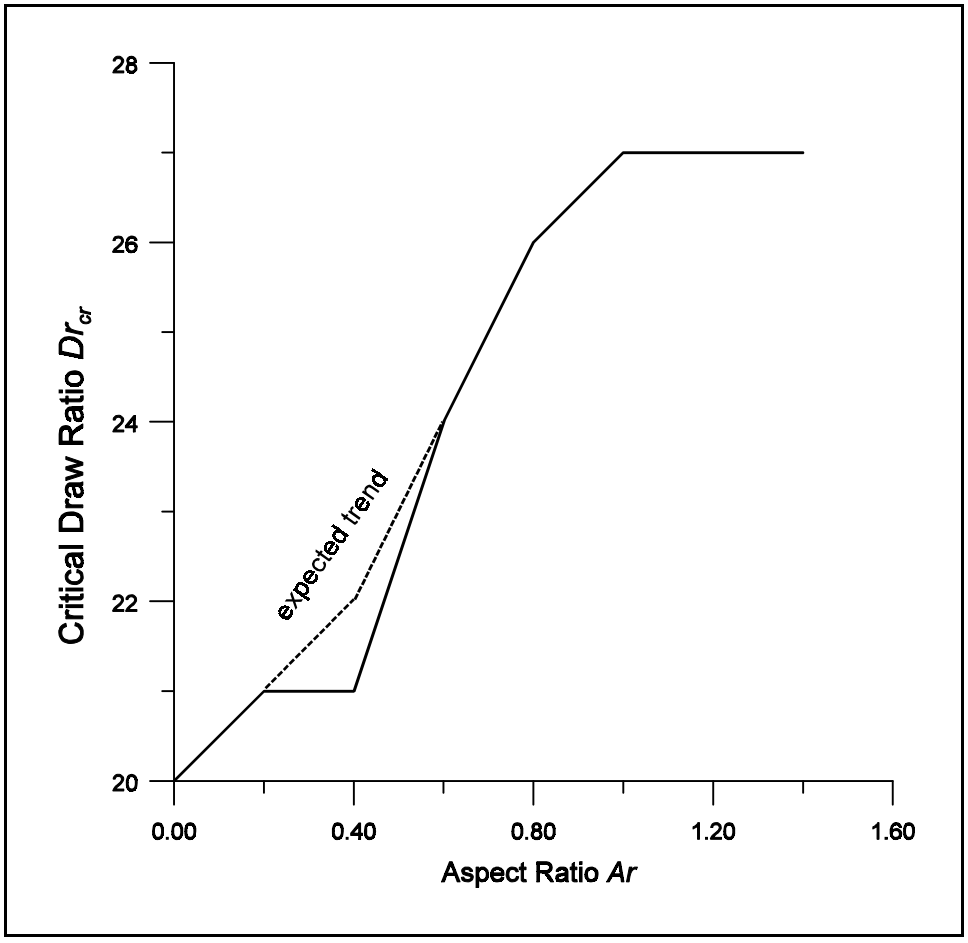


**Figure 6.4** Critical draw ratio $Dr_{cr}$ versus the aspect ratio *Ar*

## 6.3 Problems with the 1.5D Kinematic Assumption

As discussed in Section 6.1, the formulation used by Sergent (1977) and others predicts a linear shape for the free-surface, which is unlike the curved shape observed in practice. Although the numerical algorithm used in this thesis does not have this shortcoming, there is another problem, which both the closed-form and 1.5D numerical algorithm share. In the real film casting process, edge beads are observed and edge beads

cannot be accommodated within the 1.5D assumption. Not being able to predict edge-bead may not seem like a major problem, as the edge-bead only represents a small fraction of the overall width and it is typically trimmed from the film, however the edge-bead has a strong influence on the overall film geometry. The edge-bead provides a restraining influence on the film, with the result that the middle of the film is essentially in a state of plane strain. When a state of plane strain is combined with the membrane approximation, the 1D model discussed in the previous chapter is obtained. Therefore, the 1D model seems more consistent with the behaviour across the majority of film's width, than does the 1.5D model.

The idea that the middle of the film is in a state of plane strain, and that the edge is in a state of uniaxial extension, was first proposed by Dobroth and Erwin (1986). This theory is supported by the results of others, including Smith and Stolle (2000a), where the restraining influence of the edge-bead is illustrated for nonisothermal film casting, film falling under its own weight, and for the case when the edge-bead is partially removed by employing a nonuniform thickness across the die. However, the assumption of 1D behaviour in the middle of the film does not seem to hold for larger aspect ratios. For instance, the simulation results of Debbaut *et al.* (1995) at $Ar = 1.0$ do not show a zone of 1D behaviour. Therefore, when higher aspect ratios are used, or when there is interest in the behaviour of the edge-bead, it is necessary to adopt a fully 2D formulation. The next chapter presents steady-state and stability results for a 2D formulation.

# Chapter 7 Two-Dimensional Simulations

Although useful information can be gained from 1D and 1.5D simulations, the film casting process is more accurately approximated as 2D. A 2D formulation is necessary to accommodate the presence and influence of an edge-bead. Furthermore, experimental measurements show that velocity in the machine direction ($\dot{u}$) is a function of both in-plane coordinate directions (Chambon *et al.* 1996). The necessity of a 2D formulation becomes more apparent as the aspect ratio increases, because the size of the region of approximately 1D behaviour decreases as the aspect ratio increases.

Unfortunately the more realistic 2D description does not come without a price; the 2D formulation has challenges that are not encountered in either the 1D or 1.5D formulations. Two complications for the 2D formulation are:

i) the elements can now rotate, which can introduce error; and,

ii) the nodal coordinates cannot be redefined at the roll so as to agree with the spatial boundary conditions.

A consequence of these complications is that the stiffness matrix may become ill-conditioned at higher draw ratios because of the mesh distortion through element stretching and rotation. Another complication for the 2D description is that more elements are required than for the 1D and 1.5D algorithms because the 2D formulation has to accommodate additional gradients in the transverse direction. The need for more elements means an increase in the

computer time required to execute the simulations. To avoid the impact of mesh distortions and long simulation times, the simulations of this chapter are conducted at relatively low draw ratios. As the instability of the film is apparent at higher draw ratios, the approach used for the 1D and 1.5D analyses to determine the critical draw ratio is not used for the 2D analyses; that is, instability is not determined by finding the operating conditions that cause undamped oscillations in the film geometry and in the rate of energy dissipated. This does not mean however that instability cannot be considered for the 2D simulations, since a comparison of the transient behaviour of different simulations at the same draw ratio provide insight into how different materials and operating conditions influence stability. Besides providing information on stability, the transient response at low draw ratios is also valuable because it provides a picture of how the film's width and thickness interact.

Steady-state results are presented in Section 7.1 to illustrate the influence of the constitutive parameters ($m$, $n$ and $\lambda$) and nonisothermal conditions on the film's thickness and velocity profiles. Following this, Section 7.2 compares the results for the current formulation against previously published viscous fluid film casting simulations. The final section, Section 7.3, focusses on the time-dependent behaviour of the 2D film.

## 7.1 Steady-State Parametric Study

All of the simulations that were conducted for the parametric study were based on the parameters from Table 7.1, and they were continued until $\dot{W}^c$ converged to an approximately constant steady-state value. As shown in Table 7.1, an aspect ratio of $Ar = L/W_{die} = 1.4$ was

chosen. Although most film lines operate at lower aspect ratios, this value was chosen for two reasons. Firstly, the 2D nature of the film is more apparent at higher aspect ratios and secondly, the higher aspect ratio simulations amplify the influence of changes in the constitutive parameters or operating conditions, because the larger air-gap allows more time for an adjustment in the flow characteristics. The second reason for using a large aspect ratio is important because, as the simulations of this section show, in many respects the film is relatively insensitive to changes in the material properties or operating conditions.

**Table 7.1 Film Casting Parameters for the 2D Simulations**

| Geometry | Boundary Conditions | Material Parameters | Numerical Params |
|---|---|---|---|
| $h_{die}$ = 0.001 m | $\dot{u}_{die}$ = 0.01 m/s | $m$ = 1.0 | $nelL$ = 200 |
| $W_{die}$ = 0.5 m | $\dot{u}_{roll} = \dot{u}_{die} Dr$ | $n$ = 1.0 | $nelW$ = 40 |
| $Ar$ = 1.4 | $Dr$ = 10 | $\lambda$ = 0.002 s | $\Delta t = 10^{-3}$ s |
| $L=W_{die}\cdot Ar$ =0.7 m | | $\eta^s$ = 2000 Pa·s | $toler = 10^{-2}$ |
| | | $A = 1/(3\eta^s) = 1.6667\times10^{-4}$ (Pa·s)$^{-1}$ | |
| | | $E = 1/(\lambda A) = 3.0\times10^{6}$ Pa | |

All of the simulations of this section have steady-state finite element meshes similar to that shown in Figure 7.1, which corresponds to the simulations parameters of Table 7.1. Although the mesh is a "snap-shot" at one instant of time, the distortion of the elements provides a clear picture of the deformation history for the material, as one can easily identify the distortions that develop as the material is stretched through the air-gap. Figure 7.1

illustrates that the material experiences large accumulated strains. Along the centre line of the film the accumulated strain is mostly extensional, whereas nearer the edge, the material experiences significant shear strain. The shape of the finite element mesh also highlights the fact that the elements near the edge have a longer path and residence time within the air-gap. An examination of Figure 7.1 reinforces the practise of using low aspect ratios for film lines because the high aspect ratio allows the undesirable result of the high neck-in shown in the figure. Moreover, the pronounced differences between the shapes of the finite elements at the chill roll suggests that the desired uniformity of the film properties across the film's width will not be achieved, because the deformation histories of the different material particles are so dissimilar. From a practical point of view, the shape of the mesh and its elements provides useful information on the behaviour of the film.

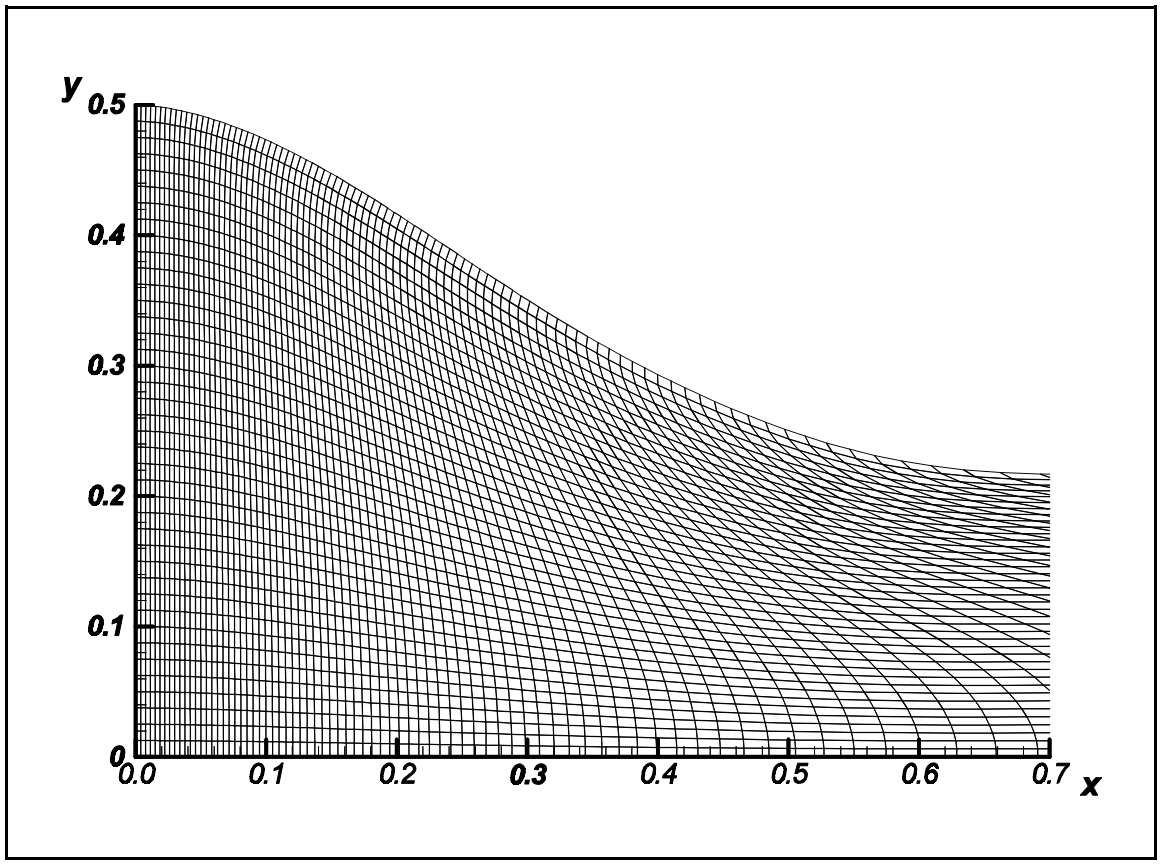


**Figure 7.1** Finite element mesh for the film casting of a Newtonian fluid

### 7.1.1 Influence of Extensional Thinning/Thickening

To investigate the influence of extensional thickening/thinning, the parameters of Table 7.1 were used, with *m* values of 1.0 (Newtonian fluid), 0.75 (thickening fluid) and 1.5 (thinning fluid). Figure 7.2 illustrates how the normalized thickness contours are effected by the power-law nature of the viscosity. The extensional thickening fluid shows a higher thickness gradient at the die, in the machine direction. This behaviour was also observed for the 1D simulations presented in Section 5.1.1. Just as the thickness at the die changes more

rapidly for the extensional thickening fluid, the free surface necks-in more rapidly for the extensional thickening fluid. However, the final width of the film is almost identical for all three fluids under consideration. In fact, the differences in geometry between the different fluids is fairly small. This finding is in keeping with the results presented by Debbaut *et al*. (1995), who show steady-state simulation results for the 2D film casting of an extensional thinning fluid. For small degrees of extensional thinning ($m$ = 1.25), Debbaut *et al*. show only a small change from the thickness predictions for a Newtonian fluid. However, for larger degrees of extensional thinning ($m$ = 2 and $m$ = 3), they show a dramatic change in the thickness distribution. These high values of $m$ could not be reproduced with the UL algorithm because the stiffness matrix became ill-conditioned, likely because of the increased physical instability for higher values of $m$. As demonstrated in Section 5.2.2 for the 1D formulation, higher $m$ values lead to a dramatic decrease in the critical draw ratio. The algorithm presented by Debbaut *et al*. does not account for instability, so the possibility exists that the high extensional thinning value simulations they present actually represent "impossible" results. The influence of extensional thinning on the stability of 2D film casting is discussed further in Section 7.3.

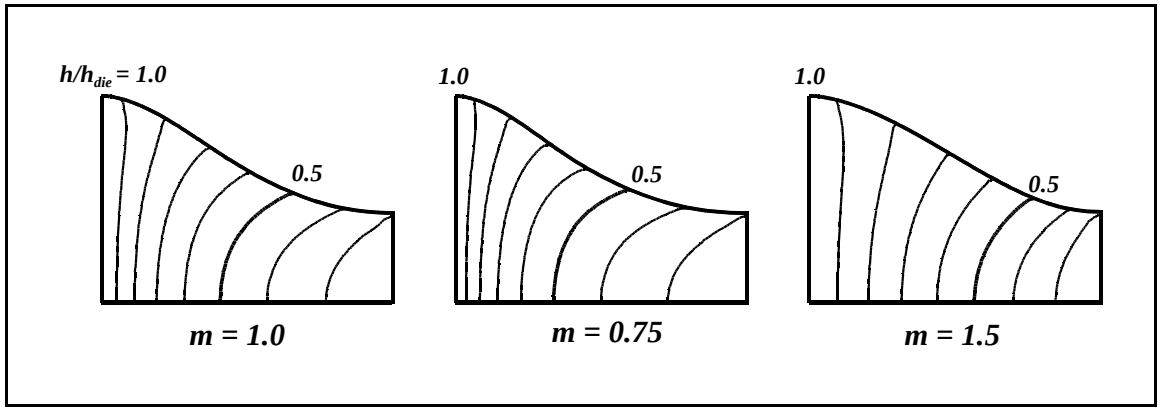


**Figure 7.2** Thickness contours for various values of the extensional thinning/thickening parameter *m*

### 7.1.2 Influence of Strain-hardening

The influence of the *n* parameter is demonstrated by three simulations, for which the normalized thickness contours are shown in Figure 7.3, using the parameters of Table 7.1, with $n$ = 1.0, 0.5 and 0.25. As for the 1D simulations discussed in Section 5.1.2, strain-hardening leads to a higher thickness gradient at the die. In fact, the initial decrease in thickness is so rapid for $n$ = 0.25 that the $h/h_{die}$ = 0.9 contour is close enough to the die that the first two contours in Figure 7.3 are almost coincident. The jump in thickness reduction at the die may be partly due to the imprecise satisfaction of the boundary conditions at the die. However, the high gradients at the die also point to a potential problem area in the physical process that an engineer should be aware of. Strain-hardening also has an influence on the shape of the free surface. For every film casting simulation the free surface must be normal to the die and to the roll to ensure that the free surface is tangent to the velocity

vector. At these locations the boundary conditions specify that the only non-zero velocity component is in the machine direction; however, as the film moves away from the die the free surface adjusts so that it is no longer perpendicular to the die. In the case of a strain-hardening fluid this adjustment in the free surface occurs more rapidly than for a Newtonian fluid. Another influence of strain-hardening is a wider final film width. A likely explanation for this is the longer particle path along the free surface. The longer path provides more time for the creep strain to accumulate and this results in a stiffer material. The stiffer material at the edges provides a restraining influence, which leads to a slightly larger final film width. As a final point, the 0.5 contour for all three materials is in approximately the same location, so the change in the constitutive behaviour has not had an overly dramatic influence on the overall film geometry.

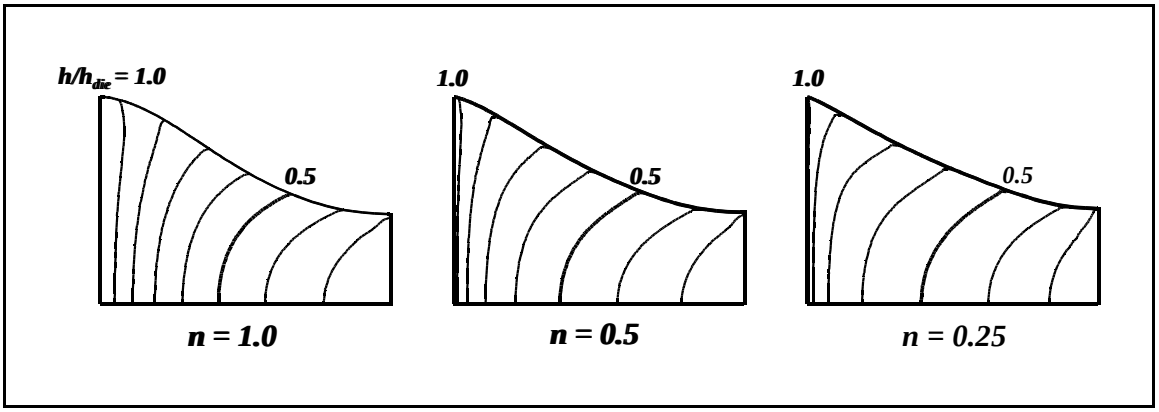


**Figure 7.3** Thickness contours for various values of the strain-hardening parameter *n*

### 7.1.3 Influence of Relaxation Time

Once again using the parameters of Table 7.1, simulations were completed with relaxation times of 0.002, 2 and 7s. Figure 7.4 illustrates the influence of the relaxation time on the normalized thickness contours. Although the influence is not dramatic, the higher relaxation times lead to a more sharply defined edge-bead and a larger final film width. A similar result is observed by Debbaut *et al*. (1995) with increasing relaxation time, but Debbaut *et al*. show much more significant changes. Furthermore, Debbaut *et al*. show a higher thickness gradient at the die with increasing relaxation time. The differences between the current study and Debbaut *et al*. are not surprising though, given that their Maxwell equation is not equivalent to the Maxwell equation used by the current formulation, for the reasons discussed in Chapter 4.

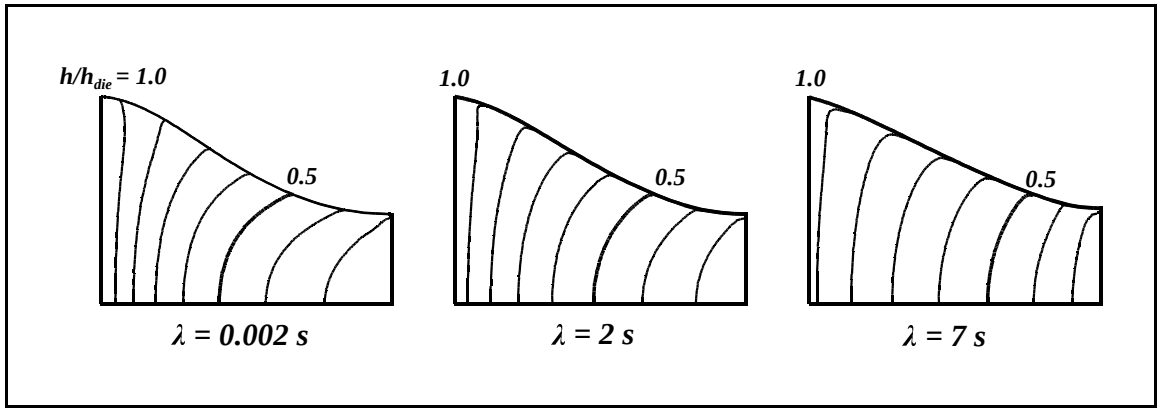


**Figure 7.4** Thickness contours for various values of the relaxation time λ (s)

### 7.1.4 Influence of Nonisothermal Conditions

The normalized thickness contours shown in Figure 7.5 were found by using the parameters of Tables 7.1 and 5.2, with a heat transfer coefficient α of 0, 20 and 40 W/(m$^2$·K). For the material properties and processing conditions chosen, the nonisothermal conditions are seen to increase the thickness gradient at the die, as was also observed for the 1D simulations in Section 5.1.4 and for the 2D simulations of Smith and Stolle (2000a). Another observation from Smith and Stolle (2000a) that is reproduced by the simulations under consideration is a decrease in the neck-in with increasing heat transfer. Smith and Stolle suggest that the decrease in neck-in is a consequence of the longer particle path at the edge of the film, as this leads to increased cooling and a greater restraining influence of the edge, because of the increase in the temperature-dependent viscosity.

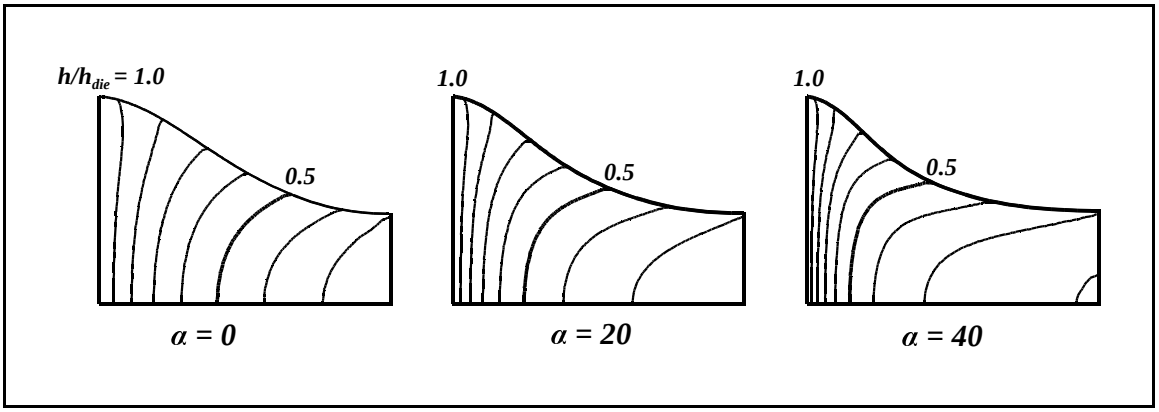


**Figure 7.5** Thickness contours for various values of the heat transfer coefficient α (W/(m$^2$·K))

## 7.2 Comparison to Other Steady-State, Viscous Fluid Studies

Although the viscoelastic constitutive equation for the UL formulation cannot be compared to viscoelastic film casting E studies, the approximately viscous UL formulation has a similar constitutive response as that used in the E formulations for the film casting of a viscous fluid. In this section, the steady-state simulation results using the current algorithm are compared to the simulation results for the steady-state viscous film casting studies presented by d'Halewyu *et al*. (1990), Sakaki *et al*. (1996), Smith and Stolle (2000a) and Debbaut *et al*. (1995).

### 7.2.1 Comparison to d'Halewyu *et al.* (1990)

To reproduce the simulation presented by d'Halewyu *et al*. (1990), the parameters of Table 7.1 were used, but with the aspect ratio modified to $Ar = 0.4$. Figure 7.6 shows the thickness profile at the chill roll as predicted by several authors for this same film casting problem. The simulations of Sakaki *et al*. (1996) and Smith and Stolle (2000a) are seen to agree quite well, but the results of d'Halewyu *et al*. (1990) and the current study provide two different answers. In the centre of the film, where the film behaviour is essentially 1D, all of the simulations agree, but nearer the edge the results differ. With the exception of the current study, all of the papers cited in Figure 7.6 use an Eulerian algorithm. Smith and Stolle (2000a) compare the results of the three Eulerian simulations shown in the figure and suggest that the results of d'Halewyu *et al*. differ because of their use of an uncoupled numerical algorithm. It appears that the nonlinear nature of the film problem leads to

numerical solutions that are not necessarily unique. The UL algorithm is significantly different from the E approaches and this might explain the observed differences. This issue is looked at more closely in the next chapter.

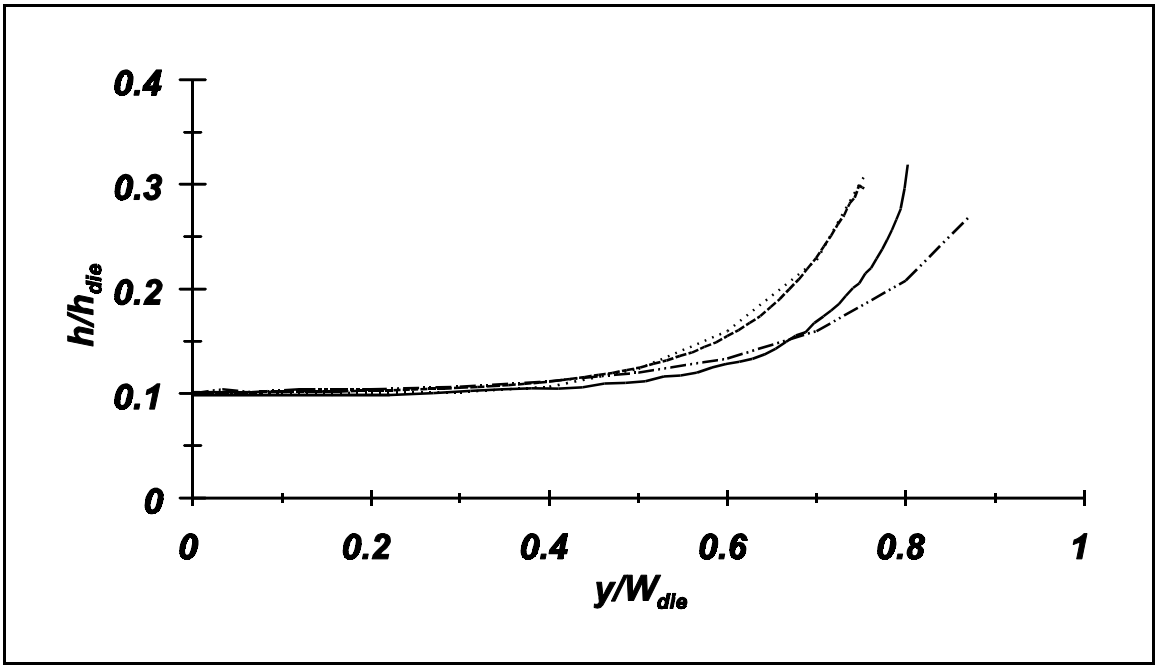


**Figure 7.6** Thickness profile at the chill roll for d'Halewyu *et al.* (1990) (–··–), Sakaki *et al.* (1996) (···), Smith and Stolle (2000a) (---), and the current study (—)

### 7.2.2 Comparison to Debbaut *et al.* (1995)

Another 2D study of viscous film casting is presented by Debbaut *et al*. (1995). To simulate the film casting problems discussed by them, the simulation parameters of Table 7.1 were modified to $Ar = 1.0$ and $Dr = 9$ or $Dr = 20$. The thickness profile at the chill roll is shown in Figure 7.7, as predicted by Debbaut *et al*. (1995), the E algorithm of Smith

(1997) and by the current UL formulation. As in the previous section, the different algorithms lead to different predictions. The differences are even more pronounced here, since these simulation use a higher aspect ratio, $Ar = 1.0$ versus the previous value $Ar = 0.4$. The higher value of $Ar$ allows the flow to readjust so that there is no zone of approximately 1D behaviour at the centre of the film. The most pronounced difference in Figure 7.7 is for the UL simulation versus the two E algorithms at a draw ratio of 20. The differences in this case may be due to the differences in the numerical algorithms, or possibly the differences in how the downstream boundary condition is implemented. These possibilities are investigated in the next chapter.

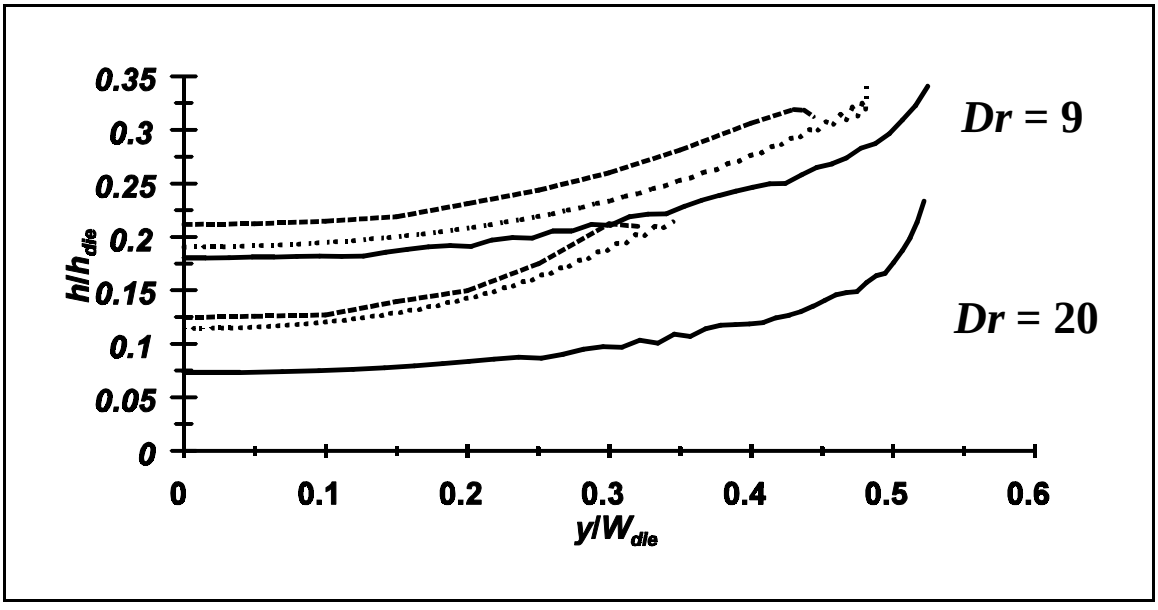


**Figure 7.7** Thickness profile at the chill roll for Debbaut *et al.* (1995) (– – –), using the E algorithm of Smith (1997) (···), and the current study (–)

### 7.3 Transient Behaviour in 2D Film Casting

In the 2D simulations, the thickness distribution and the width of the film interact. This interaction is shown in Figure 7.8, for the width at the chill roll and for the thickness at the line of symmetry. The simulation parameters are the same as those in Table 7.1, but with $Ar = 0.2$ and $Dr = 15$. As this figure shows, the oscillations in the thickness and width are out of phase with one another. This is to be expected owing to the continuity requirement. When the thickness increases, the width has to decrease to compensate and vice-versa. Silagy *et al*. (1998, 1999) show this same phase difference in their simulation results for the 2D film casting of a viscous fluid.

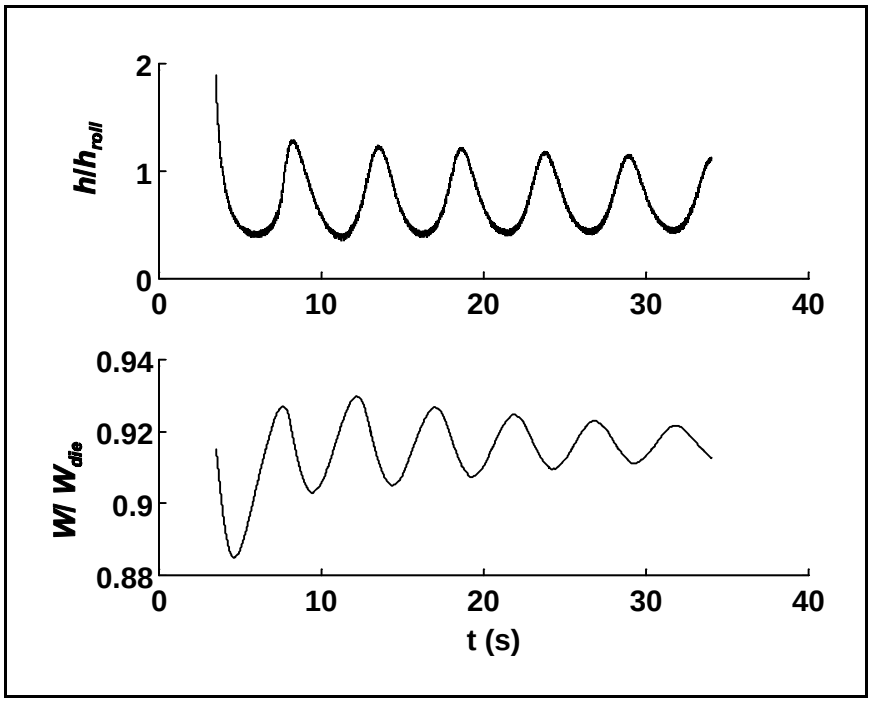


**Figure 7.8** Normalized width and thickness histories at the chill roll for film casting of a Newtonian fluid with $Ar = 0.2$ and $Dr = 15$

As mentioned in the introduction to this chapter, it is not possible to reliably investigate instability for the 2D simulations in the same way as was done for the 1D and 1.5D simulations, because of the distortion of the mesh at higher draw ratios. The approach for considering instability in 2D is to look at the number of oscillations in the indicator variables at low draw ratios. If a change in operating conditions leads to more oscillations, then this is a likely indication that the change in question has a destabilizing influence. Using this idea, the following conclusion can be reached from considering the time histories associated with the simulations of this chapter:

- the trends in instability for the 2D simulations with changing constitutive parameters and nonisothermal conditions are the same as for the 1D simulations:
  - increased extensional thinning has a destabilizing influence
  - higher relaxation times have a destabilizing influence
  - increased extensional thickening has a stabilizing influence
  - increased heat transfer has a stabilizing influence
- higher aspect ratios have a stabilizing effect, like that observed for the 1.5D simulations.

All of the time histories used to make the above conclusions are not reproduced here, but an example is provided to illustrate the approach. The example time histories, which are shown in Figure 7.9, are for the three different *m* value simulations discussed in Section 7.1.1. The number of oscillations in the $\dot{W}^c$ history, before steady-state, increases with increasing values of *m*, as shown in Figure 7.9. Furthermore, with *Ar* = 1.4, *m* = 1.5 is stable, but for the 1D simulations, where *Ar* = 0, *m* = 1.5 is not stable, as shown in Figure 5.6. Therefore, in this case, a higher aspect ratio appears to have a stabilizing influence on the 2D simulation. The same approach was followed to examine the stability of the other

constitutive parameters and for the nonisothermal conditions, in order to make the conclusions listed above.

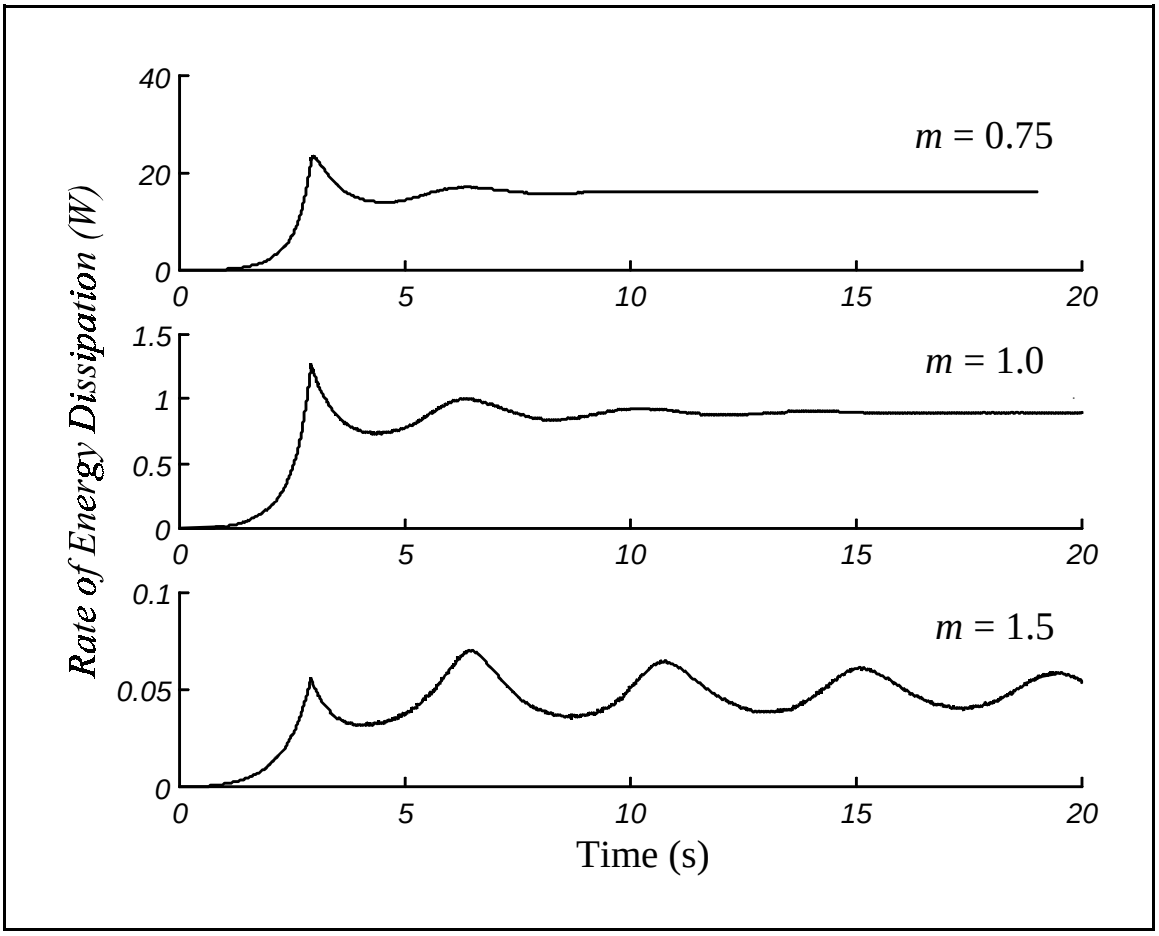


**Figure 7.9** Rate of energy dissipation history for the three different *m* value simulations discussed in Section 7.1.1

# Chapter 8 A Comparison Between the Updated Lagrangian and Eulerian Algorithms

As mentioned in Chapter 1, the UL approach is rarely, if ever, used for the simulation of continuous polymer processing operations. The purpose of this chapter is to determine if this lack of attention is deserved, or if the UL formulation has potential to compete with the E approach. To make this determination, the two formulations are compared for a specific continuous process, that of isothermal film casting of a viscous fluid. The UL algorithm for film casting has been described in the previous chapters and the E algorithm, which is developed in Smith (1997), is summarized in Section 8.1. Sections 8.2 and 8.3 compare the E and UL algorithms with respect to their accuracy for the 1D case, and the simulation results for the 2D case, respectively. A comparison of the relative complexity and efficiency of the two algorithms is the subject of Section 8.4. The section that follows discusses the advantages of the UL approach over the E approach. Thereafter, the discussion turns to the principal disadvantage of the UL algorithm: the application of spatial boundary conditions to a material mesh.

## 8.1 An Overview of the Eulerian Algorithm

An Eulerian algorithm for film casting is developed in Smith (1997), and summarized in Smith and Stolle (2000a). In this section a simplified version of the E algorithm is

presented that is essentially equivalent to the UL algorithm previously presented, for an approximately viscous fluid under nonisothermal conditions. Both algorithms employ the following assumptions: the film can be treated as a 2D membrane; the constitutive equation is for a linear viscous fluid; and inertia, self-weight, air-drag, surface tension, die-swell and film sag are ignored. The only difference between the two formulations, besides the fact that a different description of motion is being employed, is that the E algorithm is time independent; it determines the steady-state solution directly and neglects the transient behaviour.

### 8.1.1 Governing Equations and Boundary Conditions

For the coordinate system defined in Figure 8.1 the equations for the conservation of momentum, mass and thermal energy, the constitutive equation and the equation describing the free-surface are as follows:

$$\boldsymbol{L}^T(h\boldsymbol{\sigma}) = \mathbf{0} \tag{8.1}$$

$$\nabla^T(h\dot{\boldsymbol{u}}) = 0 \tag{8.2}$$

$$\rho Ch\dot{\boldsymbol{u}}^T(\nabla T) + \alpha(T - T_{air}) - kh\nabla^T(\nabla T) = 0 \tag{8.3}$$

$$\boldsymbol{\sigma} = \eta^s \begin{bmatrix} 4 & 2 & 0 \\ 2 & 4 & 0 \\ 0 & 0 & 1 \end{bmatrix} \boldsymbol{D}^v \tag{8.4}$$

$$\frac{dW}{dx}\dot{u} - \dot{v} = 0 \qquad \textbf{(8.5)}$$

where $h$ is the half thickness of the film, $W$ is the width, $\eta^s$ is the viscosity, $\dot{\boldsymbol{u}} = [\dot{u}\ \ \dot{v}]^T$ is the velocity vector and $\boldsymbol{\sigma}$ and $\boldsymbol{D}^v$ are the tensors for plane stress and the rate of deformation, respectively. As for the UL governing equations, the tensors use the column vector notation of Zienkiewicz (1977) and the vector components are summarized in Appendix A. Equations 8.1 to 8.4 have analogous equations in the UL formulation, whereas Equation 8.5, which explicitly determines the free surface, is unique to the E formulation. In the UL formulation the free surface is determined as a natural consequence of updating the geometry.

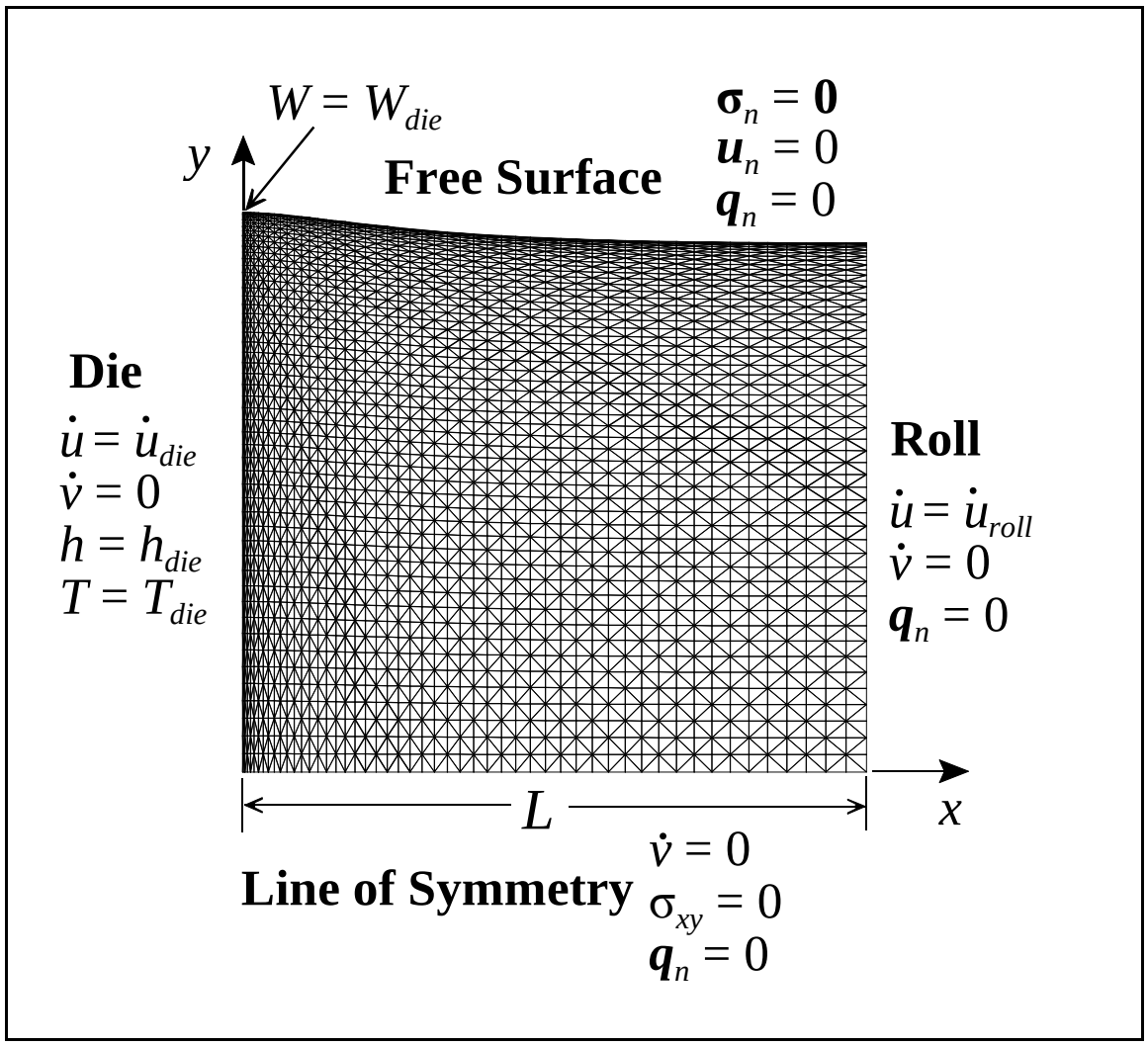


**Figure 8.1** Coordinate system, dimensions, boundary conditions and mesh for the Eulerian algorithm

As for the UL formulation, the viscosity is considered to be related to the temperature via an Arrhenius relation

$$\eta^s(T) = \eta_0^s e^{\left[\frac{Q}{R}\left(\frac{1}{T} - \frac{1}{T_0}\right)\right]} \qquad \textbf{(8.6)}$$

in which $\eta_0^s$ and $T_0$ are reference values of viscosity and temperature, $Q$ is the activation energy, and $R$ is the gas constant (8.314 J mol$^{-1}$ K$^{-1}$).

In general, the natural and kinematic boundary conditions for a thermomechanical problem are given by

$$\boldsymbol{\sigma}_n = \boldsymbol{t} \text{ on } \Gamma_t, \quad \boldsymbol{u} = \boldsymbol{u}_0 \text{ on } \Gamma_u; \quad \boldsymbol{q}_n = \boldsymbol{q}_0 \text{ on } \Gamma_q, \quad T = T_0 \text{ on } \Gamma_T \qquad \textbf{(8.7)}$$

in which $\Gamma_t$, $\Gamma_{u,}$ $\Gamma_q$, and $\Gamma_T$ are subsets of the problem boundary where the following may be specified, depending on conditions: traction $\boldsymbol{t}$, velocity $\dot{\boldsymbol{u}}_0$, thermal flux $\boldsymbol{q}_0$ and temperature $T_0$. The subscript $n$ is used to represent the fact that the values are directed outward and normal to the bounding surface. Figure 8.1 summarizes the specific boundary conditions for the film casting problem, where, as for the UL formulation, only half of the film's width is required due to symmetry. The boundary conditions are equivalent to those for the UL algorithm, except that velocities instead of displacements are considered in the E approach, and it is necessary to explicitly prescribe the width at the die.

### 8.1.2 Numerical Algorithm

Figure 8.2 shows a flowchart of the E algorithm used for solving the governing equations to predict the width, velocity, thickness and temperature for a given cast film problem. Since the equations are nonlinear, it is necessary to gradually increase the draw ratio in steps of $\Delta Dr$. Following the common finite element notation, the finite element

equivalent of Equations 8.1 to 8.5, along with the appropriate boundary conditions and temperature dependent viscosity, may be written in compact form as

$$\boldsymbol{\Psi}^i \equiv \boldsymbol{K}^i \boldsymbol{a}^i - \boldsymbol{F}^i = \boldsymbol{0} \qquad \textbf{(8.8)}$$

where $\boldsymbol{\Psi}^i$ is the residual load vector, $\boldsymbol{K}^i$ is the stiffness matrix and $\boldsymbol{F}^i$ is the load vector. Both $\boldsymbol{K}^i$ and $\boldsymbol{F}^i$ are functions of the degree of freedom vector $\boldsymbol{a}^i$, where the superscript $i$ refers to the iteration step. For the formulation summarized here, 3-noded triangular elements are used, which are arranged as shown in Figure 8.1. All the elements have degrees of freedom for the velocities, the thickness, and the temperature, and the elements at the free-edge have an additional unknown, the width. As shown in Zienkiewicz (1977: pp452-454), Equation 8.8 can be expressed in terms of a truncated Taylor's expansion, to provide the following Newton-Raphson recursion algorithm:

$$\boldsymbol{K}_T^i \Delta \boldsymbol{a}^i = -\boldsymbol{\Psi}^i \qquad \textit{with } \boldsymbol{K}_T^i = \left( \frac{d\boldsymbol{\Psi}}{d\boldsymbol{a}} \right)^i \textit{ and } \Delta \boldsymbol{a}^i = \boldsymbol{a}^{i+1} - \boldsymbol{a}^i \qquad \textbf{(8.9)}$$

The components of the tangential stiffness matrix $\boldsymbol{K}_T^i$ of Equation 8.9 are derived in Smith (1997).

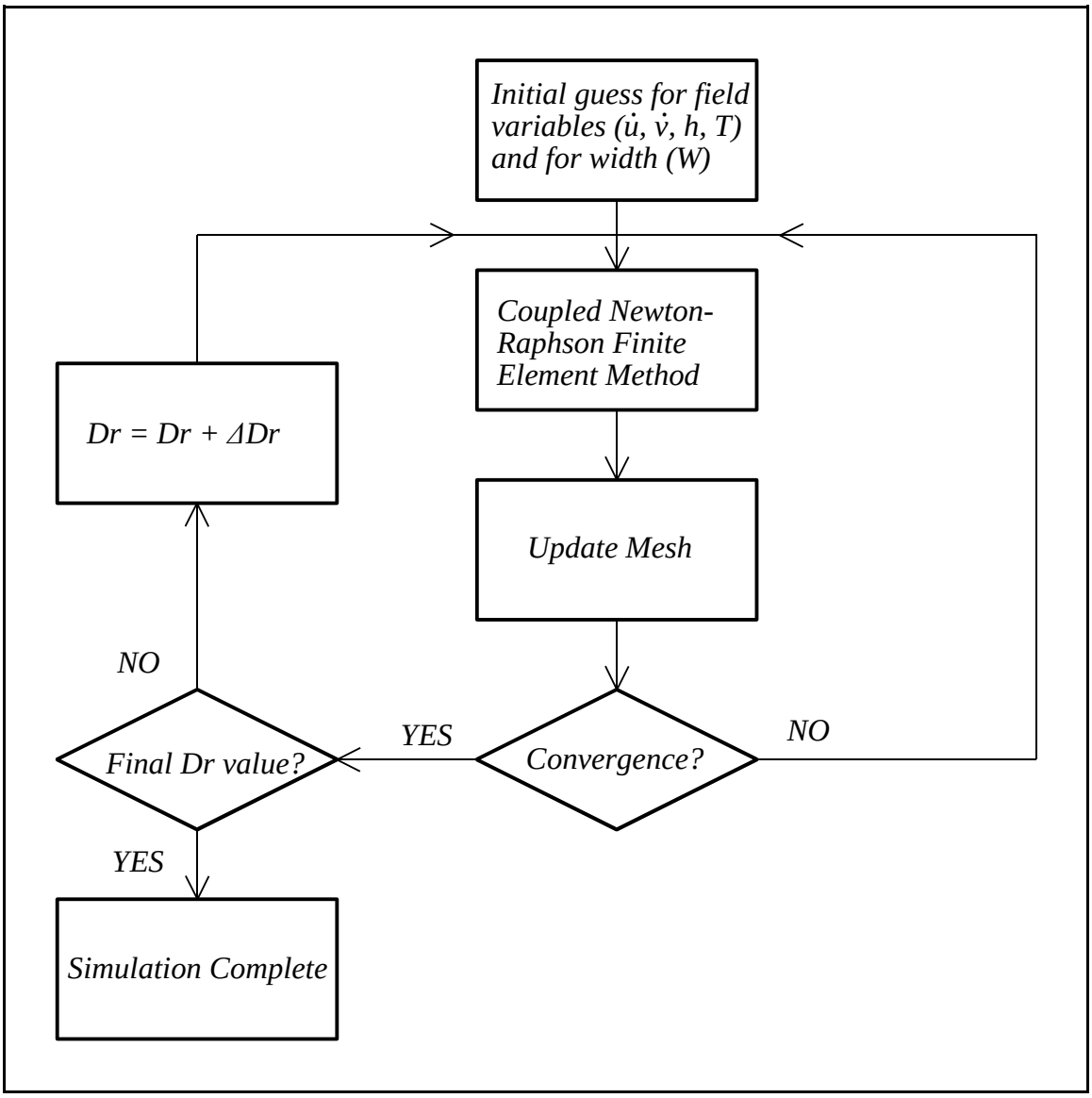


**Figure 8.2** Flowchart for the Eulerian algorithm

As Figure 8.2 shows, an initial guess is needed to start the algorithm. For the simulations conducted here, the initial guess consists of a rectangular domain of dimensions $W_{die}$ by $L$, in which $\dot{v} = 0$, and $\dot{u}$ and $h$ are determined using the 1D closed-form solutions

provided in Appendix G. For the mesh update step, the *y*-coordinates for each column of nodes, as shown in Figure 8.1, must be adjusted to agree with the new predicted width. Each node in each column is updated so that its new *y* value maintains the same ratio to the new width as it had to the previous width. To determine convergence the following criterion is tested:

$$Max\left(\frac{\|\Delta \boldsymbol{a}_u\|}{\|\boldsymbol{a}_u\|},\ \frac{\|\Delta \boldsymbol{a}_h\|}{\|\boldsymbol{a}_h\|},\ \frac{\|\Delta \boldsymbol{a}_T\|}{\|\boldsymbol{a}_T\|},\ \frac{\|\Delta \boldsymbol{a}_W\|}{\|\boldsymbol{a}_W\|}\right) \le toler \qquad \textbf{(8.10)}$$

in which $\boldsymbol{a}_u$, $\boldsymbol{a}_h$, $\boldsymbol{a}_T$, and $\boldsymbol{a}_W$ are the current solutions for the velocity, thickness, temperature and width degrees of freedom, $\Delta$ represents the change in these variables and $\|\cdot\|$ denotes the Euclidean norm of the vector. The E simulation results presented in this thesis use the same value of the tolerance as the UL simulation results: $toler = 10^{-2}$.

## 8.2 Comparison of the Accuracy for 1D Film Casting of a Viscous Fluid

This section reproduces the portion of Smith and Stolle (2001) that compares the accuracy of the UL and E algorithms for the case of 1D film casting. A comparison of the accuracy is possible because in the case of 1D film casting of a viscous fluid a theoretical solution exists. Appendix G provides the closed-form solution for the rate of energy dissipation $\dot{W}^c$ for 1D film casting of a linear viscous fluid. This theoretical solution is used to calculate the relative error in rate of energy dissipation for the E and UL approaches with varying mesh densities, using the input parameters of Table 5.1. Figure 8.3 summarizes the results with a log-log plot of the relative error versus mesh density, where the mesh density

refers to the number of elements in the air-gap. The distinction that the elements must lie in the air-gap is made because, in order to simplify the book-keeping, the numerical algorithm for the UL formulation stores elements inside the die and roll, but these elements do not contribute to the actual solution. Moreover, the elements inside the die and on the roll are not counted for the purposes of comparing the two algorithms because the degrees of freedom for these elements are not part of the finite element equations, as their motion is known *a priori* and thus it is unnecessary to include them in the solution.

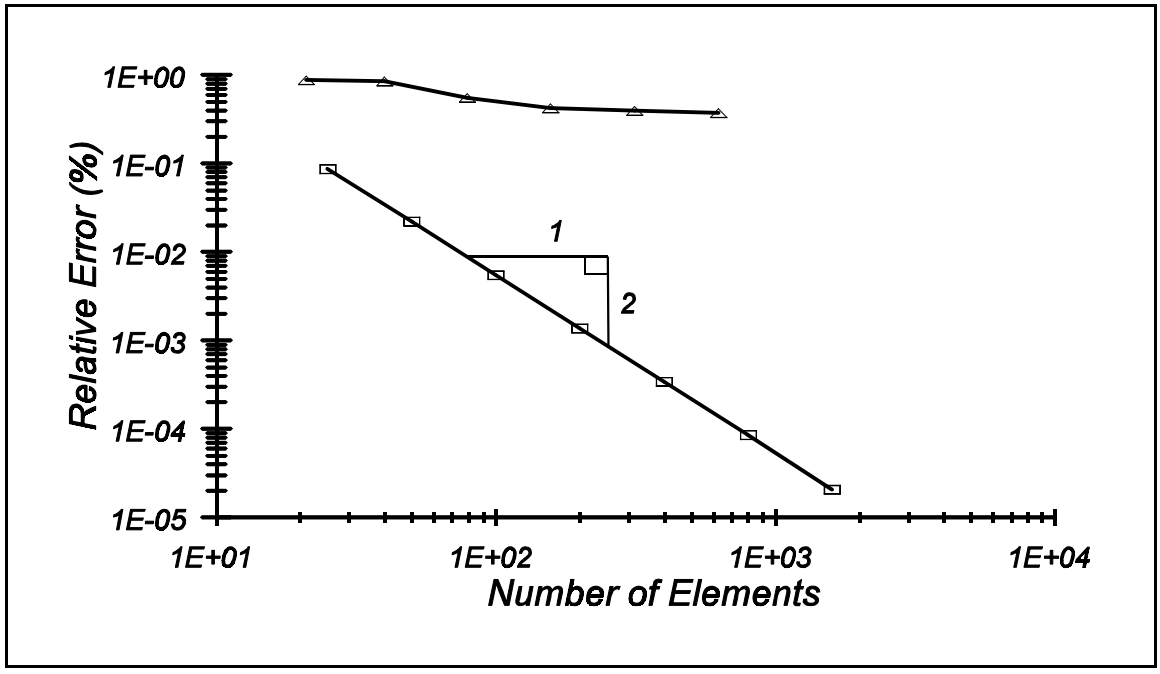


**Figure 8.3** Log-log plot of the relative error in rate of energy dissipation for the E (□) and UL (▽) algorithms

As expected for the E algorithm, the error decreased with a doubling of the mesh, leading to approximately a quartering of the error. The UL algorithm, on the other hand, did not perform as well. For instance, the UL formulation has a greater error than the E

formulation, and the error does not decrease as rapidly when the number of elements are increased. The apparent poorer performance of the UL algorithm relative to the E algorithm is attributed to: i) there are small oscillations in the solution even after it has reached steady state; ii) the film casting problem is formulated in terms of spatial boundary conditions, which the UL scheme can only approximate; and iii) the UL formulation has a viscoelastic constitutive description, which only approximates a viscous fluid and the closed-form solution for $\dot{W}^c$, presented in Appendix G, is for an Eulerian framework. The error associated with the approximation of a viscous fluid by a low relaxation time viscoelastic fluid was investigated further by decreasing the relaxation time, and looking at the corresponding decrease in the relative error, as shown in Figure 8.4. Although the initial trend with a decreasing relaxation time is a decreasing error, the benefit is seen to level off below $\lambda \approx 10^{-3}$s. This levelling off is likely a consequence of the round-off errors associated with performing calculations with small floating point numbers. Apparently a practical limit exists on how well a viscous fluid can be approximated by a viscoelastic fluid with a low relaxation time. As an additional point, the small improvement associated with decreasing the relaxation time below say 0.002 s, is not worth the additional computational effort. Smaller relaxation times require smaller time steps to capture the material response properly. For instance, the simulations for Figure 8.4 required a time step of $10^{-6}$s. As a consequence of the small time step, a very large number of time steps, and a correspondingly large simulation time, was necessary to reach steady-state conditions.

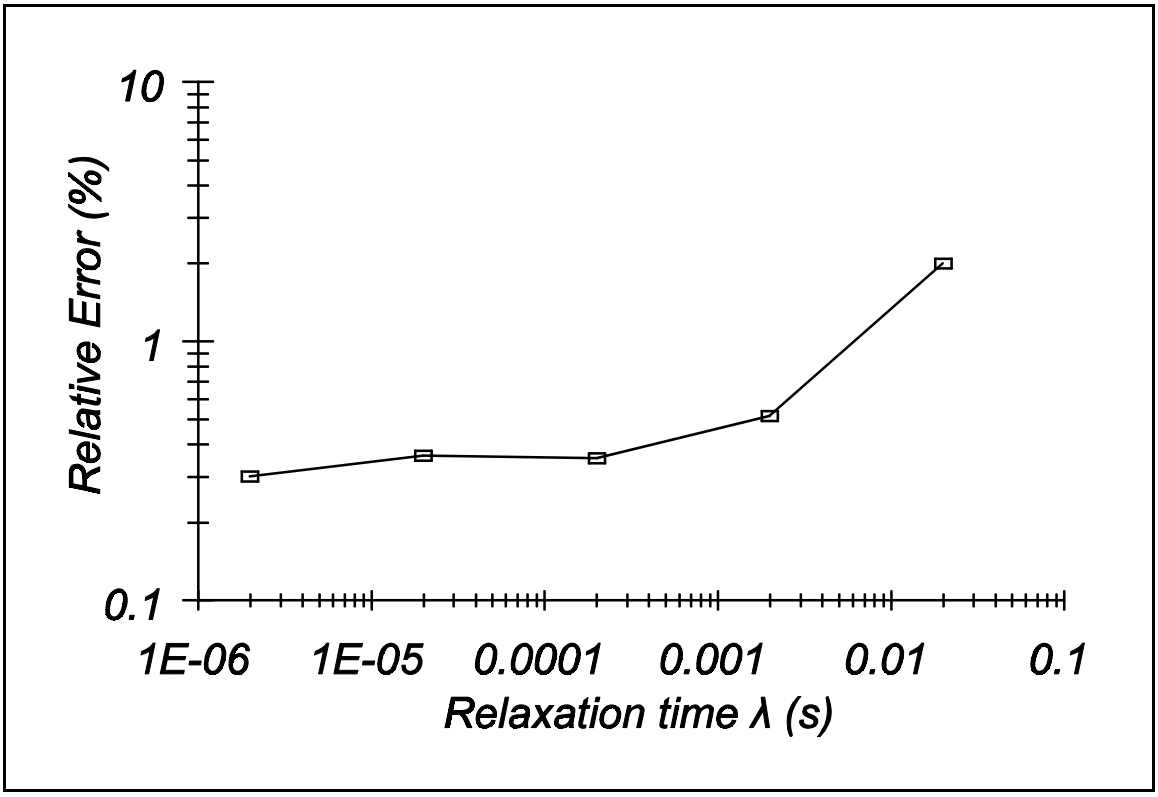


**Figure 8.4** Log-log plot of the relative error in rate of energy dissipation for the UL algorithm with changing relaxation time λ (s)

Although the UL scheme did not perform as well as the E scheme when comparing numerical solutions to analytical solutions, it is worth noting that with a reasonable number of elements the UL scheme has acceptable results, with a maximum relative error less than 1%. One must also recognize that each formulation solves a slightly different problem, with the real physical process having conditions that likely lie somewhere between the two.

## 8.3 Comparison of the Solutions for 2D Film Casting of a Viscous Fluid

Unlike 1D film casting, a closed-form solution is not available for 2D film casting. For the 2D case, the discussion instead focuses on comparing the simulation results of the various numerical algorithms. In Section 7.2 results were presented for the UL and E algorithms, and for other published studies on 2D film casting of a viscous fluid. The comparisons showed disagreement, at times considerable, between the geometry predicted for the film by the various studies. All the E approaches solve the same governing equations and boundary conditions, and the UL approach approximates these same governing equations and boundary conditions, so the differences in the results must be attributed to differences in the numerical algorithms. Table 1.4 summarizes the different numerical algorithms that have been used for simulating film casting. In a general sense, the disagreement in the numerical predictions is a consequence of the highly nonlinear nature of the problem and the strong coupling between the velocity field and the film geometry. A more specific explanation for differences in the simulation results is difficult to determine because the information available from other studies is limited to that provided in the published papers. However, some insight into the differences between E and UL formulations can be gained by comparing the E algorithm summarized in this chapter to the UL algorithm introduced in this thesis.

In this section, four potential explanations for differences in predictions, associated with different algorithms, are explored:

- the element shapes for the two algorithms are different;

- the UL algorithm only approximates the E boundary conditions;
- the solution of the UL algorithm may depend on the initial guess; and,
- although the E and UL solutions for velocity and geometry are dissimilar, the two solutions are difficult for a finite element algorithm to distinguish between because they are relatively close in an energy sense.

Before discussing the potential explanations for the differences in behaviour, the 2D UL simulation results are compared to the 2D E results

### 8.3.1 UL versus E with Triangular Elements

Section 7.2.1 shows the thickness at the chill roll for various studies, using the simulation parameters from d'Halewyu *et al.* (1990). The figure suggests mediocre agreement between the UL and E formulations. However, when the numbers are put into perspective, the agreement is seen to be reasonable. For instance, the relative change from the E to the UL formulations for thickness at the line of symmetry and width at the chill roll are approximately 8 % and 9 %, respectively. Although this difference may appear significant, it is of the same order of magnitude as typical measurement errors. The similarity of the simulation results between the E and UL formulations are shown more dramatically by considering how the thickness changes over the entire plane of the film. Figure 8.5 shows normalized thickness contours, which each represent a 10 % decrease in thickness for every step downstream, for the UL and $E_{tri}$ algorithms. The simulation parameters are the same as those used in Section 7.2.1, except that the number of elements for the $E_{tri}$ simulation were varied, with $40 \leq nelL \leq 52$ and $52 \leq nelW \leq 81$. The number of

elements was varied to investigate the possibility of a dependency of the solution on the mesh density, and no mesh dependency was observed. Figure 8.5 was created using the simulation results for *nelL* = 52 and *nelW* = 81. A comparison of the first two diagrams in the figure indicates that the principle difference between the two studies is that $E_{tri}$ has greater neck-in than the UL algorithm. The other contour plots provided in Figure 8.5 are discussed in later sections.

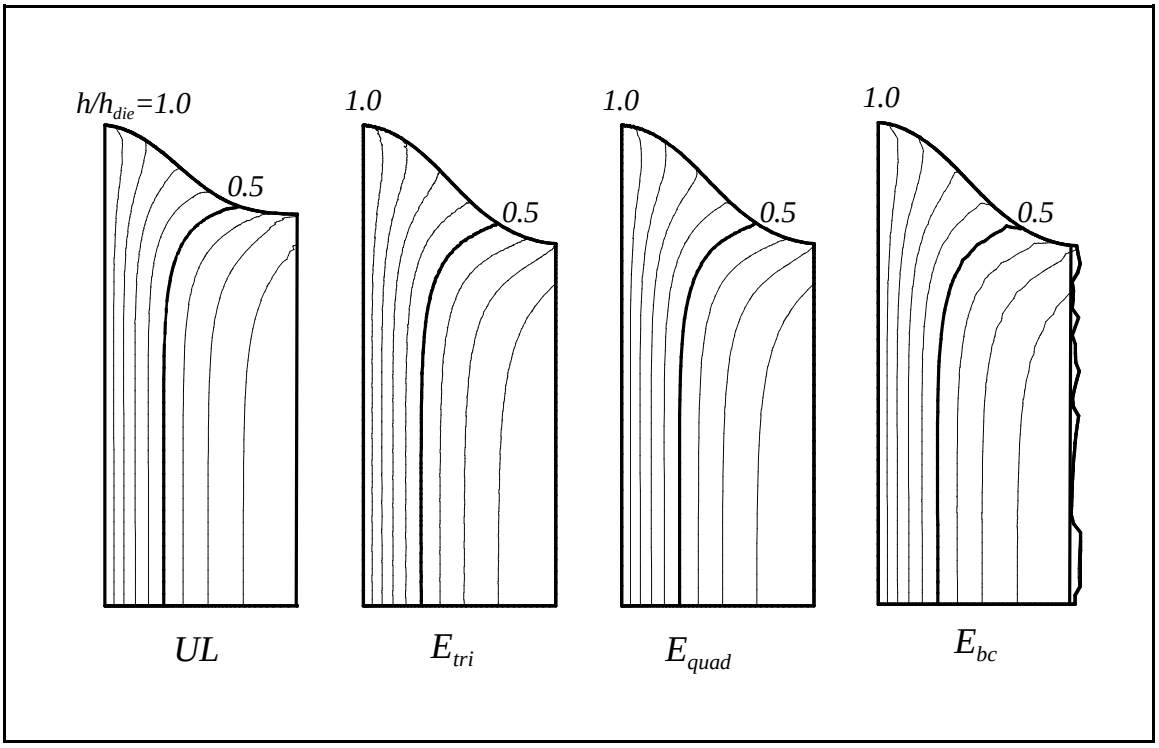


**Figure 8.5** Thickness contours for film casting simulations reproducing d'Halewyu *et al.* (1990), with *Dr* = 10, using the Updated Lagrangian (UL) algorithm and the Eulerian algorithm with triangular elements ($E_{tri}$), quadrilateral elements ($E_{quad}$) and UL boundary conditions ($E_{bc}$)

Although an argument can be made that the E and UL results are in reasonable agreement for the d'Halewyu *et al.* (1990) simulation, when the Debbaut *et al.* (1995)

$Dr = 20$ simulation is reproduced, the results of the E and UL algorithms are very different. This is demonstrated in the thickness at the chill roll plot of Section 7.2.2, where the magnitude of the relative difference in thickness at the line of symmetry and width at the chill roll, between the E and UL formulations, is approximately 36 % and 51 %, respectively. The thickness distribution over the plane of the film also varies considerably between the two approaches, as shown in Figure 8.6. One possible reason for the difference in the thickness distributions could be that at the higher draw ratios the film is closer to instability. Although the E algorithm discussed here completely ignores instability, the UL solution could be influenced by phenomena associated with the approaching instability. Other possible explanations for the observed differences in the film geometries are discussed in the sections that follow.

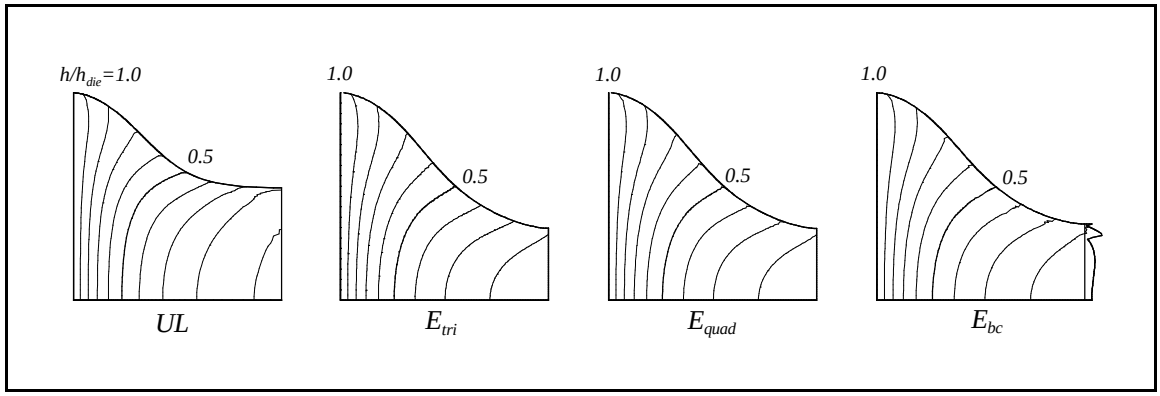


**Figure 8.6** Thickness contours for the film casting simulations reproducing Debbaut *et al.* (1995), with $Dr = 20$, using the Updated Lagrangian (UL) algorithm and the Eulerian algorithm with triangular elements ($E_{tri}$), quadrilateral elements ($E_{quad}$) and UL boundary conditions ($E_{bc}$)

### 8.3.2 Use of Quadrilateral Elements for the E Formulation

The UL and E algorithms as originally developed made use of different element types; therefore, the possibility existed that the observed differences could be due to mesh dependencies. To investigate this, the E algorithm was reformulated using quadrilateral elements. Figures 8.5 and 8.6 show that the thickness contours for the quadrilateral elements ($E_{quad}$) are essentially the same as those previously obtained using $E_{tri}$. Consequently, the difference in element shapes does not explain the greater neck-in obtained with the E algorithm.

### 8.3.3 Use of UL Boundary Conditions for the E Formulation

One of the principle distinctions between the UL and E algorithms is that the UL mesh only approximates the spatial boundary conditions of the E algorithm. To investigate whether the boundary conditions could account for the observed differences, the E algorithm was implemented using the UL boundary conditions. The simulation results are shown as $E_{bc}$ in Figures 8.5 and 8.6. For the simulations that reproduce the film problems discussed by d'Halewyu *et al.* (1990) and Debbaut *et al*. (1995), the thickness contours are essentially identical to those previously obtained using the E formulation; therefore, for the problem analysed the change in boundary conditions does not account for the larger neck-in of the E simulations.

### 8.3.4 Influence of the Initial Guess on the UL Formulation

Most of the UL simulations conducted for this thesis began with all the elements inside the die and with the initial stresses and the accumulated creep strain set to zero. One may ask whether this initial guess has some influence on the final solution. To investigate this possibility, a UL simulation was conducted with an initial guess corresponding to the final geometry of the $E_{quad}$ simulation shown in Figure 8.5. Convergence, as demonstrated by the time histories in Figure 8.7, occurred in $5\times10^4$ time steps, and the final solution was essentially the same as that previously obtained with the UL algorithm. This result is not unexpected, given that the initial $E_{quad}$ elements will eventually migrate out of the air-gap and thus their influence will eventually damp out of the system. Interestingly, although the solution starts close to the final solution, it still takes approximately the same number of time steps for the transient response to die out as when starting with all elements inside the die. An important observation shown in Figure 8.7 is that the $\dot{W}^c$ history is almost a flat curve. Although the geometry of the film changes, in an energy sense there is little to distinguish the two solutions; i.e., the E solution corresponds to $t = 0$ and the UL solution corresponds to $t > 0$. The fact that the solutions are so close in an energy sense could explain why different algorithms find different solutions. The finite element method optimizes the energy dissipated, but the optimum is difficult to determine because adjacent solutions are very close to optimal.

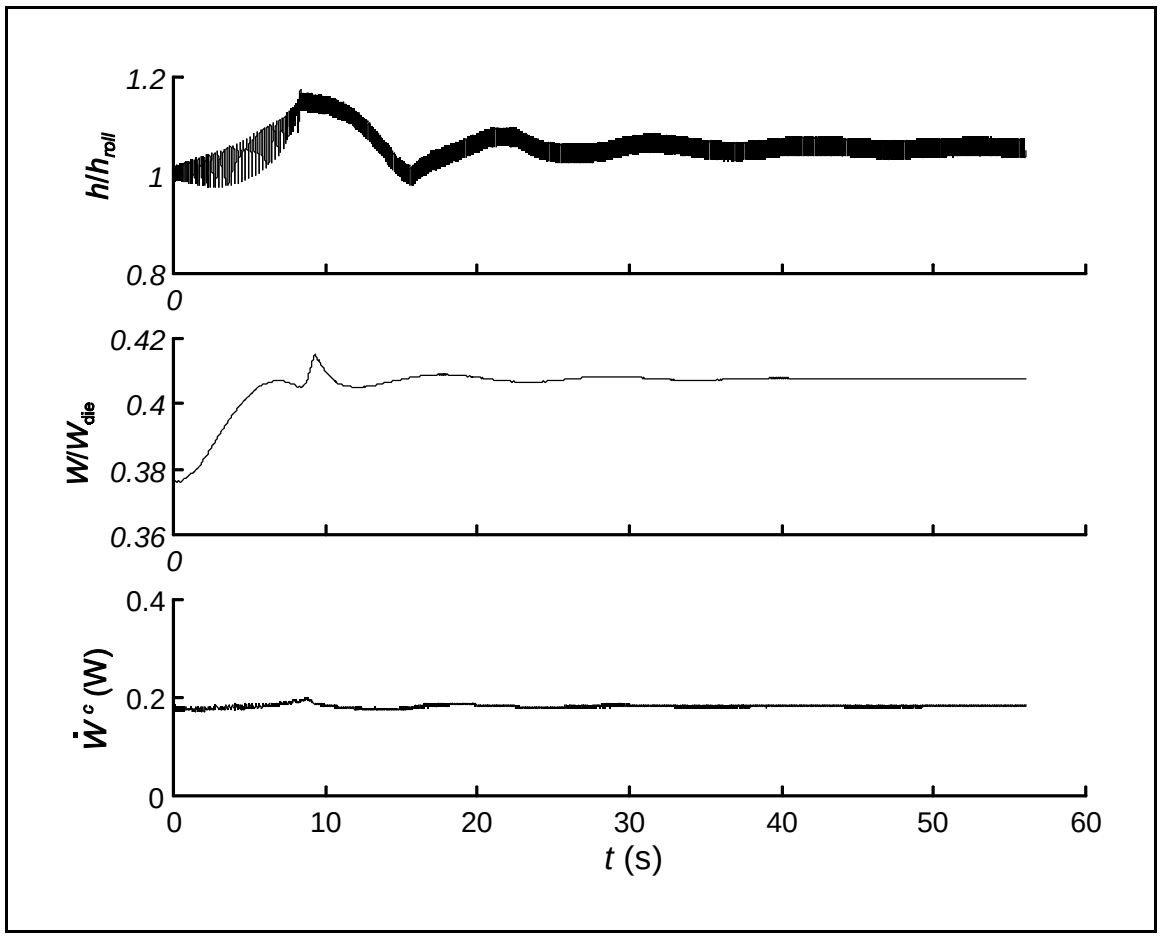


**Figure 8.7** Histories for the UL algorithm starting from the $E_{quad}$ final solution of normalized thickness at the line of symmetry, normalized width at the chill roll and viscous dissipation

## 8.4 Comparison of the Algorithms

In this section the UL and E algorithms are compared with respect to complexity, speed, and storage requirements. The comparison is not quantitative or rigorous; instead, the idea is to make some qualitative statements about how the algorithms compare in a general sense.

### 8.4.1 Comparison of Complexity

The two algorithms are of roughly equal in terms of their overall complexity. In this context the definition of complexity refers to the difficulty of formulating and understanding the conceptual details of the algorithms; it does not refer to a formal count of the number of computer operations. The judgement that the two algorithms are equal in complexity is based on the experience of implementing both of the algorithms. In the process of implementing the algorithms some general observations with respect to their complexity were noted, as follows:

- The UL algorithm has the complications of time-stepping and the radial-return algorithm, whereas the E algorithm has the complications of a fully coupled Newton-Raphson algorithm and explicitly solving for the free surface.
- The complexity of the E algorithm would increase if upwinding were introduced; upwinding is sometimes necessary for the transport equations, either for mass or thermal energy, in an E framework. The complication of upwinding is incorporated in one 2D film casting study (Debbaut *et al.* 1995) in order to numerically solve the continuity equation.

### 8.4.2 Comparison of Speed

The E algorithm was found to be much faster than the UL algorithm. For the simulations discussed in Section 8.2, with $Dr = 10$, the E algorithm took 4 iterations, whereas the UL algorithm took $5\times10^4$ time steps, with approximately 5 sub-iterations for each step.

This difference was even more pronounced when *Dr* was increased to 20; the E algorithm took 6 iterations and the UL algorithm needed approximately $4.0\times10^6$ time steps (see Figure 5.5). The reason for the dramatic difference between the two algorithms is that the E algorithm finds the steady state solution directly, while the UL algorithm has to wait for the transient behaviour to die out and the transient behaviour takes longer to damp out as the draw ratio increases.

If the E algorithm were changed to incorporate time-stepping, then it would likely be slower than the UL algorithm because the E algorithm would require as many time steps as the UL to reach steady-state, but the solution of each step would be more time consuming because the coupled analysis of the E algorithm has a larger bandwidth stiffness matrix than the uncoupled UL algorithm. Also, the stiffness matrix for the E algorithm is unsymmetric, so that the analysis cannot take advantage, as the UL algorithm can, of the fast solvers that are available for positive definite symmetric systems of equations.

### 8.4.3 Comparison of Storage

As to the respective storage requirements of the two algorithms, the UL requires less memory for the same number of elements, since, as mentioned above, its stiffness matrix is symmetric, while that for the E algorithm is not. Of course a significant advantage of the 1D E algorithm in terms of storage is that it requires fewer elements than the UL algorithm for similar accuracy, as demonstrated in Section 8.2. However, for the 2D simulations the E algorithm also needs a significant number of elements to accommodate the gradients in the

transverse direction, especially near the film's edge. The UL algorithm does have some additional storage requirements over the E algorithm, because in the UL algorithm it is necessary to store the history dependent quantities, such as the stress and the total effective creep strain. The additional storage requirements however, are relatively small when compared to the storage needed for the stiffness matrix.

## 8.5 Advantages of the UL Algorithm

The principle advantages of the UL algorithm over the E algorithm is that it is a more intuitive and natural approach. The approach is intuitive in the sense that the equations and theories of continuum mechanics are first formulated with reference to the material, and in the UL approach the focus is on the material. In the E algorithm it is necessary to introduce extra mathematics to account for the fact that the mesh is spatially fixed, but the material is moving. Another advantage of the UL algorithm is that it does not mix different "types" of degrees of freedom in one analysis. The UL algorithm works in terms of displacements, whereas the E algorithm includes degrees of freedom for velocities and for the film geometry. In the UL approach the geometry is naturally updated as a consequence of predicting the displacements, but in the E approach the values for the new thickness and width must be explicitly solved. Further advantages of the UL algorithm are discussed in the sections that follow. Section 8.5.1 discusses how the UL algorithm determines instability as a response problem. Sections 8.5.2 and 8.5.3 highlight the fact that a constitutive response that depends on the thermomechanical history of the material is more naturally implemented

in a UL framework. The final advantage, which is discussed in Section 8.5.4, is the more robust convergence characteristics of the UL algorithm.

### 8.5.1 Determination of Instability

The UL algorithm directly accommodates the detection of instability, since film casting is treated as a response problem. If draw resonance occurs, then it will be observed in the simulated solution. It is because the UL algorithm detects instability as a response problem that it takes longer to reach steady state for $Dr = 20$ than for $Dr = 10$. The usual approach used in the polymer processing literature to identify instability is linear perturbation analysis. Appendix M summarizes the linear perturbation analysis for 1D film casting of a viscous fluid. As this Appendix shows, the process is mathematically complex even for a simple constitutive equation and a 1D analysis. The analysis becomes considerably more involved for power-law (Aird and Yeow 1983) and for viscoelastic fluids (Anturkar and Co 1988). If the analysis is modified for 1.5D simulations other complications are introduced, as demonstrated by Silagy *et al*. (1996a, 1996b). A linear perturbation analysis has apparently not been published for 2D film casting. Instead the studies that consider the stability of 2D films use the approach adopted in this thesis of observing the draw resonance as a response problem.

The E algorithm in its current form cannot detect draw resonance and will in fact predict “impossible” solutions with draw ratios greater than the critical draw ratio of 20.2. The E algorithm can however be modified to detect instability by adding the transient terms

to the governing equations (Barq *et al*. 1990; Barq *et al*. 1994; Silagy *et al*. 1998; Silagy *et al*. 1999). However, if this change is made, the E algorithm loses the advantage of speed, as discussed in Section 8.4.2. It is worth noting that, unlike the UL algorithm, time-stepping E algorithms are usually supplied with an artificial perturbation of the solution in order to demonstrate instability. In the studies of Barq *et al*. (1990, 1994) and Silagy *et al*. (1999) a perturbation is added to the roll velocity in order to induce oscillations, which can be monitored to determine whether the film is stable or not.

### 8.5.2 Constitutive Description

The response of most polymers is not entirely viscous, and a more realistic viscoelastic constitutive equation is desirable. The UL algorithm already incorporates viscoelasticity, as each element is essentially a Maxwell body. Although the constitutive equation for the UL algorithm adopted in this thesis is fairly simple, the changes necessary for a more complex constitutive equation are straightforward. Different constitutive equations can be implemented by changing the state equation that predicts the rate of creep straining (Equation 2.8). This may involve tracking different history dependent properties, but because the property can be "stored" with the element the algorithmic book-keeping required is straightforward.

The complexity of the E algorithm increases dramatically when viscoelasticity is introduced, since E algorithms are not naturally set up to track particle paths or to take into account deformation history. The extraction of the history of particles requires separate

explicit integration along the streamlines (Luo and Mitsoulis 1990) or the use of convected derivatives (Marchal and Crochet 1987). Moreover, the E framework can obscure the extent of past deformations, unless some special measures are taken to capture this information. The UL approach, on the other hand, quickly summarizes the past deformation history through the current shape of the finite elements, as demonstrated via Figure 7.1.

### 8.5.3 Temperature Dependence

The E algorithm summarized in Section 8.2 is for a viscous fluid, for which the temperature only effects the viscosity. If a nonisothermal viscoelastic fluid is introduced, the algorithm is more complicated as it is necessary to accommodate the influence of both the temperature and the deformation histories. In an E framework, this is typically done by shifting the time scale, as shown for 1D film casting in the study of Alaie and Papanastasiou (1991). The UL framework avoids the complication of shifting the time scale by explicitly tracking the material. The temperature-dependent properties are updated as the mesh deforms.

### 8.5.4 Convergence Characteristics

The UL algorithm has better convergence characteristics than the E algorithm in that the UL algorithm is not overly influenced by the initial mesh. Whether the algorithm begins with all elements inside the die, or with some configuration of elements in the air-gap, the time-stepping generally leads to a steady-state solution for a stable film problem. On the

other hand, the E algorithm does not converge if the initial guess is not close enough to the final solution. This observation is likely due to the choice of the Newton-Raphson method for solving the system of equations, as the Newton-Raphson algorithm requires a solution that is "sufficiently" close to the root (Chapra and Canale 1990).

Another advantage of the UL algorithm is that when convergence problems do occur, they provide insight into the physical process. In this way a negative is turned into a positive feature of the algorithm. For instance, if the transient behaviour does not die out, or leads to "breakage" of the film, then instability has been identified. Another example occurs when the UL algorithm halts because of an ill-conditioned stiffness matrix due to excessive mesh deformations at the die or roll. The mesh distortions that lead to the ill-conditioned matrix are a consequence of high gradients and/or rotation and distortion of the elements; therefore, the convergence problems are an indication of real factors in the physical problem.

## 8.6 Spatial Boundary Conditions and a Material Mesh

As discussed in Section 3.8, the UL algorithm, especially for the 2D case, only approximates the spatial location of the die and roll where the boundary conditions on the film are modified. The uneven and changing boundary conditions are partly responsible for limiting the draw ratio that can be obtained with the UL algorithm in a 2D framework. In defence of the UL algorithm, the imperfect satisfaction of the transition from one set of boundary conditions to another is a mathematical problem, not a physical one. The real film casting process will probably not have die and roll locations that can be precisely defined

over time. The location of the boundary conditions likely migrate slightly over time, with the boundaries seldom, if ever, corresponding to a straight line. The spatial boundary conditions used for the E algorithm are attractive from a computational viewpoint, but in a sense they are no more correct than the UL boundary conditions, as both are idealizations of the real process.

# Chapter 9 Conclusions and Recommendations

This thesis presented a new numerical algorithm for 2D nonisothermal simulations of a nonlinear viscoelastic cast film process. The algorithm is new with respect to how it is implemented and with respect to the physical phenomena included in the governing equations. In the case of the implementation, the algorithm described in this thesis is the first to model film casting using an updated Lagrangian description of the motion. Furthermore, the algorithm provides one of the few examples of determining draw resonance as a response problem, as opposed to the more common approach of linear stability analysis. When compared to the existing literature, the algorithm described in this thesis also contributes to the body of knowledge on film casting by removing some of the simplifying assumptions used in previous studies. The new features of the model include the following:

i) The transient behaviour of a 2D film can be observed;

ii) Use is made of a constitutive equation unlike those generally employed in polymer processing. The constitutive equation accommodates viscoelasticity, extensional thinning/thickening, and strain-hardening.

iii) The influence of temperature on the stability of 2D films can be observed.

The body of this chapter is divided into two main sections: Section 9.1, which summarizes the simulation results and the differences between UL and E algorithms, and

Section 9.2, which consists of recommendations for future work. Following these two sections, concluding remarks are provided in Section 9.3.

## 9.1 Summary

Parametric studies were conducted for the 1D, 1.5D and 2D versions of the UL algorithm. The results of these studies are summarized in Section 9.1.1. Besides presenting the results of simulations, the thesis also discussed the differences between and the advantages and disadvantages of the UL and E formulations. Section 9.1.2 provides the highlights of this discussion.

### 9.1.1 Summary of Simulation Results

The simulations in Chapter 5 illustrated the influence of the material properties and processing conditions on the steady-state 1D velocity and thickness distributions in the air-gap. As the polymer is assumed incompressible, the product of the velocity and thickness at any distance from the die must be constant. Therefore, the points used to summarize the results only need to refer to the changes in the thickness, with the understanding that the conservation of mass will cause a corresponding change in the velocity. The simulations in Chapter 5 lead to the following conclusions:

- extensional thinning (increasing $m$) decreases the thickness gradient at the die
- extensional thickening (decreasing $m$) increases the thickness gradient at the die
- strain-hardening ($n < 1$) increases the thickness gradient at the die

- the elasticity of the melt (increasing $\lambda$) decreases the thickness gradient at the die
- heat transfer (increasing $\alpha$) increases the thickness gradient at the die

Chapter 5 also considered draw resonance in 1D film casting and the following observations were made:

- compared to a viscous fluid ($m = 1$), extensional thinning ($m > 1$) decreases stability, whereas extensional thickening ($m < 1$) increases stability
- increases in strain-hardening cause decreases in stability
- increases in $\lambda$ lead to decreases in stability
- increases in $\alpha$ lead to dramatic increases in stability

In Chapter 6 attention was focussed on the so-called 1.5D simulations, where the thickness is not allowed to vary across the width of the film. This kinematic assumption about the thickness is a popular simplifying assumption in the film casting literature. The discussion in Chapter 6 suggests the following conclusions:

- higher aspect ratios (increases in the air-gap length relative to the die width) lead to an increase in neck-in and a higher thickness at the chill roll
- higher aspect ratios have a stabilizing influence on the film
- the 1.5D assumption is not a good approximation of the film casting process because the restraining influence of the edge-bead is not accommodated

The 1D and 1.5D assumptions were dropped in Chapter 7, where the analysis turned to 2D simulations. The steady-state simulation results presented in Chapter 7 show that, for the draw ratios considered, changes to the material properties do not have a dramatic influence on the film's geometry. This observation suggests that, at least for the case of

lower draw ratios, the solution for the film casting problem is continuity driven. The instability of 2D films was also discussed in Chapter 7 and it was concluded that the trends with changing constitutive parameters and nonisothermal conditions are the same as for the 1D simulations and that higher aspect ratios have a stabilizing effect, like that observed for the 1.5D simulations.

### 9.1.2 UL versus E Formulations for Film Casting

One of the principal questions asked by this thesis is whether UL algorithms hold promise for the simulation of continuous polymer processing, in particular for the simulation of film casting. To answer this question it was first necessary to relate the terminology used in the polymer processing literature to the conventions adopted for the UL constitutive equation. This was the purpose of Chapter 4, where mathematical relations were developed to relate the E versions of power-law viscous and linear viscoelastic fluids to the UL constitutive equation. However, in the case of nonlinear viscoelasticity, Chapter 4 illustrates that the mapping between the two formulations is unclear. Moreover, it is suggested that, in some respects, the UL approach provides a more natural analog of the idealized Maxwell fluid for two reasons: the rate of deformation tensor used in the E approach is not equivalent to the rate of strain tensor, and the convected stress rates chosen for the E constitutive equations may not be conjugate to the rate of deformation tensor in the energy sense. This second point is suggested by the common practise in the chemical engineering literature of

deriving new constitutive equations by changing the definition of the objective stress rate with no corresponding modification to the associated rate of deformation tensor.

The investigation of the potential of the UL algorithm to simulate film casting was pursued further in Chapter 8, where the UL algorithm is compared to several different E algorithms. Table 9.1 summarizes the Chapter 8 conclusions with respect to the advantages and disadvantages of each type of algorithm.

**Table 9.1 A Comparison of the UL and E algorithms**

| | **Advantages** | **Disadvantages** |
|---|---|---|
| **E** | • accurate for 1D viscous<br>• fast | • would lose the speed advantage if time-stepping is incorporated<br>• more complex for treating viscoelastic constitutive equations<br>• can be sensitive to the initial guess<br>• different dof "types" (mechanical and geometric degrees of freedom are included in the same analysis) |
| **UL** | • a natural and intuitive approach<br>• draw resonance is predicted as a response problem<br>• complex constitutive equations are relatively easy to implement<br>• robust convergence behaviour<br>• advection is not necessary for the thermal analysis or for the continuity equation<br>• the dof are of the same "type" (the mechanical analysis uses displacement dof to predict the velocity field and the geometry)<br>• the deformation of the material mesh provides a picture of the deformation history of the material particles | • in boundary conditions is only approximated<br>• slow to reach steady-state<br>• the rotation and distortion of the finite elements can lead to an ill-conditioned stiffness matrix |

Table 9.1 shows that the UL description of motion is a viable alternative to the usual E description for simulating film casting. Although the UL approach has its drawbacks, it does provide a powerful framework for the numerical simulations and it accommodates a wide range of materials and processing conditions. Moreover, some of the disadvantages of the

algorithm can, in a sense, be interpreted as advantages. For instance, the approximation of the spatial location of the die and roll may be closer to the physics of the actual film casting process than the mathematical idealization of straight unchanging boundaries. Furthermore, the distortion of the mesh, while potentially leading to an ill-conditioned stiffness matrix, also provides a useful picture of where and how a given material particle will deform over time.

Chapter 8 also compares the solutions obtained for 2D film casting of a viscous fluid using the UL algorithm and the E algorithm of Smith and Stolle (2000a). Although the agreement is reasonable at low draw ratios and low aspect ratios, the differences can be significant between the results of the different algorithms. Several possible explanations for the differences were investigated, including the element shapes, the approximation of the boundary conditions, and the initial mesh used for the UL analysis. None of these factors seemed to explain the differences between the solutions of the UL and E algorithms. Instead the differences were explained by the nonlinear nature of the problem and the fact that the algorithms cannot easily distinguish between dissimilar solutions because they are so close in an energy sense. Furthermore, unlike the E algorithm in question, the UL algorithm accommodates transient behaviour, so the observed increase in differences between the solutions as the draw ratio increases might be related to the approaching instability.

## 9.2 Recommendations for Future Work

Although this thesis provides useful insight into the film casting process and the use of a UL description of motion for continuous processing, future work is required to improve the constitutive description. The goal of this analysis was to provide a UL framework for simulating film casting, not to exactly describe the complex rheology of polymers. Now that the framework has been established it would be relatively straightforward to modify the constitutive equation. The question then becomes: what is the best approach to use? The answer to this question would likely lie in collecting experimental data and in increasing the understanding of the mapping between the E and UL frameworks for the complex constitutive equations that have been developed and had success within the E description of motion. Whatever approach is used in the future, it should take advantage of the fact that the constitutive behaviour refers to the material and the UL algorithm is derived in terms of the material.

Another improvement to the existing algorithm would be to increase the draw ratios that can be simulated using the 2D analysis. The main hurdle to overcome here would be the deformation of the mesh and the associated problems for the conditioning of the stiffness matrix. A desirable algorithm would be one that combines the material tracking nature of the UL algorithm and the stable mesh features of the E approach. The algorithm could make use of the Arbitrary Lagrangian Eulerian (ALE) finite element method (Liu *et al*. 1988), or it could use a spatial mesh and track the deformation history explicitly, as done by Van Den Berg *et al*. (1996) for a geomaterial.

Another suggestion for future work is to take the lessons learned in this thesis and apply them to the similar process of metal casting. In fact, the physics of the film casting process are similar enough to other industrial problems that some of the ideas of this thesis could be applied to problems in the following areas: polymer fibre spinning, downstream secondary treatment of polymer films, biaxial drawing of films, continuous casting using polymers or metals, pulp and paper manufacturing, etc.

## 9.3 Concluding Remarks

The choice of description of motion is an important consideration for the finite element analysis of any problem. In the case of film casting, E algorithms have been popular, and deservedly so for 1D film casting of viscous fluids, since the E scheme is superior to the UL scheme in simplicity, speed and accuracy. The superiority of the E scheme can be traced to the fact that it is specifically tailored to this type of problem. Two tradeoffs are associated with this specific tailoring: i) a lack of robustness; and ii) the difficulty of extending the algorithm to more complex material descriptions and operating conditions.

As presented in this thesis the UL algorithm is more robust than the E algorithm because it naturally picks up the steady-state solution, with little dependence on the initial guess. The UL algorithm can also model viscoelastic fluids and transient phenomena, such as draw resonance. Although the E algorithm performs well for simple problems, the UL algorithm is attractive for complex problems, which include the addition of two-dimensions,

complex viscoelastic constitutive equations, and nonisothermal effects. The advantage of the UL approach lies in the fact that the principles of mechanics apply directly to the body, not to the region in space that it momentarily occupies. Moreover, the numerical bookkeeping necessary for history-dependent constitutive equations is easier for a UL algorithm, since this information is explicitly stored for each element. The major drawback of the UL algorithm is the difficulty of applying spatial boundary conditions to a material mesh, although this drawback can be mitigated by using a fine mesh and by recognizing that a small migration of the spatial boundaries is likely more representative of the actual physics. In conclusion, UL algorithms are a viable alternative to E algorithms for simulation of continuous polymer processing, such as film casting.

# References


Acierno, D., and Di Maio, L., (2000), Film Casting of Polyethylene Terephthalate: Experiments and Model Comparisons, *Polymer Engineering and Science*, Vol 40, No.1: pp108-117.

Agassant, J. F., Avenas, P., Sergent, J. P. and Carreau, P. J., (1991), *Polymer Processing. Principles and Modeling*, Hanser Publishers, Munich; Vienna and New York.

Aird, G. R. and Yeow, Y. L., (1983), Stability of Film Casting of Power-Law Liquids, *Industrial Engineering Chemical Fundamentals*, 22: pp7-10.

Alaie, S. M. and Papanastasiou, T. C., (1991), Film Casting of Viscoelastic Liquid, *Polymer Engineering and Science*, 31, 2: pp67-75.

Anturkar, N. R. and Co, A., (1988), Draw Resonance in Film Casting of Viscoelastic Fluids: a Linear Stability Analysis, *Journal of Non-Newtonian Fluid Mechanics*, 28: pp287-307.

Avenas, P., Agassant, J. F. and Sergent, J. Ph., (1986), *La Mise en Forme des Matières Plastiques. Technique et Documentation*, 2nd ed., Lavoisier, Paris.

Barq, P., Haudin, J. M. and Agassant, J. F., (1992), Isothermal and Anisothermal Models for Cast Film Extrusion, *International Polymer Processing*, VII, 4: pp334-349.

Barq, P., Haudin, J. M., Agassant, J. F., and Bourgin, P., (1994), Stationary and Dynamic Analysis of Film Casting Process, *International Polymer Processing*, IX, 4: pp350-358.

Barq, P., Haudin, J. M., Agassant, J. F., Roth, H. and Bourgin, P., (1990), Instability Phenomena in Film Casting Process, *International Polymer Processing*, V, 4: pp264-271.

Bathe, K. J., (1982), *Finite element procedures in engineering analysis*, Prentice-Hall, Englewood Cliffs, N.J.

Beaulne M., and Mitsoulis, E., (1999), Numerical Simulation of the Film Casting Process, *International Journal of Polymer Processing*, 3: pp261-275.

Bird, R. B., (1987), *Dynamics of Polymeric Liquids*, Wiley, New York.

Borja, R. I. and Lee, S. R., (1991), Cam-Clay Plasticity, Part 1: Implicit Integration of Elasto-Plastic Constitutive Relations, *Computer Methods in Applied Mechanics and Engineering*, 78, pp. 48-72.

Chambon, F., Ohlsson, S. and Silagy, D., (1996), Validation of a Model for the Cast-Film Process, *First Joint Topical Conference on Processing, Structure and Properties of Polymeric Materials, Conference Preprint,* American Institute of Chemical Engineers, New York, New York: pp39-42.

Chapra, S. C. and Canale, R. P., (1990), *Numerical Methods for Engineers*, 2nd ed., McGraw-Hill Publishing Company, New York.

Conte, S. D. and deBoor, C., (1980), *Elementary Numerical Analysis an Algorithmic Approach*, 3rd ed., McGraw-Hill Book Company, New York.

Cotto, D., Duffo, P. and Haudin, J. M., (1989), Cast Film Extrusion of Polypropylene Films, *International Polymer Processing*, IV, 2: pp103-113.

d'Halewyu, S., Agassant, J. F. and Demay, Y., (1990), Numerical Simulation of the Cast Film Process, *Polymer Engineering and Science*, 20, 6: pp335-340.

Debbaut, B., Marchal, J. M., and Crochet, M. J., (1995), Viscoelastic effects in film casting in *Zeitschrift fur Angewandte Mathematik und Physick Special Issue*, Casey J. and Crochet M. J. (eds.), Birkhäuser Verlag, Boston, 46: ppS679-S698.

Denn, M. M., (1975), *Stability of Reaction and Transport Processes,* Prentice-Hall, Englewood Cliffs, N. J.

Dobroth, T. and Erwin, L., (1986), Causes of Edge Beads in Cast Films, *PolymerEngineering and Science*, 26, 7: pp462-467.

Duffo, P., Monasse, B. and Haudin, J. M., (1991), Cast Film Extrusion of Polypropylene. Themomechanical and Physical Aspects, *Journal of Polymer Engineering*, 10, 1-3: pp151-228.

Fisher, R. J. and Denn, M. M., (1975), Finite-Amplitude Stability and Draw Resonance in Isothermal Melt Spinning, *Chemical Engineering Science*, 30, pp1129-1134.

Gadala, M. S., Oravas, G. Æ., and Dokainish, M. A., (1983), A Consistent Eulerian Formulation of Large Deformation Problems in Statics and Dynamics, *International Journal of Non-Linear Mechanics*, 18, 1, pp. 21-35.

Iyengar, V. R. and Co, A., (1993), Film Casting of a Modified Giesekus Fluid:A Steady-State Analysis, *Journal of Non-Newtonian Fluid Mechanics*, 48: pp1-20.

Iyengar, V. R. and Co, A., (1996), Film Casting of a Modified Giesekus Fluid: Stability Analysis, *Chemical Engineering Science*, 51, 9: pp1417-1430.

Joseph, D. D., (1990), Fluid dynamics of viscoelastic liquids, Springer-Verlag, New York.

Kraus, H., (1980), *Creep Analysis*, John Wiley & Sons, New York, New York.

Lee, W. K., (1984), A Slit Die Design for Stable Film Extrusion, *Advances in Rheology*, International Congress on Rheology Mexico, Elsevier Science Publishing Company, New York, New York: pp473-481.

Liu, W. K., Chang, H., Chen, J., and Belytschko T., (1988), Arbitrary Lagrangian-Eulerian Petrov-Galerkin Finite Elements for Nonlinear Continua, *Computer Methods in Applied Mechanics and Engineering*, 68, pp259-310.

Lodge, A. S., (1974), *Body Tensor Fields in Continuum Mechanics, with Applications to Polymer Rheology*, Academic Press, New York.

Luo, X. L. and Mitsoulis, E., (1990), An Efficient Algorithm for Strain History Tracking in Finite Element Computations of Non-Newtonian Fluids with Integral Constitutive Equations, *International Journal for Numerical Methods in Fluids*, 11: pp1015-1031.

Malvern, L. E., (1969), *Introduction to the Mechanics of a Continuous Medium*, Prentice-Hall, Englewood Cliffs, New Jersey.

Marchal, J. M. and Crochet, M. J., (1987), A New Mixed Finite Element for Calculating Viscoelastic Flow, *Journal of Non-Newtonian Fluid Mechanics*, 26: pp77-114.

Minoshima, W. and White, J. L., (1983), Stability of Continuous Film Extrusion Processes, *Polymer Engineering Reviews*, 2, 3: pp211-226.

Oldroyd, J. G., (1950), On the Formulation of Rheological Equations of State, *Proceedings of the Royal Society of London A*, 200, pp523-541.

Pearson, J. R. A., (1985), *Mechanics of Polymer Processing*, Elsevier Applied Science, London.

Perzyna, P., (1966), Fundamental problems in viscoplasticity, *Advances in Applied Mechanics*, 9, pp243-377.

Pis-Lopez, M. E. and Co, A., (1996a), Multilayer Film Casting of Modified Giesekus fluids Part 1. Steady-state analysis, *Journal of Non-Newtonian Fluid Mechanics*, 66: pp71-93.

Pis-Lopez, M. E. and Co, A., (1996b), Multilayer Film Casting of Modified Giesekus fluids Part 2. Linear stability analysis, *Journal of Non-Newtonian Fluid Mechanics*, 66: pp95-114.

Rajagopalan, D., (1999), Impact of Viscoelasticity on Gage Variation in Film Casting, *Journal of Rheology*, 43, 1: pp73-83.

Rajagopalan, D., Armstrong, R. C., and Brown, R. A., (1990), Finite element methods for calculation of steady viscoelastic flow using constitutive equations with a Newtonian viscosity, *Journal of Non-Newtonian Fluid Mechanics*, 36: pp159-192.

Rauwendaal, C., (1986), *Polymer Extrusion*, Macmillan Publishing Company, Inc., New York.

Rojiani, K., (1996), *Programming in C with Numerical Methods for Engineers*, Prentice Hall, Englewood Cliffs, N.J.

Sakaki, K., Katsumoto, R., Kajiwara, T. and Funatsu, K., (1996), Three-Dimensional Flow Simulation of a Film-Casting Process, *Polymer Engineering and Science*, 36, 3: pp1821-1831.

Sergent, J. P., (1977), *Etude de deux Procédés de Fabrication de Films. Le Soufflage de Gaine. L'extrusion de Film à Plat*, Thesis, Université Louis Pasteur, Strasbourg.

Shah, Y. T. and Pearson, J. R. A., (1972), On the Stability of Nonisothermal Fiber Spinning, *Industrial Engineering Chemistry Fundamentals*, 11, 2, pp145-149.

Silagy, D., Demay, Y. and Agassant, J. F., (1999), Numerical Simulation of the Film Casting Process, *International Journal of Numerical Methods in Fluids*, 30: pp1-18.

Silagy, D., Demay, Y. and Agassant, J. F., (1998), Stationary and Stability Analysis of the Film Casting Process, *Journal of Non-Newtonian Fluid Mechanics*, 79: pp563-583.

Silagy, D., Demay, Y. and Agassant, J. F., (1996a), Study of the Stability of the Film Casting Process, *Polymer Engineering and Science*, 36, 21: pp2614-2625.

Silagy, D., Demay, Y. and Agassant, J. F., (1996b), Étude de la Stabilité Linéaire de L'étirage d'un Film Newtonien, *Comptes Rendus de l'académie des Sciences*, 322, Série IIb, 4: pp283-289.

Smith, A. A., Hinton, E. and Lewis, R. W., (1983), *Civil Engineering Systems Analysis and Design*, John Wiley & Sons, New York.

Smith, W. S., (1997), *Nonisothermal Film Casting of a Viscous Fluid*, M. Eng. Thesis, McMaster University, Hamilton, ON.

Smith, W. S. and Stolle, D. F. E., (2001), A Comparison of Updated Lagrangian and Eulerian Finite Element Algorithms for the Simulation of Film Casting, accepted to *Finite Elements in Analysis and Design*.

Smith, W. S. and Stolle, D. F. E., (2000a), Nonisothermal Two-Dimensional Film Casting of a Viscous Polymer, *Polymer Engineering and Science*, 40, 8, pp1870-1877.

Smith, W. S. and Stolle, D. F. E., (2000b), Draw Resonance in Film Casting as a Response Problem using a Material Description of Motion, *Journal of Plastic Film & Sheeting*, 16, 2, pp95-107.

Stolle, D. F. E., (1992), Average Strain Quadrilateral Elements, *Communications in Applied Numerical Methods*, 8, pp505-510.

Stolle, D. F. E., (1991), An Interpretation of Initial Stress and Strain Methods and Numerical Stability, *International Journal of Numerical and Analytical Methods in Geomechanics*, 15, pp399-416.

Stolle, D. F. E., Bonnier, P. G. and Vermeer, P. A.. (1997), A Soft Soil Model and Experience with Two Integration Schemes, *Numerical Models in Geomechanics*, pp123-128.

Stolle, D. F. E., Pringle, M. M. and Smith, W. S., (2000) *A Direct Approach for Average Strain Elements*, submitted to International Journal for Computational Civil and Structural Engineering, September, 2000.

Stolle, D. F. E. and Schad, H., (1992), An Updated Reference Configuration Formulation for Large-Deformation Problems, *International Journal of Numerical and Analytical Methods in Geomechanics*, 16, pp295-306.

Tanner, R. I., (1985), *Engineering Rheology*, 2nd ed., Clarendon Press, Oxford.

Tappi Press (1992), *Film Extrusion Manual Process, Materials, Properties*, Tappi Press, Technology Park/Atlanta.

Van Den Berg, P., De Borst, R. and Huétink, H., (1996), An Eulerian Finite Element Model for Penetration in Layered Soil", *International Journal of Numerical and Analytical Methods in Geomechanics*, 20, pp865-886.

Yeow, Y. L., (1974), On the Stability of Extending Films: a Model for the Film Casting Process, *Journal of Fluid Mechanics*, 66, part 3: pp613-622.

Zienkiewicz, O. C., *The Finite Element Method*, (1977), 3rd Edition, McGraw-Hill, London.

# Appendix A Components and Expansions for Various Variables

This appendix summarizes the components for the variables used in the body of the thesis. Table A.1 shows the components of the linear differential operators and Table A.2 expands the vector and tensor variables. Tables A.3 and A.4 summarize the finite element matrices for the thermal analysis and the deviatoric tensor invariants, respectively.

**Table A.1 Linear Differential Operators**

| Variable | Components | Variable | Components |
|---|---|---|---|
| $\nabla$ | $[\partial/\partial x \;\; \partial/\partial y]^T$ | $\boldsymbol{L}$ | $\begin{bmatrix} \frac{\partial}{\partial x} & 0 & \frac{\partial}{\partial y} \\ 0 & \frac{\partial}{\partial y} & \frac{\partial}{\partial x} \end{bmatrix}^T$ |

**Table A.2 Vector and Tensor Variables (written as column vectors)**

| Variable | Components | Variable | Components |
|---|---|---|---|
| $\boldsymbol{u}$, $\dot{u}$ | $[\, u\ v\,]^T$, $[\, \dot{u}\ \ \dot{v}\,]^T$ | $\boldsymbol{\sigma}$ | $[\, \sigma_{xx}\ \sigma_{yy}\ \sigma_{xy}\,]^T$ |
| $\Delta\boldsymbol{\varepsilon}$ | $[\, \Delta\varepsilon_{xx}\ \Delta\varepsilon_{yy}\ \Delta\gamma_{xy}\,]^T$ | $\Delta\boldsymbol{\sigma}$ | $[\, \Delta\sigma_{xx}\ \Delta\sigma_{yy}\ \Delta\sigma_{xy}\,]^T$ |
| $\Delta\boldsymbol{\varepsilon}^c$ | $[\, \Delta\varepsilon^c_{xx}\ \Delta\varepsilon^c_{yy}\ \Delta\gamma^c_{xy}\,]^T$ | $\boldsymbol{s}$ | $[\, s_{xx}\ s_{yy}\ s_{xy}\,]^T$ |

| Variable | Components | Variable | Components |
|---|---|---|---|
| $\boldsymbol{D}^v$ | $[\, D^v_{xx}\ \mathrm{D}^v_{yy}\ \mathrm{D}^v_{xy}\,]^T$ | $\boldsymbol{D}$ | $G\cdot\begin{bmatrix}4 & 2 & 0\\ 2 & 4 & 0\\ 0 & 0 & 1\end{bmatrix}$ |
| $\dfrac{\partial Q}{\partial \boldsymbol{\sigma}}$ | $\left[\dfrac{\partial Q}{\partial \sigma_{xx}}\quad \dfrac{\partial Q}{\partial \sigma_{yy}}\quad \dfrac{\partial Q}{\partial \sigma_{xy}}\right]^T$ | $\dfrac{\partial F}{\partial \boldsymbol{\sigma}}$ | $\left[\dfrac{\partial F}{\partial \sigma_{xx}}\quad \dfrac{\partial F}{\partial \sigma_{yy}}\quad \dfrac{\partial F}{\partial \sigma_{xy}}\right]^T$ |
| $\dfrac{\partial q}{\partial \boldsymbol{\sigma}}$ | $\left[\dfrac{\partial q}{\partial \sigma_{xx}}\quad \dfrac{\partial q}{\partial \sigma_{yy}}\quad \dfrac{\partial q}{\partial \sigma_{xy}}\right]^T$ | $\boldsymbol{I}$ | $[\,1\ 1\ 0\,]^T$ |

In the above table the material properties introduced are $G$, the shear modulus, and $\nu$, Poisson's ratio. The shear modulus is related to the elastic modulus $E$, via $G = E / (2(1+\nu))$, or $G = E/3$, for an incompressible material. The strains are calculated using the standard definitions; that is, $\Delta\varepsilon_{xx} = \dfrac{\partial u}{\partial x}$, $\Delta\varepsilon_{yy} = \dfrac{\partial v}{\partial y}$, $\Delta\varepsilon_{zz} = \dfrac{\partial w}{\partial z}$, $\Delta\gamma_{xy} = \dfrac{\partial u}{\partial y} + \dfrac{\partial v}{\partial x}$. Similarly, the rates of deformation are calculated as follows: $D^v_{xx} = \dfrac{\partial \dot{u}}{\partial x}$, $D^v_{yy} = \dfrac{\partial \dot{v}}{\partial y}$, $D^v_{zz} = \dfrac{\partial \dot{w}}{\partial z}$, $D^v_{xy} = \dfrac{\partial \dot{u}}{\partial y} + \dfrac{\partial \dot{v}}{\partial x}$.

**Table A.3 Finite Element Variables for Solving for the Temperature**

| Variable | Components | Variable | Components |
|---|---|---|---|
| $\boldsymbol{N}_T$ | $\begin{bmatrix}N_1 & N_2 & N_3 & N_4\end{bmatrix}$ | $\mathbf{B}_T$ | $\begin{bmatrix}\dfrac{\partial N_1}{\partial x} & \dfrac{\partial N_2}{\partial x} & \dfrac{\partial N_3}{\partial x} & \dfrac{\partial N_4}{\partial x}\\ \dfrac{\partial N_1}{\partial y} & \dfrac{\partial N_2}{\partial y} & \dfrac{\partial N_3}{\partial y} & \dfrac{\partial N_4}{\partial y}\end{bmatrix}$ |

In Table A.3 the values of $N_1$, $N_2$, $N_3$, and $N_4$ are the usual shape functions for a quadrilateral element (Zienkiewicz 1977: p156). Table A.3 defines the matrices for shape function and shape function gradients for the temperature analysis. The mechanical analysis uses different matrices, which are summarized in Appendix F.

**Table A.4 Expansion of Invariants using the Membrane Approximation**

| Invariant | Expansion |
|---|---|
| $J_2$ | $(s_{xx}^2 + s_{yy}^2 + s_{xx}s_{yy} + s_{xy}^2)$ |
| $q$ | $\sqrt{3(s_{xx}^2 + s_{yy}^2 + s_{xx}s_{yy} + s_{xy}^2)}$ |
| $J_2^{\varepsilon}$ | $(\Delta e_{xx}^2 + \Delta e_{yy}^2 + \Delta e_{xx}\Delta e_{yy} + \Delta e_{xy}^2)$, *where*<br>$\Delta e_{xx} = \Delta\varepsilon_{xx} - \Delta\varepsilon_v/3$<br>$\Delta e_{yy} = \Delta\varepsilon_{yy} - \Delta\varepsilon_v/3$<br>$\Delta e_{xy} = \Delta\gamma_{xy}/2$<br>$\Delta\varepsilon_v = \Delta\varepsilon_{xx} + \Delta\varepsilon_{yy} + \Delta\varepsilon_{zz}$ |
| $\Delta\varepsilon_q$ | $\sqrt{\frac{4}{3}(\Delta e_{xx}^2 + \Delta e_{yy}^2 + \Delta e_{xx}\Delta e_{yy} + \Delta e_{xy}^2)}$ |

In the above table $\Delta e_{xx}$, $\Delta e_{yy}$, and $\Delta e_{xy}$ are the components of the in-plane incremental deviatoric strain tensor. For an incompressible material, as used in this thesis, the deviatoric components are the same as the regular incremental strain components, since $\Delta\varepsilon_v = 0$. The expansion of the above invariants uses the membrane approximation to simplify the out-of-

plane shear components, so that $s_{xz} = s_{yz} = 0$ and $e_{xz} = e_{yz} = 0$. Also, for the deviatoric tensors the remaining out-of-plane components can be related to the in-plane values; that is, $s_{zz} = -(s_{xx} + s_{yy})$ and $e_{zz} = -(e_{xx} + e_{yy})$.

# Appendix B Derivation of the Elasticity Matrix for the Membrane Approximation

The constitutive relation for an elastic material can be expressed as follows:

$$\Delta\boldsymbol{\sigma} = 2G\,\Delta\boldsymbol{\varepsilon}^{e} - \Delta p\,\boldsymbol{I} \qquad \textbf{(B.1)}$$

where the 3D tensors for change in stress and elastic strain are used (in column vector form), $\Delta p$ is the change in the pressure and $\boldsymbol{I} \equiv [1\ 1\ 1\ 0\ 0\ 0]^{T}$. If the membrane approximation is introduced, then the number of components in the change in stress tensor may be reduced by three, since $\Delta\sigma_{zz} = \Delta\sigma_{xz} = \Delta\sigma_{yz} = 0$, but the change in pressure is still unknown. Using the fact that the out-of-plane stress is zero ( $\Delta\sigma_{zz} = 2G\Delta\varepsilon^{e}_{zz} - \Delta p = 0$ ), the pressure can be written in terms of the elastic strain as

$$\Delta p = 2G\,\Delta\varepsilon^{e}_{zz} \qquad \textbf{(B.2)}$$

Using the assumed incompressibility of the elastic strain (Equation 2.2, using the elastic components), the pressure can be expressed in terms of the in-plane elastic strains via

$$\Delta p = -2G\,(\Delta\varepsilon^{e}_{xx} + \Delta\varepsilon^{e}_{yy}) \qquad \textbf{(B.3)}$$

If Equation B.3 is substituted into Equation B.1, then the plane stress components of the change in stress tensor are as follows:

$$\begin{aligned}
\Delta\sigma_{xx} &= 2G\,\Delta\varepsilon^{e}_{xx} + 2G(\Delta\varepsilon^{e}_{xx} + \Delta\varepsilon^{e}_{yy}) \\
\Delta\sigma_{yy} &= 2G\,\Delta\varepsilon^{e}_{yy} + 2G(\Delta\varepsilon^{e}_{xx} + \Delta\varepsilon^{e}_{yy}) \\
\Delta\sigma_{xy} &= G\,\Delta\gamma^{e}_{xy}
\end{aligned} \qquad \textbf{(B.4)}$$

where the relationship that $\Delta\gamma_{xy}^{e} = 2\Delta\varepsilon_{xy}^{e}$ has been employed.

Using the column vector notation for the change in stress and strain tensors, the above relation (Equation B.4) can be expressed as

$$\Delta\boldsymbol{\sigma} = \boldsymbol{D}\,\Delta\boldsymbol{\varepsilon}^{e}, \quad \boldsymbol{D} = G \cdot \begin{bmatrix} 4 & 2 & 0 \\ 2 & 4 & 0 \\ 0 & 0 & 1 \end{bmatrix} \tag{B.5}$$

in which the change in stress and strain tensors are now modified to only include the plane stress components.

# Appendix C Derivation of the Finite Element Equations for the Implicit Creep Algorithm

The derivation of the finite element equations for creep follows the approach presented by Stolle (1991). To estimate the displacements for the $(i+1)^{th}$ time step the residual for that time step ($\boldsymbol{\Psi}_{i+1}$) should be approximately zero, as shown below

$$\boldsymbol{\Psi}_{i+1} \equiv \int_V \boldsymbol{B}^T \boldsymbol{\sigma}_{i+1} dV - \boldsymbol{R} = \mathbf{0} \tag{C.1}$$

The stress change over the time step may be written as

$$\boldsymbol{\sigma}_{i+1} = \boldsymbol{\sigma}_i + \Delta\boldsymbol{\sigma}_i \tag{C.2}$$

Introducing the constitutive matrix allows the stress increment to be related to the total and creep strain increments

$$\Delta\boldsymbol{\sigma}_i = \boldsymbol{D}\,(\Delta\boldsymbol{\varepsilon}_i - \Delta\boldsymbol{\varepsilon}_i^c) \tag{C.3}$$

The creep increment can be calculated from the creep strain rate

$$\dot{\boldsymbol{\varepsilon}}^c = \dot{\varepsilon}_q^c \frac{\partial \psi}{\partial \boldsymbol{\sigma}} \tag{C.4}$$

For a fully implicit approach the variables are evaluated at the end of the time step, so the creep strain increment is as follows:

$$\Delta\boldsymbol{\varepsilon}_i^c = \Delta t_i \dot{\boldsymbol{\varepsilon}}_{i+1}^c = \Delta t_i \dot{\varepsilon}_{q_{i+1}}^c \frac{\partial \psi}{\partial \boldsymbol{\sigma}} \tag{C.5}$$

Now $F$ is defined as

$$F = \Delta t \dot{\varepsilon}_q^c = \Delta \varepsilon_q^c \quad \textbf{(C.6)}$$

Taylor's expansion can be applied to $F$ to find $F$ at the end of the time step ($F_{i+1}$)

$$F_{i+1} = F_i + \Delta F_i = F_i + \left(\frac{\partial F}{\partial \boldsymbol{\sigma}}\right)^T \Delta \boldsymbol{\sigma}_i + \frac{\partial F}{\partial \varepsilon_q^c} \Delta \varepsilon_q^c = F_i + \left(\frac{\partial F}{\partial \boldsymbol{\sigma}}\right)^T \Delta \boldsymbol{\sigma}_i + \frac{\partial F}{\partial \varepsilon_q^c} F_{i+1} \quad \textbf{(C.7)}$$

If Equations C.3 and C.5 are substituted into the above equation, then the following results, after rearranging

$$F_{i+1} = C_1 [F_i + \left(\frac{\partial F}{\partial \boldsymbol{\sigma}}\right)^T \boldsymbol{D} \Delta \varepsilon_i] \quad \textbf{(C.8)}$$

where

$$C_1 = [1 + (H_e + H_c)]^{-1}, \quad H_e = \left(\frac{\partial F}{\partial \boldsymbol{\sigma}}\right)^T \boldsymbol{D} \frac{\partial \psi}{\partial \boldsymbol{\sigma}}, \quad H_c = -\frac{\partial F}{\partial \varepsilon_q^c} \quad \textbf{(C.9)}$$

Equation C.8 and Equation C.5 may be used to express the creep stress increment (Equation C.3), which in turn may be substituted into Equation C.1 to yield the required finite element equations

$$\int_V \boldsymbol{B}^T \boldsymbol{D}^{ve} \boldsymbol{B} \, dV \, \Delta \boldsymbol{a} = \boldsymbol{R} - \int_V \boldsymbol{B}^T \boldsymbol{\sigma} dV + \int_V \boldsymbol{B}^T \Delta \boldsymbol{\sigma}^c dV \quad \textbf{(C.10)}$$

with

$$\boldsymbol{D}^{ve} = \boldsymbol{D} - C_1 \boldsymbol{D} \frac{\partial q}{\partial \boldsymbol{\sigma}} \left(\frac{\partial F}{\partial \boldsymbol{\sigma}}\right)^T \boldsymbol{D} \quad \textbf{(C.11)}$$

$$\Delta \boldsymbol{\sigma}^c = C_1 F \boldsymbol{D} \frac{\partial q}{\partial \boldsymbol{\sigma}} \quad \textbf{(C.12)}$$

$$C_1 = [1+(H_e+H_c)]^{-1},\ H_e = \left(\frac{\partial F}{\partial \boldsymbol{\sigma}}\right)^T \boldsymbol{D}\frac{\partial \psi}{\partial \boldsymbol{\sigma}},\ H_c = -\frac{\partial F}{\partial \varepsilon_q^c} \qquad \textbf{(C.13)}$$

To actually use the above equations a specific function for $\psi$ is needed, which in the current work is $\psi \equiv q$. The gradient of $F$ with respect to $\boldsymbol{\sigma}$ may be expanded as

$$\frac{\partial F}{\partial \boldsymbol{\sigma}} = \frac{\partial F}{\partial q}\frac{\partial q}{\partial \boldsymbol{\sigma}} = \Delta t_i \frac{\partial \dot{\varepsilon}_q^c}{\partial q}\frac{\partial q}{\partial \boldsymbol{\sigma}} \qquad \textbf{(C.14)}$$

An examination of the above equations shows that the gradient of $q$ with respect to $\boldsymbol{\sigma}$ occurs several times. This term is equal to

$$\frac{\partial q}{\partial \boldsymbol{\sigma}} = \frac{3}{2q}[\, s_{xx}\ \ s_{yy}\ \ 2s_{xy}\,]^T \qquad \textbf{(C.15)}$$

Another term that occurs frequently in the finite element equations is termed $\boldsymbol{v}_{ec}$, which for the membrane formulation is defined as

$$\boldsymbol{v}_{ec} = \boldsymbol{D}\frac{\partial q}{\partial \boldsymbol{\sigma}} = \frac{3G}{q}\begin{bmatrix} 2s_{xx}+s_{yy} \\ s_{xx}+2s_{yy} \\ s_{xy} \end{bmatrix} \qquad \textbf{(C.16)}$$

It is now possible to expand $H_e$ and $H_c$. For the membrane formulations they are given by

$$H_e = 3G\Delta t_i \frac{\partial \dot{\varepsilon}_q^c}{\partial q},\quad H_c = \Delta t_i \frac{\partial \dot{\varepsilon}_q^c}{\partial \varepsilon_q^c} \qquad \textbf{(C.17)}$$

With the above expansions the viscoelastic constitutive matrix may be written as

$$\boldsymbol{D}^{ve} = \boldsymbol{D} - C_1 \Delta t_i \frac{\partial \dot{\varepsilon}_q^c}{\partial q}\boldsymbol{v}_{ec}\boldsymbol{v}_{ec}^T \qquad \textbf{(C.18)}$$

with the creep stress increment being given by

$$\Delta\boldsymbol{\sigma}^c = C_1 \Delta t_i \dot{\varepsilon}_q^c \boldsymbol{v}_{ec} \qquad \textbf{(C.19)}$$

To complete the definitions of the above terms the creep strain rate and its derivatives must be specified. For a power law strain hardening form, they are

$$\dot{\varepsilon}_q^c = nA^{\frac{1}{n}} q^{\frac{m}{n}} (\varepsilon_q^c)^{\frac{n-1}{n}}; \quad \frac{\partial \dot{\varepsilon}_q^c}{\partial q} = mA^{\frac{1}{n}} q^{\frac{m-n}{n}} (\varepsilon_q^c)^{\frac{n-1}{n}}; \quad \frac{\partial \dot{\varepsilon}_q^c}{\partial \varepsilon_q^c} = (n-1)A^{\frac{1}{n}} q^{\frac{m}{n}} (\varepsilon_q^c)^{-\frac{1}{n}} \qquad \textbf{(C.20)}$$

where $\varepsilon_q^c = Aq^m t^n$ for a constant stress creep test.

# Appendix D Closed-Form Solution for the Effective Creep Strain Increment

In terms of differentials, the effective creep strain rate (Equation 2.8) may be written as follows:

$$d\varepsilon_q^c = nA^{\frac{1}{n}} q^{\frac{m}{n}} (\varepsilon_q^c)^{\frac{n-1}{n}} dt \tag{D.1}$$

The above equation can be rearranged and integrated over a time step $\Delta t = t_2 - t_1$, where the subscripts 1 and 2 refer to the beginning and the end of the time step, respectively

$$\int_{\varepsilon_{q_1}^c}^{\varepsilon_{q_1}^c + \Delta\varepsilon_q^c} (\varepsilon_q^c)^{\frac{1-n}{n}} d\varepsilon_q^c = \int_{t_1}^{t_1+\Delta t} nA^{\frac{1}{n}} q^{\frac{m}{n}} dt \tag{D.2}$$

where $\Delta\varepsilon_q^c = \varepsilon_{q_2}^c - \varepsilon_{q_1}^c$ is the effective creep strain increment. If the material properties and $q$ are assumed constant over the time step, then the definite integrals can be expanded to

$$n[(\varepsilon_{q_1}^c + \Delta\varepsilon_q^c)^{\frac{1}{n}} - (\varepsilon_{q_1}^c)^{\frac{1}{n}}] = nA^{\frac{1}{n}} q^{\frac{m}{n}} \Delta t \tag{D.3}$$

The above equation can be further rearranged to yield

$$(\varepsilon_{q_1}^c + \Delta\varepsilon_q^c)^{\frac{1}{n}} = (\varepsilon_{q_1}^c)^{\frac{1}{n}} (1 + A^{\frac{1}{n}} q^{\frac{m}{n}} (\varepsilon_{q_1}^c)^{-\frac{1}{n}} \Delta t) \tag{D.4}$$

The effective creep strain increment can be found by taking the $n^{th}$ power of both sides of the previous equation and rearranging terms

$$\Delta\varepsilon_q^c = \varepsilon_{q_1}^c \left( 1 + \frac{nA^{\frac{1}{n}} q^{\frac{m}{n}} (\varepsilon_{q_1}^c)^{\frac{n-1}{n}} \Delta t}{n\varepsilon_{q_1}^c} \right)^n - \varepsilon_{q_1}^c \qquad \textbf{(D.5)}$$

An examination of this equation shows the occurrence of $\dot{\varepsilon}_q^c$ as defined by Equation 2.8. Therefore, the effective creep strain increment can be rewritten in compact form as

$$\Delta\varepsilon_q^c = \varepsilon_{q_1}^c [(n\varepsilon_{q_1}^c)^{-n} (n\varepsilon_{q_1}^c + \dot{\varepsilon}_{q_1}^c \Delta t)^n - 1] \qquad \textbf{(D.6)}$$

# Appendix E The Newton-Raphson Algorithm for Solving for $q$

If Equation 2.8 is substituted into Equation 3.11, then after some rearrangement a nonlinear function $f(q)$ is obtained

$$f(q) = q + 3G\varepsilon_q^c[(n\varepsilon_q^c)^{-n}(n\varepsilon_q^c + nA^{\frac{1}{n}}q^{\frac{m}{n}}(\varepsilon_q^c)^{\frac{n-1}{n}}\Delta t)^n - 1] - q_e = 0 \quad \textbf{(E.1)}$$

The root of the above equation is solved via the Newton-Raphson algorithm

$$q_{i+1} = q_i - \frac{f(q_i)}{f'(q_i)} \quad \textbf{(E.2)}$$

where the derivative $f'(q)$ can be calculated by taking the derivative of Equation E.1 to yield

$$f'(q) = 1 + 3mn^{1-n}GA^{\frac{1}{n}}(\varepsilon_q^c)^{\frac{-n^2+2n-1}{n}}\Delta t q^{\frac{m-n}{n}}[n\varepsilon_q^c + nA^{\frac{1}{n}}q^{\frac{m}{n}}(\varepsilon_q^c)^{\frac{n-1}{n}}\Delta t]^{n-1} \quad \textbf{(E.3)}$$

The initial value for $q_0$ in the root finding scheme is $q_e$ and the iterations are ceased once the following criteria is met:

$$abs\left(\frac{q_{i+1} - q_i}{q_i}\right) \leq Tolerance \quad \textbf{(E.4)}$$

# Appendix F The Average Shape Function Gradients for the Film Element

The finite element equations to determine the displacements for the UL film casting algorithm described in this thesis use average strain elements (Stolle 1992; Stolle *et al*. 2000). This appendix summarizes the derivation of the average shape function gradients for the $d^{\text{th}}$ sub-element, so that Equation 3.23 can be expressed using each sub-element's average $\boldsymbol{B}^d$ matrix. To perform the integration of Equation 3.23, the integral is transformed from the *x*-*y*-*z* to the local *r*-*s*-*t* basis. In the *r*-*s*-*t* system the element is a cube centred at the origin, with each side having a length of 2. The relationship between the *x*-*y*-*z* and the *r*-*s*-*t* systems is expressed using the brick element shape functions ($N_i^b$) via:

$$x = N_i^b x_i; \quad y = N_i^b y_i; \quad z = N_i^b z_i; \quad u = N_i^b u_i; \quad v = N_i^b v_i; \quad w = N_i^b w_i \qquad \textbf{(F.1)}$$

where index notation and the summation convention are assumed and $x_i$, $y_i$, $z_i$, $u_i$, $v_i$ and $w_i$ are the nodal values for the coordinates and displacements. For a brick element, which is illustrated in Figure F.1 in the *x*-*y*-*z* system and in Figure F.2 for the *r*-*s*-*t* system, the shape functions are (Zienkiewicz 1977: p169):

$$N_i^b = \frac{1}{8}(1 + r_i r)(1 + s_i s)(1 + t_i t) \qquad \textbf{(F.2)}$$

where $i$ is the node number, ($r$, $s$, $t$) are the coordinates in the transformed basis and ($r_i$, $s_i$, $t_i$) are the coordinates of the $i^{th}$ node. The summation convention does not apply to this equation.

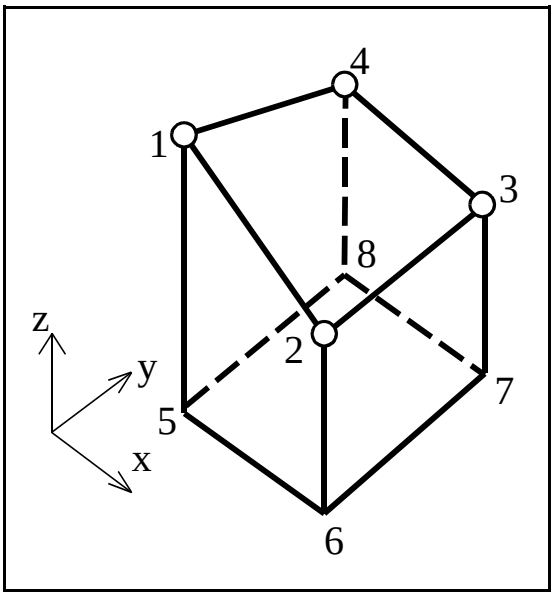


**Figure F.1** A typical brick element in the *x*-*y*-*z* system

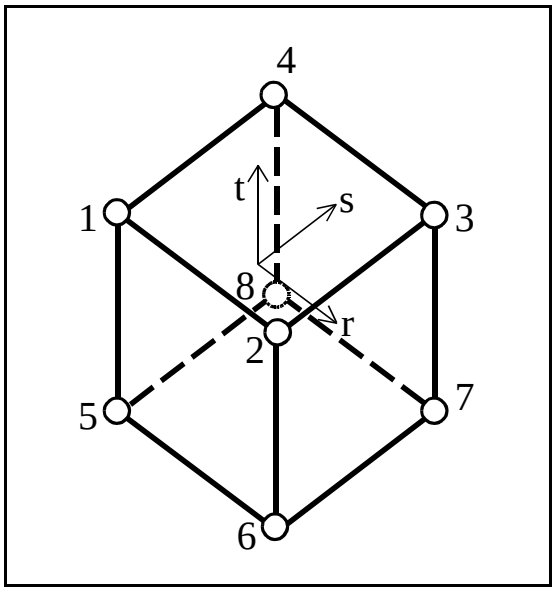


**Figure F.2** A typical brick element in the *s*-*r*-*t* system

In the case of a film element, the above shape functions can be simplified by recognizing that some of the information is redundant. With reference to Figure F.1, it is assumed for the film that for $x$, $y$, $u$ and $v$, the $i^{th}$ nodal value is equal to the $(i+4)^{th}$ nodal value, for $1 \le i \le 4$ and for $z$ and $w$, the $i^{th}$ nodal values are zero, for $5 \le i \le 8$. If these relations are substituted into Equation F.2 then

$$x = N_i x_i ; \quad y = N_i y_i ; \quad z = \bar{t} N_i z_i ; \quad u = N_i u_i ; \quad v = N_i v_i ; \quad w = \bar{t} N_i w_i$$
$$\text{where } N_i = \frac{1}{4}(1+r_i r)(1+s_i s) \text{ and } \bar{t} = \frac{1+t}{2} \qquad \textbf{(F.3)}$$

The shape functions $N_i$, which do not use the summation convention, correspond to the shape functions for a quadrilateral element (Zienkiewicz 1977: p156).

Now that the finite element approximation for *u*, *v* and *w* are available, the average $\boldsymbol{B}^d$ matrix can be expressed in terms of the average shape function gradients:

$$\boldsymbol{B}^d = \begin{bmatrix} N_{1,x}^d & 0 & 0 & N_{2,x}^d & 0 & 0 & N_{3,x}^d & 0 & 0 & N_{4,x}^d & 0 & 0 \\ 0 & N_{1,y}^d & 0 & 0 & N_{2,y}^d & 0 & 0 & N_{3,y}^d & 0 & 0 & N_{4,y}^d & 0 \\ 0 & 0 & (\bar{t}N_1^d)_{,z} & 0 & 0 & (\bar{t}N_2^d)_{,z} & 0 & 0 & (\bar{t}N_3^d)_{,z} & 0 & 0 & (\bar{t}N_4^d)_{,z} \\ N_{1,y}^d & N_{1,x}^d & 0 & N_{2,y}^d & N_{2,x}^d & 0 & N_{3,y}^d & N_{3,x}^d & 0 & N_{4,y}^d & N_{4,x}^d & 0 \\ N_{1,z}^d & 0 & (\bar{t}N_1^d)_{,x} & N_{2,z}^d & 0 & (\bar{t}N_2^d)_{,x} & N_{3,z}^d & 0 & (\bar{t}N_3^d)_{,x} & N_{4,z}^d & 0 & (\bar{t}N_4^d)_{,x} \\ 0 & N_{1,z}^d & (\bar{t}N_1^d)_{,y} & 0 & N_{2,z}^d & (\bar{t}N_2^d)_{,y} & 0 & N_{3,z}^d & (\bar{t}N_3^d)_{,y} & 0 & N_{4,z}^d & (\bar{t}N_4^d)_{,y} \end{bmatrix} \quad \textbf{(F.4)}$$

with a comma used to represent partial differentiation. For the membrane formulation, parasitic shear is suppressed by calculating the gradients associated with the shear terms for the entire element, instead of for each sub-element.

In Equation F.4, the average shape function gradients in the *x*, *y* and *z* directions are needed, both for the quadrilateral shape functions and for the quadrilateral shape functions multiplied by $\bar{t}$. These gradients are calculated by using the Jacobian of transformation ($J_{ij}$), which can be written for a given variable $f = f(x(r,s,t), y(r,s,t), z(r,s,t))$ as follows:

$$\begin{bmatrix} \frac{\partial f}{\partial r} \\ \frac{\partial f}{\partial s} \\ \frac{\partial f}{\partial t} \end{bmatrix} = \begin{bmatrix} \frac{\partial x}{\partial r} & \frac{\partial y}{\partial r} & \frac{\partial z}{\partial r} \\ \frac{\partial x}{\partial s} & \frac{\partial y}{\partial s} & \frac{\partial z}{\partial s} \\ \frac{\partial x}{\partial t} & \frac{\partial y}{\partial t} & \frac{\partial z}{\partial t} \end{bmatrix} \begin{bmatrix} \frac{\partial f}{\partial x} \\ \frac{\partial f}{\partial y} \\ \frac{\partial f}{\partial z} \end{bmatrix} = J_{ij} \begin{bmatrix} \frac{\partial f}{\partial x} \\ \frac{\partial f}{\partial y} \\ \frac{\partial f}{\partial z} \end{bmatrix} \qquad \textbf{(F.5)}$$

Equation F.5 is inverted by using the rule that the inverse of a matrix is equal to the adjoint of the matrix divided by its determinant

$$\begin{bmatrix} \frac{\partial f}{\partial x} \\ \frac{\partial f}{\partial y} \\ \frac{\partial f}{\partial z} \end{bmatrix} = J_{ij}^{-1} \begin{bmatrix} \frac{\partial f}{\partial r} \\ \frac{\partial f}{\partial s} \\ \frac{\partial f}{\partial t} \end{bmatrix} = \frac{1}{\det|J_{ij}|} \begin{bmatrix} M_{11} & -M_{21} & M_{31} \\ -M_{12} & M_{22} & -M_{32} \\ M_{13} & -M_{23} & M_{33} \end{bmatrix} \begin{bmatrix} \frac{\partial f}{\partial r} \\ \frac{\partial f}{\partial s} \\ \frac{\partial f}{\partial t} \end{bmatrix} \qquad \textbf{(F.6)}$$

where $M_{ij}$ are the minors of the $J_{ij}$ and are defined as follows:

$$\begin{aligned} M_{11} &= \begin{vmatrix} y_{,s} & z_{,s} \\ y_{,t} & z_{,t} \end{vmatrix}; \quad M_{12} = \begin{vmatrix} x_{,s} & z_{,s} \\ x_{,t} & z_{,t} \end{vmatrix}; \quad M_{13} = \begin{vmatrix} x_{,s} & y_{,s} \\ x_{,t} & y_{,t} \end{vmatrix}; \\ M_{21} &= \begin{vmatrix} y_{,r} & z_{,r} \\ y_{,t} & z_{,t} \end{vmatrix}; \quad M_{22} = \begin{vmatrix} x_{,r} & z_{,r} \\ x_{,t} & z_{,t} \end{vmatrix}; \quad M_{23} = \begin{vmatrix} x_{,r} & y_{,r} \\ x_{,t} & y_{,t} \end{vmatrix}; \\ M_{31} &= \begin{vmatrix} y_{,r} & z_{,r} \\ y_{,s} & z_{,s} \end{vmatrix}; \quad M_{32} = \begin{vmatrix} x_{,r} & z_{,r} \\ x_{,s} & z_{,s} \end{vmatrix}; \quad M_{33} = \begin{vmatrix} x_{,r} & y_{,r} \\ x_{,s} & y_{,s} \end{vmatrix} \end{aligned} \qquad \textbf{(F.7)}$$

Using Equation F.6, Equation 3.23 is transformed to the *r*-*s*-*t* basis:

$$\Delta\varepsilon^d = \begin{bmatrix} \Delta\varepsilon_{xx}^d \\ \Delta\varepsilon_{yy}^d \\ \Delta\varepsilon_{zz}^d \\ \Delta\gamma_{xy}^d \\ \Delta\gamma_{xz}^d \\ \Delta\gamma_{yz}^d \end{bmatrix} = \frac{1}{V^d} \int_{r_l^d}^{r_u^d} \int_{s_l^d}^{s_u^d} \int_{t_l^d}^{t_u^d} \begin{bmatrix} M_{11}u,r - M_{21}u,s + M_{31}u,t \\ -M_{12}v,r + M_{22}v,s - M_{32}v,t \\ M_{13}w,r - M_{23}w,s + M_{33}w,t \\ -M_{12}u,r + M_{22}u,s - M_{32}u,t \; + \; M_{11}v,r - M_{21}v,s + M_{31}v,t \\ M_{13}u,r - M_{23}u,s + M_{33}u,t \; + \; M_{11}w,r - M_{21}w,s + M_{31}w,t \\ M_{13}v,r - M_{23}v,s + M_{33}v,t \; - \; M_{12}w,r + M_{22}w,s - M_{32}w,t \end{bmatrix} drdsdt \quad \textbf{(F.8)}$$

One should note that the determinant of the Jacobian cancels out of the above equation. The values of the integration limits for each sub-element, and for the entire element, are summarized in Table F.1.

**Table F.1 Integration Limits to Define each of the Sub-Elements and the Entire Element**

| Sub-element $d$ | $r_l^d$ | $r_u^d$ | $s_l^d$ | $s_u^d$ | $t_l^d$ | $t_u^d$ |
|---|---|---|---|---|---|---|
| 1 | -1 | 0 | -1 | 0 | -1 | 1 |
| 2 | 0 | 1 | -1 | 0 | -1 | 1 |
| 3 | 0 | 1 | 0 | 1 | -1 | 1 |
| 4 | -1 | 0 | 0 | 1 | -1 | 1 |
| entire element | -1 | 1 | -1 | 1 | -1 | 1 |

The minors in terms of the finite element discretizations are given by

$$\begin{aligned}
M_{11} &= y_{,s}z_{,t} - y_{,t}z_{,s} = \tfrac{1}{2}N_{i,s}N_j y_i z_j \\
M_{12} &= x_{,s}z_{,t} - x_{,t}z_{,s} = \tfrac{1}{2}N_{i,s}N_j x_i z_j \\
M_{13} &= x_{,s}y_{,t} - x_{,t}y_{,s} = 0 \\
M_{21} &= y_{,r}z_{,t} - y_{,t}z_{,r} = \tfrac{1}{2}N_{i,r}N_j y_i z_j \\
M_{22} &= x_{,r}z_{,t} - x_{,t}z_{,r} = \tfrac{1}{2}N_{i,r}N_j x_i z_j \\
M_{23} &= x_{,r}y_{,t} - x_{,t}y_{,r} = 0 \\
M_{31} &= y_{,r}z_{,s} - y_{,s}z_{,r} = \bar{t}\,(N_{i,r}N_{j,s} - N_{i,s}N_{j,r})\, y_i z_j \\
M_{32} &= x_{,r}z_{,s} - x_{,s}z_{,r} = \bar{t}\,(N_{i,r}N_{j,s} - N_{i,s}N_{j,r})\, x_i z_j \\
M_{33} &= x_{,r}y_{,s} - x_{,s}y_{,r} = (N_{i,r}N_{j,s} - N_{i,s}N_{j,r})\, x_i y_j
\end{aligned} \qquad \textbf{(F.9)}$$

The above expansion of the minors takes advantage of the fact that $x_{,t} = y_{,t} = 0$.

The minors can be substituted into Equation F.8, along with the displacement gradients in the *r-s-t* basis (with $u_{,t} = v_{,t} = 0$) to yield

$$\Delta\varepsilon^d = \frac{1}{2V^d}\int_{r_l^d}^{r_u^d}\int_{s_l^d}^{s_n^d}\int_{t_l^d}^{t_u^d} \begin{bmatrix}
N_k(N_{i,r}N_{j,s} - N_{i,s}N_{j,r})\, u_i y_j z_k \\
-N_k(N_{i,r}N_{j,s} - N_{i,s}N_{j,r})\, v_i y_j z_k \\
N_k(N_{i,r}N_{j,s} - N_{i,s}N_{j,r})\, x_i y_j w_k \\
-N_k(N_{i,r}N_{j,s} - N_{i,s}N_{j,r})\, u_i x_j z_k + N_k(N_{i,r}N_{j,s} - N_{i,s}N_{j,r})\, v_i y_j z_k \\
\bar{t}(N_k(N_{i,r}N_{j,s} - N_{i,s}N_{j,r})\, w_i x_j z_k + N_k(N_{i,r}N_{j,s} - N_{i,s}N_{j,r})\, y_i z_j w_k) \\
\bar{t}(-N_k(N_{i,r}N_{j,s} - N_{i,s}N_{j,r})\, w_i x_j z_k - N_k(N_{i,r}N_{j,s} - N_{i,s}N_{j,r})\, x_i z_j w_k)
\end{bmatrix} dr\,ds\,dt \qquad \textbf{(F.10)}$$

A common expression appears in this calculation, which motivates the following definition:

$$I_{ijk} \equiv N_k\,(N_{i,r}N_{j,s} - N_{i,s}N_{j,r}) \qquad \textbf{(F.11)}$$

Using the definition of $I_{ijk}$ and integrating Equation F.10 over t ($t_l$ = -1, $t_u$ = 1 for all $d$), the following equation is found:

$$\Delta\varepsilon^d = \begin{bmatrix} \Delta\varepsilon_{xx}^d \\ \Delta\varepsilon_{yy}^d \\ \Delta\varepsilon_{zz}^d \\ \Delta\gamma_{xy}^d \\ \Delta\gamma_{xz}^d \\ \Delta\gamma_{yz}^d \end{bmatrix} = \frac{1}{V^d} \int_{r_l^d}^{r_u^d} \int_{s_l^d}^{s_n^d} \begin{bmatrix} I_{ijk} u_i y_j z_k \\ -I_{ijk} v_i x_j z_k \\ I_{ijk} x_i y_j w_k \\ -I_{ijk} u_i x_j z_k + I_{ijk} v_i y_j z_k \\ \frac{1}{2}[I_{ijk} w_i y_j z_k + I_{ijk} y_i z_j w_k] \\ -\frac{1}{2}[I_{ijk} w_i x_j z_k + I_{ijk} x_i z_j w_k] \end{bmatrix} dr\,ds \qquad \textbf{(F.12)}$$

This equation shows that the expression $I_{ijk}$ contains the terms that depend only on $r$ and $s$, which suggests the following definition:

$$A_{ijk}^d = \int_{r_l^d}^{r_u^d} \int_{s_l^d}^{s_n^d} I_{ijk}\, dr\, ds \qquad \textbf{(F.13)}$$

Using Equation F.13, Equation F.12 can be expressed as:

$$\Delta\varepsilon^d = \begin{bmatrix} \Delta\varepsilon_{xx}^d \\ \Delta\varepsilon_{yy}^d \\ \Delta\varepsilon_{zz}^d \\ \Delta\gamma_{xy}^d \\ \Delta\gamma_{xz}^d \\ \Delta\gamma_{yz}^d \end{bmatrix} = \frac{1}{V^d} \begin{bmatrix} A_{ijk} y_j z_k u_i \\ -A_{ijk} x_j z_k v_i \\ A_{jki} x_j z_k w_i \\ -A_{ijk} x_j z_k u_i + A_{ijk} y_j z_k v_i \\ \frac{1}{2}(A_{ijk} y_j z_k + A_{jki} y_j z_k) w_i \\ -\frac{1}{2}(A_{ijk} x_j z_k + A_{jki} x_j z_k) w_i \end{bmatrix} \qquad \textbf{(F.14)}$$

From Equation F.14 the average shape function gradients can be expressed as

$$\begin{bmatrix} N_{i,x}^{d} \\ N_{i,y}^{d} \\ N_{i,z}^{d} \\ (\bar{t}N_i)_{,x}^{d} \\ (\bar{t}N_i)_{,y}^{d} \\ (\bar{t}N_i)_{,z}^{d} \end{bmatrix} = \frac{1}{V^d} \begin{bmatrix} A_{ijk}^{d} y_j z_k \\ -A_{ijk}^{d} x_j z_k \\ 0 \\ \frac{1}{2}(A_{ijk}^{d} + A_{jki}^{d}) y_j z_k \\ -\frac{1}{2}(A_{ijk}^{d} + A_{jki}^{d}) x_j z_k \\ A_{jki}^{d} x_j y_k \end{bmatrix} \quad \textbf{(F.15)}$$

Equation F.15 shows that the average shape function gradients for the $d^{\text{th}}$ sub-element can be determined using the element's nodal coordinates and the $A_{ijk}^{d}$ expression. An examination of Equation F.13 shows that the calculation of $A_{ijk}^{d}$ only depends on integration in *r*-*s* space; therefore, the integration can be performed once and the results can be reused throughout the analysis. $A_{ijk}^{d}$ was evaluated using Maple and, after some rearranging, $A_{ijk}^{d}$ can be expressed as follows:

$$A_{ijk}^{d} = \frac{g(d)}{64}\left[\alpha + \frac{1}{3}(r_k\beta + s_k\gamma) + \frac{1}{2}(r_k\alpha + \beta + \frac{1}{3}r_k s_k\gamma)\bar{r} + \frac{1}{2}(s_k\alpha + \frac{1}{3}r_k s_k\beta + \gamma)\bar{s} + \frac{1}{4}(r_k s_k\alpha + s_k\beta + r_k\gamma)\overline{rs}\right] \quad \textbf{(F.16)}$$

*where* $\alpha = r_i s_j - r_j s_i$; $\beta = r_i r_j (s_j - s_i)$; *and* $\gamma = s_i s_j (r_i - r_j)$

In Equation F.16 the summation convention does not apply, $r_i$ = [-1 1 1 -1], $s_i$ = [-1, -1, 1, 1], and the remaining terms are summarized in Table F.2.

**Table F.2 Terms used for the Calculation of $A_{ijk}^{\ d}$**

| Sub-element $d$ | $g(d)$ | $\bar{r}$ | $\bar{s}$ |
|---|---|---|---|
| 1 | 1 | -1 | -1 |
| 2 | 1 | 1 | -1 |
| 3 | 1 | 1 | 1 |
| 4 | 1 | -1 | 1 |
| entire element | 4 | 0 | 0 |

The volume calculation can also be done using $A_{ijk}^{\ d}$, as follows:

$$V^d = \int_{V^d} dxdydz = \int_{r_l^d}^{r_u^d}\int_{s_l^d}^{s_u^d}\int_{t_l^d}^{t_u^d} \det|J_{ij}|drdsdt = \int_{r_l^d}^{r_u^d}\int_{s_l^d}^{s_u^d} I_{ijk}\, x_i\, y_j\, z_k\, dr\, ds = A_{ijk}^{\ d}\, x_i\, y_j\, z_k \qquad \textbf{(F.17)}$$

This appendix has shown how the entries in $\boldsymbol{B}^d$ are calculated. These entries can be used to construct the $\boldsymbol{B}$ matrix used to calculate the in-plane incremental displacements and the $\boldsymbol{B}_{zz}$ matrix used to calculate the out-of-plane incremental displacements. The $\boldsymbol{B}$ matrix uses the $N_{i,x}^{\ d}$ and $N_{i,y}^{\ d}$ terms and the $\boldsymbol{B}_{zz}$ matrix uses the $(\bar{t}N_i)_{,x}^{\ d}$ terms.

# Appendix G The Closed-Form Solution for 1D Isothermal Film Casting of a Power-Law Fluid

The governing equations for 1D isothermal film casting of a power-law fluid in an Eulerian formulation are as follows:

$$\frac{d(h\sigma_{xx})}{dx} = 0 \qquad \textbf{(G.1)}$$

$$\frac{d(h\dot{u})}{dx} = 0 \qquad \textbf{(G.2)}$$

$$\sigma_{xx} = 2^{\beta+1}K\left(\frac{d\dot{u}}{dx}\right)^{\beta} \qquad \textbf{(G.3)}$$

Equations G.1 and G.2 are the 1D versions of Equations 8.1 and 8.2, respectively. The constitutive equation, Equation G.3, is found using Equation 4.1 along with $\sigma_{xx} = -p + \tau_{xx}$, $\sigma_{zz} = -p + \tau_{zz} = 0$ (membrane approximation), $\frac{\partial \dot{u}}{\partial x} = -\frac{\partial \dot{w}}{\partial z}$ (incompressibility constraint) and $\dot{II} = 2\frac{\partial \dot{u}}{\partial x}$. The boundary conditions for the 1D film casting problem are

$$\begin{aligned} &At\ x = 0 \qquad \dot{u} = \dot{u}_{die}\ and\ h = h_{die} \\ &At\ x = L \qquad \dot{u} = \dot{u}_{roll} = \dot{u}_{die}\,Dr \end{aligned} \qquad \textbf{(G.4)}$$

Integration of Equations G.1 and G.2 yields

$$h\sigma_{xx} = F \qquad \textbf{(G.5)}$$

and

$$h\dot{u} = Q \qquad \textbf{(G.6)}$$

where $F$ represents the force per unit width and $Q$ is the volume flux per unit width. Now Equation G.3 and Equation G.6 (rearranged to explicitly calculate $h$) are substituted into Equation G.5 and rearranged as follows:

$$\begin{aligned} 2^{\beta+1}K\frac{Q}{\dot{u}}\left(\frac{d\dot{u}}{dx}\right)^{\beta} &= F \\ \dot{u}^{-\frac{1}{\beta}}\frac{d\dot{u}}{dx} &= \left(\frac{F}{2^{\beta+1}KQ}\right)^{\frac{1}{\beta}} = C_1 \\ \dot{u}^{-\frac{1}{\beta}}du &= C_1 dx \end{aligned} \qquad \textbf{(G.7)}$$

Now both sides of the resulting equation are integrated:

$$\begin{aligned} \int_{\dot{u}_{die}}^{\dot{u}} \hat{u}^{-\frac{1}{\beta}} d\hat{u} &= \int_0^x C_1 d\hat{x} \\ \frac{\beta}{\beta-1}(\dot{u}^{\frac{\beta-1}{\beta}} - \dot{u}_{die}^{\frac{\beta-1}{\beta}}) &= C_1 x \\ \dot{u}^{\frac{\beta-1}{\beta}} - \dot{u}_{die}^{\frac{\beta-1}{\beta}} &= \frac{\beta-1}{\beta}C_1 x = C_2 x \end{aligned} \qquad \textbf{(G.8)}$$

Applying the boundary condition for velocity at $x = L$, the theoretical velocity profile is found to be

$$\dot{u} = \dot{u}_{die}\left[1 + (Dr^{\frac{\beta-1}{\beta}} - 1)\frac{x}{L}\right]^{\frac{\beta}{\beta-1}} \qquad \textbf{(G.9)}$$

Substituting this result into Equation G.6 and using $Q = u_{die} \cdot h_{die}$, the theoretical thickness profile is found to be

$$h = h_{die}\left[1 + (Dr^{\frac{\beta-1}{\beta}} - 1)\frac{x}{L}\right]^{\frac{-\beta}{\beta-1}} \qquad \textbf{(G.10)}$$

The gradients of velocity and thickness can be found by differentiating Equations G.9 and G.10, respectively

$$\frac{d\dot{u}}{dx} = \frac{\beta \dot{u}_{die}}{(\beta-1)L}(Dr^{\frac{\beta-1}{\beta}}-1)\left[1 + (Dr^{\frac{\beta-1}{\beta}}-1)\frac{x}{L}\right]^{\frac{1}{\beta-1}} \quad \textbf{(G.11)}$$

$$\frac{dh}{dx} = \frac{-\beta h_{die}}{(\beta-1)L}(Dr^{\frac{\beta-1}{\beta}}-1)\left[1 + (Dr^{\frac{\beta-1}{\beta}}-1)\frac{x}{L}\right]^{\frac{1-2\beta}{\beta-1}} \quad \textbf{(G.12)}$$

Using Equations G.3 and G.11, the stress in the machine direction can be expressed as

$$\sigma_{xx} = 2^{\beta+1}K\left[\frac{\beta \dot{u}_{die}}{(\beta-1)L}(Dr^{\frac{\beta-1}{\beta}}-1)\left[1 + (Dr^{\frac{\beta-1}{\beta}}-1)\frac{x}{L}\right]^{\frac{1}{\beta-1}}\right]^{\beta} \quad \textbf{(G.13)}$$

Another quantity of interest is the rate of energy dissipation over the domain $\dot{W}^c$. For the 1D domain this quantity may be expressed as follows:

$$\dot{W}^c = \iiint_V \sigma_{ij} D_{ij} dV = \iiint_V \sigma_{xx} D_{xx} dV = \int_0^L h(x)\sigma_{xx}(x)\frac{d\dot{u}}{dx}dx \quad \textbf{(G.14)}$$

where $\dot{W}^c$ is the steady state rate of energy dissipation per unit width of the film. If Equations G.10, G.13 and G.11 are substituted into Equation G.14, the energy dissipated can be expressed as

$$\dot{W}^c = 2^{\beta+1}Kh_{die}\dot{u}_{die}^{\beta+1}(Dr-1)\left[\frac{\beta(Dr^{\frac{\beta-1}{\beta}}-1)}{(\beta-1)L}\right]^{\beta} \quad \textbf{(G.15)}$$

A special case of the power law fluid is the linear viscous fluid, where $\beta = 1$. The above equations for velocity, thickness, stress and energy dissipation are undefined for

$\beta = 1$; however, the solutions for these variables can be derived in an analogous manner to the above derivation. If the above steps are repeated for the Newtonian fluid, then the following results are found:

$$\dot{u} = \dot{u}_{die} Dr^{\frac{x}{L}} \tag{G.16}$$

$$h = h_{die} Dr^{-\frac{x}{L}} \tag{G.17}$$

$$\frac{dh}{dx} = -\frac{h_{die}}{L}\ln(Dr) Dr^{-\frac{x}{L}} \tag{G.18}$$

$$\sigma_{xx} = 4\eta^s \frac{\dot{u}_{die}}{L}\ln(Dr) Dr^{\frac{x}{L}} \tag{G.19}$$

$$\dot{W}^c = 4\eta^s h_{die} \dot{u}_{die}^2 \ln(Dr)(Dr-1)/L \tag{G.20}$$

# Appendix H Relating UL to E Constitutive Parameters for the Power-Law and Linear Maxwell Fluids

The constitutive equation presented in Section 2.5, which is expressed in a UL framework, can be related to two constitutive models commonly employed within an E framework: the power-law fluid, and the linear Maxwell fluid.

## The Power-Law Fluid

In the E framework most often used in fluid mechanics, the power-law constitutive equation can be written as

$$\tau_{ij} = 2K\dot{I}I^{\beta-1}D_{ij}, \quad \dot{I}I = \sqrt{2D_{ij}D_{ij}} \qquad \textbf{(H.1)}$$

where $\tau_{ij}$ is termed the extra stress tensor, $D_{ij}$ is the rate of deformation tensor, $K$ is a constant, and $\dot{I}I$ is proportional to the second invariant of the rate of deformation tensor.

If there is no strain hardening (i.e. $n$ = 1.0), then the creep strain rate tensor introduced in Section 2.5 can be written, using index notation, as

$$\dot{\varepsilon}_{ij} = \dot{\varepsilon}_q \frac{\partial \psi}{\partial \sigma_{ij}} = Aq^m \left( \frac{3}{2q} s_{ij} \right) = \frac{3Aq^{m-1}}{2} s_{ij} \qquad \textbf{(H.2)}$$

Equations H.1 and H.2 can be related by taking the following into account:

i) the extra-stress tensor has the same definition as the deviatoric stress tensor ($\tau_{ij} = s_{ij}$);

ii) for viscous materials (low relaxation times) the elastic strain rate is small, so that $\dot{\varepsilon}_{ij}$ is approximately equal to $\dot{\varepsilon}^c_{ij}$; and,

iii) for small displacement gradient components, $\dot{\varepsilon}_{ij}$ is approximately equal to $D_{ij}$ (Malvern 1969: p162).

Using the above statements, Equation H.1 can be written as

$$s_{ij} = 2K\dot{II}^{\beta-1}\dot{\varepsilon}_{ij} \qquad \textbf{(H.3)}$$

and Equation H.2 can be written as

$$\dot{\varepsilon}_{ij} = \frac{3Aq^{m-1}}{2}s_{ij} \qquad \textbf{(H.4)}$$

Equation H.3 includes an invariant of the strain rate tensor, while Equation H.4 contains an invariant of the deviatoric stress tensor. To relate the two equations it is necessary to relate the invariants. This is done through the constitutive relationship for the UL description

$$q = \left(\frac{\dot{\varepsilon}_q}{A}\right)^{\frac{1}{m}} \qquad \textbf{(H.5)}$$

Equation H.5 is only valid in the case of viscous flows, when the stress can be assumed to only depend on the current rate of strain; that is, when the stress is independent of the previous deformation history. If Equation H.5 is substituted into Equation H.4 and the strain rate is isolated in Equation H.3, then the two forms of the constitutive equation can be equated, which after rearranging yields

$$3A^{\frac{1}{m}}\dot{\varepsilon}_q^{\frac{m-1}{m}} = K^{-1}\dot{II}^{1-\beta} \qquad \textbf{(H.6)}$$

To further relate the two expressions, the strain rate invariants can be introduced into the above, so that after rearranging

$$\left[\left(3^{m+1}2^{m-1}\right)^{\frac{1}{2}}A\right]^{\frac{1}{m}}(\dot{\varepsilon}_{ij}\dot{\varepsilon}_{ij})^{\frac{m-1}{2m}} = K^{-1}2^{\frac{1-\beta}{2}}(\dot{\varepsilon}_{ij}\dot{\varepsilon}_{ij})^{\frac{1-\beta}{2}} \quad \textbf{(H.7)}$$

If the powers of $\dot{\varepsilon}_{ij}\dot{\varepsilon}_{ij}$ for both sides of Equation H.7 are equated, then the following result is found:

$$m = \frac{1}{\beta} \quad \textbf{(H.8)}$$

Similarly, if the constants for both sides of Equation H.7 are equated, then the following relation holds:

$$A = 3^{\frac{-\beta-1}{2\beta}}K^{\frac{-1}{\beta}} \quad \textbf{(H.9)}$$

Equations H.8 and H.9 relate the parameters commonly available in the chemical engineering literature ($\beta$ and $K$) to the UL constitutive parameters adopted in this thesis ($m$ and $A$).

A special case of the power-law fluid is the Newtonian fluid, which is obtained when $\beta = 1$. In this case Equations H.8 and H.9 simplify to $m = 1$ and $A = 1/(3K)$. To further highlight the Newtonian fluid, two new symbols are introduced: $\eta^s$ and $\eta^c$, which are termed the shear and creep viscosities, respectively. These viscosities are related to $K$ and $A$, and to each other via

$$K = \eta^s \;, \quad A = \frac{1}{2\eta^c} \;, \quad \textit{and} \;\; \eta^c = \frac{3}{2}\eta^s \quad \textbf{(H.10)}$$

**The Linear Maxwell Fluid**

In the chemical engineering literature the linear Maxwell fluid is written as (Joseph 1990: p6)

$$\tau_{ij} + \lambda\dot{\tau}_{ij} = 2\eta^s D_{ij}, \quad \lambda = \frac{n^s}{G} \qquad \textbf{(H.11)}$$

In the UL constitutive equation, with $m = n = 1$, the rate of change of the deviatoric stress is written as follows:

$$\dot{s}_{ij} = 2G\dot{\varepsilon}^e_{ij} = 2G(\dot{\varepsilon}_{ij} - \dot{\varepsilon}^c_{ij}) = 2G(\dot{\varepsilon}_{ij} - \frac{3}{4\eta^c}s_{ij}) \qquad \textbf{(H.12)}$$

The above equation can be rearranged and simplified to

$$s_{ij} + \frac{2\eta^c}{3G}\dot{s}_{ij} = \frac{4\eta^c}{3}\dot{\varepsilon}_{ij} \qquad \textbf{(H.13)}$$

If the statements i) and iii) from above are used, along with Equation H.10, then Equations H.11 and H.13 are shown to be identical. Therefore, several alternative definitions for the relaxation time are as follows:

$$\lambda = \frac{\eta^s}{G} = \frac{2\eta^c}{3G} = \frac{1}{3GA} = \frac{1}{EA} \qquad \textbf{(H.14)}$$

The above equation uses the relationship between the elastic and shear moduli for an incompressible material; that is, $E = 3G$.

# Appendix I The UCM Solutions for Constant Rates of Uniaxial and Equibiaxial Extension

This appendix summarizes the closed-form solutions for stress as a function of time for a UCM material under a constant rate of natural strain for two material tests: uniaxial extension and equibiaxial extension. The two tests are shown in Table I.1.

**Table I.1 Summary of the Uniaxial and Equibiaxial Material Tests**

| | **Uniaxial Extension** | **Equibiaxial Extension** |
|---|---|---|
| **Figure of Material Test** | 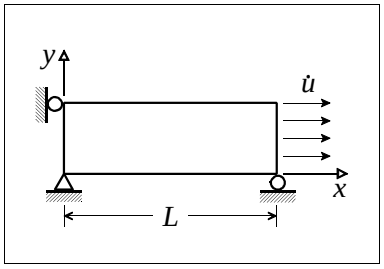 | 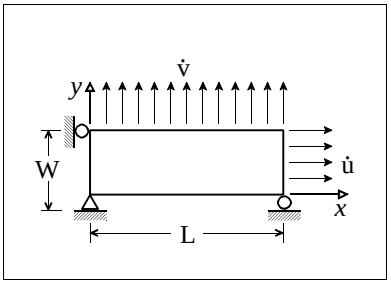 |
| **Strain Rate Assumption** | $\dot{\varepsilon}_{xx} = \dfrac{\partial \dot{u}}{\partial x} = \dot{\varepsilon}$ | $\dot{\varepsilon}_{xx} = \dfrac{\partial \dot{u}}{\partial x} = \dot{\varepsilon}_{yy} = \dfrac{\partial \dot{v}}{\partial y} = \dot{\varepsilon}$ |
| **Velocities** | $\dot{u} = \dot{\varepsilon} L_0 e^{\dot{\varepsilon} t}$ | $\dot{u} = \dot{\varepsilon} L_0 e^{\dot{\varepsilon} t}$ ; $\dot{v} = \dot{\varepsilon} W_0 e^{\dot{\varepsilon} t}$ |
| **Incompressibility and Symmetry** | $\dfrac{\partial \dot{v}}{\partial y} = \dfrac{\partial \dot{w}}{\partial z} = -\dfrac{1}{2}\dfrac{\partial \dot{u}}{\partial x} = -\dfrac{1}{2}\dot{\varepsilon}$ | $\dfrac{\partial \dot{w}}{\partial z} = -\left(\dfrac{\partial \dot{u}}{\partial x} + \dfrac{\partial \dot{v}}{\partial y}\right) = -2\dot{\varepsilon}$ |

The first row of Table I.1 summarizes the material tests by showing the dimensions, boundary conditions and coordinate system, for which the *z*-axis is directed out of the page. Table I.1 also shows the constant natural strain rate assumptions for each test and the

velocities ($\dot{u}$, $\dot{v}$) necessary to maintain the constant strain rate ($\dot{\varepsilon}$), as a function of time ($t$) and the initial length ($L_0$) and width ($W_0$). The final row of Table I.1 uses the assumed incompressibility of the material to express the strain rates in the directions where the velocity is not controlled. In the case of the uniaxial extension test, use is also made of the fact that the strain rates in the *y* and *z* directions should be equal, as neither direction should strain preferentially.

The equation for $\dot{u}$ in the third row of Table I.1 is found by using the fact that the strain rate is constant. For a constant rate of natural strain ($\dot{\varepsilon}$) the natural strain ($\varepsilon$) can be determined by integration; that is, $\varepsilon = \dot{\varepsilon}t$. The length ($L$) as a function of time can be determined using the definition of natural strain, as follows:

$$\varepsilon = \ln\left(\frac{L}{L_0}\right) = \dot{\varepsilon}t, \qquad \therefore\ L = L_0 e^{\dot{\varepsilon}t} \tag{I.1}$$

where the exponential function has been applied to each side of the equation to remove the natural logarithm. Equation I.1 can be used to determine the variation of $\dot{u}$ required to keep the extension rate constant

$$\dot{u} = \frac{dL}{dt} = \dot{\varepsilon}L_0 e^{\dot{\varepsilon}t} \tag{I.2}$$

An analogous approach is used to determine $\dot{v}$ for the equibiaxial extension test.

Now that the kinematics of the material tests have been summarized, the discussion can move to the description of the upper convected maxwell fluid (UCM), for which the extra-stress relation can be written as

$$\lambda\overset{\nabla}{\tau}_{ij} + \tau_{ij} = 2\eta^{s}D_{ij} \qquad \textbf{(I.3)}$$

with the upper convected derivative defined as

$$\overset{\nabla}{\tau}_{ij} = \frac{D\tau_{ij}}{Dt} - L_{ik}\tau_{kj} - \tau_{ik}L_{jk} \qquad \textbf{(I.4)}$$

where $L_{ij}$ is the velocity gradient tensor and $D/Dt$ is the material derivative, which simplifies to $d/dt$ for the current problems, as the stress is uniform throughout the body and consequently there is no advection of stress.

For both the uniaxial and biaxial cases there is no shearing; therefore, the velocity gradient, rate of deformation and extra-stress tensors can be written as

$$L_{ij} = D_{ij} = \begin{bmatrix} \dot{\varepsilon}_{xx} & 0 & 0 \\ 0 & \dot{\varepsilon}_{yy} & 0 \\ 0 & 0 & \dot{\varepsilon}_{zz} \end{bmatrix}; \qquad \tau_{ij} = \begin{bmatrix} \tau_{xx} & 0 & 0 \\ 0 & \tau_{yy} & 0 \\ 0 & 0 & \tau_{zz} \end{bmatrix} \qquad \textbf{(I.5)}$$

In this equation the rate of deformation is related to the rate of change of the natural strain. To prove that this is possible, one can consider the following relation from Malvern (1969: p162):

$$\frac{DE_{ij}}{Dt} = F_{mi}D_{mn}F_{nj} \qquad \textbf{(I.6)}$$

which relates the Green's finite strain $E_{ij}$ to the material deformation gradient $F_{ij}$ and the rate of deformation tensor $D_{ij}$. For the simple uniaxial extension problem, the terms in this equation can be expanded, rearranged and interpreted in terms of the natural strain, to obtain Equation I.5.

Using the $L_{ij}$ and $D_{ij}$ tensors and the definition of the upper convected derivative, the *x*-component of the extra-stress tensor in Equation I.3 can be written as

$$\lambda\left(\frac{d\tau_{xx}}{dt} - 2\dot{\varepsilon}_{xx}\tau_{xx}\right) + \tau_{xx} = 2\eta^s\dot{\varepsilon}_{xx} \qquad \textbf{(I.7)}$$

This linear nonhomogeneous differential equation, which has constant coefficients, can be solved using the initial condition that $\tau_{xx} = 0$ to yield

$$\tau_{xx} = \frac{2\eta^s\dot{\varepsilon}_{xx}}{1 - 2\lambda\dot{\varepsilon}_{xx}}\left(1 - e^{(2\dot{\varepsilon}_{xx}-\frac{1}{\lambda})t}\right) = \frac{2\eta^s\dot{\varepsilon}}{1 - 2\lambda\dot{\varepsilon}}\left(1 - e^{(2\dot{\varepsilon}-\frac{1}{\lambda})t}\right) \qquad \textbf{(I.8)}$$

where the symbol for the constant strain rate ($\dot{\varepsilon}$) has been substituted in for the strain rate in the *x*-direction. Similarly, the other two extra-stress values in Equation I.3 can be solved

$$\tau_{yy} = \frac{2\eta^s\dot{\varepsilon}_{yy}}{1 - 2\lambda\dot{\varepsilon}_{yy}}\left(1 - e^{(2\dot{\varepsilon}_{yy}-\frac{1}{\lambda})t}\right) \qquad \textbf{(I.9)}$$

$$\tau_{zz} = \frac{2\eta^s\dot{\varepsilon}_{zz}}{1 - 2\lambda\dot{\varepsilon}_{zz}}\left(1 - e^{(2\dot{\varepsilon}_{zz}-\frac{1}{\lambda})t}\right) \qquad \textbf{(I.10)}$$

For the uniaxial extension $\dot{\varepsilon}_{yy} = -\frac{1}{2}\dot{\varepsilon}$. If this relation is substituted into Equation I.9, then the following results

$$\tau_{yy} = \frac{-\eta^s\dot{\varepsilon}}{1 + \lambda\dot{\varepsilon}}\left(1 - e^{(-\dot{\varepsilon}-\frac{1}{\lambda})t}\right) \qquad \textbf{(I.11)}$$

As there is no resistance to deformation in the *y*-direction, the stress $\sigma_{yy}$ in that direction is zero; therefore, from the definition of the extra-stress tensor $p = \tau_{yy}$ and $\sigma_{xx} = \tau_{xx} - p = \tau_{xx} - \tau_{yy}$.

Using this final relation and the previously derived values for the extra-stress components, the stress in the *x*-direction may then be written as

$$\sigma_{xx} = \frac{2\eta^s\dot{\varepsilon}}{1 - 2\lambda\dot{\varepsilon}}\left(1 - e^{(2\dot{\varepsilon}-\frac{1}{\lambda})t}\right) + \frac{\eta^s\dot{\varepsilon}}{1 + \lambda\dot{\varepsilon}}\left(1 - e^{(-\dot{\varepsilon}-\frac{1}{\lambda})t}\right) \qquad \textbf{(I.12)}$$

which can be rearranged to yield

$$\sigma_{xx} = \frac{\eta^s\dot{\varepsilon}}{2(\lambda\dot{\varepsilon})^2 + \lambda\dot{\varepsilon} - 1}\left(2(\lambda\dot{\varepsilon}+1)e^{(2\dot{\varepsilon}-\frac{1}{\lambda})t} - (2\lambda\dot{\varepsilon}-1)e^{(-\dot{\varepsilon}-\frac{1}{\lambda})t} - 3\right) \qquad \textbf{(I.13)}$$

The stress for the equibiaxial case can be derived in an analogous manner to that for the uniaxial case. First, the relations $\dot{\varepsilon}_{xx} = \dot{\varepsilon}_{yy} = \dot{\varepsilon}$ and $\dot{\varepsilon}_{zz} = -2\dot{\varepsilon}$ are substituted into Equations I.8, I.9 and I.10. Second, the equation $\sigma_{zz} = 0$ is used to find $\sigma_{xx} = \tau_{xx} - \tau_{zz}$. Third, the first two steps are combined, to yield

$$\sigma_{xx} = \frac{2\eta^s\dot{\varepsilon}}{1 - 2\lambda\dot{\varepsilon}}\left(1 - e^{(2\dot{\varepsilon}-\frac{1}{\lambda})t}\right) + \frac{4\eta^s\dot{\varepsilon}}{1 + 4\lambda\dot{\varepsilon}}\left(1 - e^{(-4\dot{\varepsilon}-\frac{1}{\lambda})t}\right) \qquad \textbf{(I.14)}$$

which can be rearranged and written as

$$\sigma_{xx} = \frac{2\eta^s\dot{\varepsilon}}{8(\lambda\dot{\varepsilon})^2 - 2\lambda\dot{\varepsilon} - 1}\left((1 + 4\lambda\dot{\varepsilon})e^{(2\dot{\varepsilon}-\frac{1}{\lambda})t} - (2-4\lambda\dot{\varepsilon})e^{(-4\dot{\varepsilon}-\frac{1}{\lambda})t} - 3\right) \qquad \textbf{(I.15)}$$

# Appendix J Fitting to Virtual Experimental Data

Ideally the constitutive parameters would be found by fitting to experimental data, but unfortunately there is a paucity of extensional data available in the literature. For this reason, and because it highlights the differences between the E and UL approaches, the constitutive parameters are found by fitting the UL equation to "virtual" experiments conducted using the E constitutive equations. It is worth emphasizing that the virtual experiments differ from real experiments because exact data points are generated; that is, there is no noise or random experimental error in the data. As the film casting problem is extensional in nature, the virtual experiments are chosen to be constant rate of uniaxial extension and equibiaxial extension problems. The closed-form solution for uniaxial and equibiaxial experiments using a nonlinear Maxwell fluid are presented in Appendix I.

The best fit is determined using a Hooke and Jeeves algorithm (Smith *et al.* 1983: p180-183) with the following objective function and constraints

$$\begin{aligned} \min\ z &= \sum_{i=1}^{ndata} (\sigma_{vexp} - \sigma_{nsim})^2 \\ s.t.\ m &> 0 \\ n &> 0 \end{aligned} \qquad \textbf{(J.1)}$$

where $z$ is the squared error, *ndata* is the number of data points, and $\sigma_{vexp}$ and $\sigma_{nsim}$ are the stress values for the virtual experiment and the numerical simulation, respectively. The constraints are enforced using a penalty function.

# Appendix K Elastic Limit of the UCM Equation

The integral form of the UCM constitutive equation is given by (Joseph 1990: p14) as

$$\tau_{ij}(t) = \frac{\eta^s}{\lambda^2}\int_{-\infty}^{t} e^{-\frac{(t-\tau)}{\lambda}}(B_{ij}^{t}(\tau) - \delta_{ij})\,d\tau \qquad \textbf{(K.1)}$$

where $B_{ij}^{t}(\tau)$ is a relative strain tensor, called the relative Finger tensor or the relative left Cauchy Green tensor and $\delta_{ij}$ is the Kronecker delta. The relative Finger tensor depends on the relative deformation gradient tensor $F_{ij}^{\tau}(t)$, which is the gradient of the current position of the material particle at time *t* with respect to some past configuration at time $\tau$; that is,

$$F_{ij}^{\tau}(t) = \frac{\partial x_i(t)}{\partial x_j(\tau)} \qquad \textbf{(K.2)}$$

Using the relative deformation gradient tensor, the relative Finger tensor is defined as

$$B_{ij}^{t}(\tau) \equiv F_{ik}^{\tau}(t)\,F_{jk}^{\tau}(t) = \frac{\partial x_i(t)}{\partial x_k(\tau)}\,\frac{\partial x_j(t)}{\partial x_k(\tau)} \qquad \textbf{(K.3)}$$

Using the properties of integrals, Equation K.1 can be split into two integrals, as follows:

$$\tau_{ij}(t) = \frac{\eta^s}{\lambda^2}\int_{-\infty}^{0} e^{-\frac{(t-\tau)}{\lambda}}(B_{ij}^{t}(0) - \delta_{ij})\,d\tau + \frac{\eta^s}{\lambda^2}\int_{0}^{t} e^{-\frac{(t-\tau)}{\lambda}}(B_{ij}^{t}(\tau) - \delta_{ij})\,d\tau \qquad \textbf{(K.4)}$$

where in the first integral the relative Finger tensor will be constant with respect to τ because the material is assumed not to deform until *t* is greater than zero. The first integral can be evaluated to yield

$$\tau_{ij}(t) = \frac{\eta^s}{\lambda} e^{-\frac{t}{\lambda}} (B_{ij}^t(0) - \delta_{ij}) + \frac{\eta^s}{\lambda^2} \int_0^t e^{-\frac{(t-\tau)}{\lambda}} (B_{ij}^t(\tau) - \delta_{ij}) d\tau \qquad \textbf{(K.5)}$$

Now $\lambda = \eta^s/G$ can be substituted into this equation to produce

$$\tau_{ij}(t) = Ge^{-\frac{tG}{\eta^s}} (B_{ij}^t(0) - \delta_{ij}) + \frac{G^2}{\eta^s} \int_0^t e^{-\frac{(t-\tau)G}{\eta^s}} (B_{ij}^t(\tau) - \delta_{ij}) d\tau \qquad \textbf{(K.6)}$$

The elastic limit of the extra-stress tensor occurs when $\eta^s$ approaches infinity. In this case the exponential function in the first term will approach one, and the exponential function in the second term will approach zero; therefore, in the elastic limit

$$\tau_{ij} = G(B_{ij} - \delta_{ij}) \qquad \textbf{(K.7)}$$

where the reference to time has been dropped because for an elastic material the stress will only depend on the current deformation, not on any past configurations. The Finger tensor for the elastic case depends on the deformation gradient of the deformed position with respect to the original configuration.

# Appendix L Closed-Form Solution for 1.5D Film Casting

Given the drawing force ($F$) in the film, Avenas *et al*. (1986: pp359-369) and Agassant *et al*. (1991: pp239-250) present relations to find the following variables: the draw ratio ($\dot{u}_{roll}/\dot{u}_{die}$), the neck-in ($W_{roll}/W_{die}$) and the thickness change ($h_{roll}/h_{die}$). The theoretical relations assume that the process is isothermal and that the fluid is Newtonian. Also, restrictions are made on the admissible velocity field, so that the problem is 1.5D, with the kinematic assumptions listed in Table 1.1. Therefore, as mentioned in Section 1.4.1 the film maintains a rectangular shape from the die to the roll, as the thickness does not vary in the transverse direction.

The neck-in at the roll is calculated from the following transcendental equation:

$$\begin{gathered} -4AL = (z_{roll} - z_{die}) + \ln\frac{z_{roll}-1}{z_{die}-1} \\ \text{where } A = \frac{F}{12\eta^s Q},\ Q = u_{die}h_{die}W_{die}, \\ z_{roll} = \sqrt{1 + 8A^2W_{roll}^2},\ \text{and } z_{die} = \sqrt{1 + 8A^2W_{die}^2} \end{gathered} \qquad \textbf{(L.1)}$$

Once $W_{roll}/W_{die}$ is known the following relation is used to solve for $h_{roll}/h_{die}$:

$$\ln\frac{W_{roll}}{W_{die}} + 2\ln\frac{h_{roll}}{h_{die}} = -6AL \qquad \textbf{(L.2)}$$

The continuity equation can then be used to determine the draw ratio ($Dr$) via

$$Dr = \frac{u_{roll}}{u_{die}} = \frac{W_{die}h_{die}}{W_{roll}h_{roll}} \tag{L.3}$$

In addition to the above relations, Avenas *et al*. (1986) and Agassant *et al*. (1991) present a theoretical limit for the neck-in

$$\frac{W_{roll}}{W_{die}} = 1 - \sqrt{2}\frac{L}{W_{die}} \tag{L.4}$$

# Appendix M Linear Stability Analysis for 1D Film Casting

The most common approach for determining the stability of continuous polymer processing is linear stability analysis, as described by Denn (1975). In a linear stability analysis the steady-state solution is perturbed by some infinitesimal amount and the behaviour of the linearized governing equations is considered. If the small perturbation damps out, then the process is stable. If the perturbation continues to grow, then the process is considered unstable.

***i) Governing Equations***

In an Eulerian framework, the conservation equations and the constitutive equation for transient isothermal film casting of a viscous fluid are as follows:

$$\frac{\partial h}{\partial t} + \frac{\partial (\dot{u} h)}{\partial x} = 0 \qquad \textbf{(M.1)}$$

$$\frac{\partial (h\sigma)}{\partial x} = 0 \qquad \textbf{(M.2)}$$

$$\sigma = 4\eta^s \frac{\partial \dot{u}}{\partial x} \qquad \textbf{(M.3)}$$

An equation can be eliminated from the above by substituting Equation M.3 into Equation M.2 to obtain

$$\frac{\partial}{\partial x}\left( h \frac{\partial \dot{u}}{\partial x} \right) = 0 \qquad \textbf{(M.4)}$$

The boundary conditions for Equations M.1 and M.4 are $\dot{u}(0, t) = \dot{u}_{die}$, $\dot{u}(L, t) = \dot{u}_{roll}$ and $h(0, t) = h_{die}$. As usual, the draw ratio is defined as $Dr = \dot{u}_{roll}/\dot{u}_{die}$.

***ii) Steady-State Solutions***

The steady state solutions for velocity and thickness ($\dot{u}_{ss}$ and $h_{ss}$) are derived in Appendix G and are repeated here for convenience

$$\dot{u}_{ss} = u_{die} Dr^{\frac{x}{L}}; \qquad h_{ss} = h_{die} Dr^{-\frac{x}{L}} \tag{M.5}$$

***iii) Linearize for Infinitesimal Disturbances***

The solutions for the velocity and thickness may be expressed as the steady-state solutions plus some small perturbations (ξ, μ), as follows:

$$\dot{u}(x,t) = \dot{u}_{ss}(x) + \xi(x,t); \qquad h(x,t) = h_{ss}(x) + \mu(x,t) \tag{M.6}$$

If Equation M.6 is substituted into Equations M.1 and M.4, and if terms over first order in ξ and μ are neglected, by assuming that higher order perturbations are negligible, then the following is obtained:

$$\frac{\partial \mu}{\partial t} + \frac{\partial}{\partial x}\left(\dot{u}_{ss}\mu + h_{ss}\xi\right) = 0 \tag{M.7}$$

$$\frac{\partial}{\partial x}\left( h_{ss}\frac{\partial \xi}{\partial x} + \frac{\partial u_{ss}}{\partial x}\mu \right) = 0 \tag{M.8}$$

Equations M.7 and M.8 take advantage of the simplification that results because $\dot{u}_{ss}$ and $h_{ss}$ are solutions for Equation M.1 and M.4, respectively, and thus drop out of the equations.

The steady-state and perturbed velocities and thicknesses are assumed to satisfy the same boundary conditions; therefore, the boundary conditions for the perturbation variables are $\xi(0,t) = \xi(L,t) = \mu(0,t) = 0$.

***iv) Separation of Variables***

The following separation of variables is assumed to apply:

$$\xi(x,t) = \theta_1(t)\psi(x); \qquad \mu(x,t) = \theta_2(t)\varphi(x) \tag{M.9}$$

If Equation M.9 is substituted into Equation M.7, divided by $\theta_2\varphi$ and rearranged, then the following equation is obtained:

$$\frac{\dot{\theta}_2}{\theta_2} = -\frac{1}{\varphi}\left(\dot{u}_{ss}'\varphi + \dot{u}_{ss}\varphi' + (h_{ss}'\psi + h_{ss}\psi')[\theta_1/\theta_2]\right) = \lambda \tag{M.10}$$

where the superimposed dot ($\cdot$) and the dash ($'$) represent differentiation with respect to time and position, respectively. The first ratio is independent of $x$ and if $\theta_1 = \theta_2$ then the second ratio is independent of time; therefore, the equality can only hold if $\lambda$ is a constant ($\lambda$ does not represent the relaxation time in this usage). The ordinary differential equation for the first ratio can be solved, to yield

$$\theta_1 = \theta_2 = e^{\lambda t} \tag{M.11}$$

The differential equation corresponding to the second ratio is

$$(\dot{u}_{ss}' + \lambda)\varphi + \dot{u}_{ss}\varphi' + (h_{ss}'\psi + h_{ss}\psi') = 0 \tag{M.12}$$

Another differential equation in $x$ is found by substitution of Equations M.9 and M.11 into Equation M.8 and rearranging to yield

$$\dot{u}_{ss}''\varphi + \dot{u}_{ss}'\varphi' + (h_{ss}'\psi' + h_{ss}\psi'') = 0 \qquad \textbf{(M.13)}$$

To reduce the order of the above equation, let $\omega = \psi'$. The system of differential equations, after substitution of Equation M.5 and rearranging, becomes

$$\varphi' = \frac{h_0}{u_0 L}(\ln Dr)Dr^{-\frac{2x}{L}}\psi - \frac{h_0}{u_0}Dr^{-\frac{2x}{L}}\omega - \frac{\ln Dr}{L}\varphi - \frac{\lambda}{u_0}Dr^{-\frac{x}{L}}\varphi \qquad \textbf{(M.14)}$$

$$\psi' = \omega \qquad \textbf{(M.15)}$$

$$\omega' = \frac{\ln Dr}{L}\omega - \frac{u_0}{h_0}(\ln Dr)^2 Dr^{\frac{2x}{L}}\varphi - \frac{u_0}{h_0 L}(\ln Dr)Dr^{\frac{2x}{L}}\varphi' \qquad \textbf{(M.16)}$$

and the associated boundary conditions are $\varphi(0)=\psi(0)=\psi(L)=0$.

Equations M.14 to M.16 are the same as those obtained by Fisher and Denn (1975), except that their equations are written in dimensionless form. The system of equations forms a linear eigenvalue problem, which Fisher and Denn (1975) solve by direct numerical integration, assuming $\omega(0)=1$ and varying $\lambda$ until the downstream boundary condition, $\psi(L)=0$, is satisfied. The integration for various draw ratios shows that the real part of the eigenvalue first becomes positive at a critical draw ratio of 20.2. Below this draw ratio Equation M.11, and thus the perturbations in velocity and thickness, will decay over time, but above this value an arbitrarily small disturbance will grow over time.